Title

Complex-to-Real Mapping for Polymer Field Theories

Author

Liu, Jimmy Voong

Publication Date

2018

University of California
Santa Barbara

Complex-to-Real Mapping for Polymer Field Theories

A dissertation submitted in partial satisfaction
of the requirements for the degree

Doctor of Philosophy
in
Chemical Engineering

by

Jimmy Voong Liu

Committee in charge:

Professor Glenn H. Fredrickson, Chair
Professor M. Scott Shell
Professor Rachel A. Segalman
Professor Carlos J. García-Cervera

September 2018

The Dissertation of Jimmy Voong Liu is approved.

Professor M. Scott Shell

Professor Rachel A. Segalman

Professor Carlos J. García-Cervera

Professor Glenn H. Fredrickson, Committee Chair

September 2018

Complex-to-Real Mapping
for Polymer Field Theories

by

Jimmy Voong Liu

To my parents: let me make you proud.

Acknowledgements

Graduate school has been a singular time in my life that has helped me to grow in many ways. I am thankful for the many opportunities that I was given: to take classes that can open up new worlds, especially in mathematics and in physics; to travel to conferences to speak and hear from scientists far and wide; to hone my skills in analysis and in programming; and to synthesize all of those in a creative way for research. Glenn, I could not have done any of this without your support and your patient guidance. I have always felt like you have my back—thank you.

I thank each of my committee members for your part in shaping my program. You have all been a great source of inspiration to me. In particular, thank you, Carlos, for your constant supply of new ideas.

I am grateful to Samsung Electronics and to NSF DMR CMMT grant no. 1822215 for financial support. I would also like to acknowledge support from the Center for Scientific Computing from the CNSI, MRL: an NSF MRSEC (DMR-1720256) and NSF CNS-1725797.

I have always felt like part of an amazing and talented team, the GHF ensemble. Jan, I will remember how you seize your audience's attention with a bold statement or a joke, how mindfully you approach soft skills, and how you remind me to stay connected. Carol, I will remember you by your boundless interest in topics from science to music. Kris, thank you for the years of input and advice in every aspect of my project—you really are my second advisor. Thank you to everyone I have interacted with and learned from in the group: Dorian Bruch, Eva Chan, Daniel Vigil, Seamus Jones, Josh Lequieu, Nick Sherck, Mukul Tikekar, Jan Garcia, Doug Grzetic, Jon Martin, Scott Danielsen, Doug Tree, Carol Tsai, Corinne Carpenter, Joe Peterson, Yassine Dhane, Andrew Hamilton, Edward Toumayan, Wei Li, Bongkeun Kim, Yi-Xin Liu, Tatsu Iwama, Gaddiel Ouaknin,

Nabil Laachi, Michael Carilli, Sean Paradiso, Kris Delaney, Debbie Audus, Su-Mi Hur, Erin Lennon, and Michael Villet. I will especially miss going out to lunch, both with the reliable crew and with the occasional special guests, and the rush of adventure that is attending conferences together.

Finally, I am blessed to have a supportive family. Thank you, Tina, Jason, Mom, and Dad, for your unconditional love, and for being there for me through so many steps in my life. Thank you, Jen, for the same, and for putting up with long workdays and late nights, for taking care of me, and for teaching me to take a break once in a while and to enjoy it.

Curriculum Vitæ
Jimmy Voong Liu

Education

2018	Ph.D. in Chemical Engineering, University of California, Santa Barbara.
2013	B.S. in Chemical Engineering, Cornell University.

Academic Honors and Awards

2018	Best Poster Presentation Award, UCSB Chemical Engineering Graduate Research Fair
2017	Outstanding ScienceLine Responder Award
2016	Outstanding Presentation Award, Graduate Simulation Seminar Series
2016	Best Poster Presentation Award, Clorox-Amgen Graduate Student Symposium
2016	ScienceLine Award in Physics/Chemistry/Engineering

Publications

J. V. Liu, C. J. García-Cervera, K. T. Delaney, and G. H. Fredrickson, "The optimized phase field model for the diblock copolymer," in preparation.

J. Liu, K. T. Delaney, and G. H. Fredrickson, "Optimized phase field models in confinement: fast and accurate simulations of directed self-assembly," *Proc. SPIE* 10146, 101460Z (2017).

J. Liu, K. T. Delaney, and G. H. Fredrickson, "Phase field mapping for accurate, ultrafast simulations of directed self-assembly," *Proc. SPIE* 9779, 977920 (2016).

J. Liu, N. Laachi, K. T. Delaney, and G. H. Fredrickson, "Advantages and limitations of density functional theory in block copolymer directed self-assembly," *Proc. SPIE* 9423, 94231I (2015).

Selected Presentations

2018	APS March Meeting, Los Angeles, CA
2017	UCSB Graduate Student Symposium, Santa Barbara, CA
2017	APS March Meeting, New Orleans, LA
2017	Graduate Simulation Seminar Series, Santa Barbara, CA
2016	Berkeley Mini Stat Mech Meeting (poster), Berkeley, CA

Abstract

Complex-to-Real Mapping
for Polymer Field Theories

by

Jimmy Voong Liu

Polymer field theory is a valuable tool for studying the behavior of dense polymer systems at near-atomistic length scales. In its most successful form, it is a complex-valued, $d+1$–dimensional theory that can be studied using fully-fluctuating simulations or at the level of self-consistent field theory (SCFT). This theory requires calculations using fields that depend on d spatial variables as well as a contour variable indicating the position along the polymer chain. In principle, it can be reduced to a simpler, real-valued, d-dimensional theory that is more efficient to simulate numerically—a phase field model—but these are typically less accurate due to approximations invoked in their derivations. We introduce and refine a new method for constructing phase field models, phase field mapping, that systematically parametrizes an optimized phase field (OPF) model using the output of inexpensive SCFT simulations. We develop an OPF model for the diblock copolymer melt and characterize its performance in terms of speed, accuracy, and transferability. Then we modify and generalize the model to produce a weakly compressible model suitable for running simulations in confined templates. In bulk and in confinement, the OPF model is faster to simulate than SCFT and more accurate than other phase field models. With these advantages, the OPF model is a useful alternative to complex-valued field theories.

Contents

List of Figures

List of Tables

Chapter 1

Introduction

Polymer field theory is a valuable tool for studying the behavior of dense polymer systems at near-atomistic length scales. In particular, self-consistent field theory (SCFT) simulations have been used to predict phase behavior [1, 2, 3, 4, 5, 6, 7, 8, 9, 10], to guide patterning for manufacturing electronic devices [11, 12, 13, 14, 15, 16, 17, 18], to design materials with desirable mechanical properties [19, 20], and to study dynamical behavior of polymers in processes like solvent vapor annealing [21, 22]. SCFT has been successful at predicting density configurations, length scales and energetics when thermal fluctuations can be neglected (*i.e.*, when either the polymer concentration or the degree of polymerization is large). At an increased computational cost, we can also perform field-theoretic simulations (FTS) using the complex Langevin method to sample these thermal fluctuations [23]. What if the application is too computationally intensive even for SCFT, demanding large parameter sweeps, large cell simulations or time dependence?

Phase field models offer a more computationally efficient method to study such applications. These models do not explicitly encode the contour variable s that indicates the position along a polymer chain in SCFT. This benefits numerical calculations of phase field models in several ways. For a simulation in d spatial dimensions, a field update in SCFT is a $d+1$–dimensional calculation with a computational complexity of $\mathcal{O}(N_s M \log M)$, whereas a field update in a phase field simulation is a d-dimensional calculation with a complexity of only $\mathcal{O}(M \log M)$. Here, N_s is the contour resolution and M is the spatial resolution. Furthermore, in phase field models, stable and metastable states correspond to local minima. This enables the use of the nonlinear conjugate gradient method, an efficient numerical method that requires a convex energy landscape. (In SCFT, the presence of pressure-like fields leads to mixed saddle points and precludes the use of the conjugate gradient method.) Finally, phase field models are purely real-valued. This eliminates the sign problem present in the original field theory, where complex-valued fields and energies lead to difficulties in sampling the probability distribution. Because SCFT typically requires N_s of about 100, we expect that a phase field simulation can be run to convergence faster than a comparable SCFT simulation by roughly two orders of magnitude [24].

Historically, phase field models have been inaccurate compared to SCFT. This is largely due to the approximations used to derive these models: the Landau-Brazovskii model [25] and the Ohta-Kawasaki (OK) model [26] both rely on the random phase approximation (RPA) first applied to the diblock copolymer by Leibler [27]. The RPA is an asymptotic approximation exact only in the weak segregation limit, $\chi N \approx \chi N_s$, where χN is the segregation strength characterizing repulsion between unlike segments and χN_s is the spinodal value signaling the onset of microphase separation. In the intermediate segregation regime where $\chi N > \chi N_s$, the assumed small parameter in the RPA (the amplitude of density oscillations) is large and the RPA is not strictly valid, but the OK model is often used as a crude substitute for SCFT.

To address the drawbacks of these asymptotic and phenomenological phase field models, in this dissertation, we introduce a new approach to developing phase field models, phase field mapping. The method is based on the coarse-graining technique of force-matching for particle theories [28] and for field theories [29]. Like the coarse-graining method, phase field mapping parametrizes a cheaper model by minimizing the difference in thermodynamic forces between two models—in this case, SCFT and a phase field model. In principle, the mapping can be exact: no accuracy is necessarily lost in switching to a phase field description of the theory.

Starting from a particle-based theory for a diblock copolymer melt, we derive an equivalent field theory that can be studied using SCFT or fluctuating FTS. We show that that complex-valued field theory can be reduced to a real-valued field theory, a phase field model. We then explore how best to formulate the phase field mapping procedure to complete an optimized phase field (OPF) model. We also study the performance of the OPF model with respect to its speed, its accuracy, and its transferability to other phases (that is, how general the mapped model is). Next, we attempt to develop a phase field model compatible with the wall masking method previously developed for SCFT [11] to extend the advantages of the real-valued theory to confined systems. Finally, we offer some perspective on directions for future work in complex-to-real mapping of field theories.

1.1 Complex-valued field theory

We now outline a derivation for the complex-valued field theory that will serve as the starting point for phase field mapping. We start from a particle-based model for a polymer system, then use a particle-to-field transformations to obtain an equivalent field-based model. Here, we define the theory for a diblock copolymer melt, because most of our phase field mapping work is done for this system, but blends and other architectures are possible as well. We generally follow similar notation as in reference [3], except that we immediately nondimensionalize lengths, energies and the contour variable, as explained next.

1.1.1 Particle-based model

Our model describes an incompressible diblock copolymer melt consisting of n continuous Gaussian chains in a volume V. Each chain consists of N statistical segments of length b, of which a fraction f are of type A and the remaining segments are of type B. From this point on, we choose to express lengths in units of the radius of gyration $R_\mathrm{g} = b\sqrt{N/6}$ and energies in units of $k_B T$, the product of Boltzmann's constant and the temperature. The canonical partition function for this system is

$$\mathcal{Z}_C(n,V,T) = \frac{1}{n!\lambda_T^{3nN}} \prod_{j=1}^{n} \int \mathcal{D}\mathbf{r}_j \, e^{-U_0[\mathbf{r}^{nN}]-U_1[\mathbf{r}^{nN}]} \mathcal{K} \tag{1.1}$$

where λ_T is the thermal de Broglie wavelength and $\{U_i\}$ represent contributions to the potential energy of the system. $\mathcal{K}$ is a compressibility constraint—we will defer the specifics to the end of the section. The integral $\int \mathcal{D}\mathbf{r}_j$ denotes a path integral over the continuous function $\mathbf{r}_j(s)$ (in (1.1), note that the product should be applied only to the integration measure and not to the integrand). For a given chain j, the space curve $\mathbf{r}_j = \mathbf{r}_j(s)$ is a vector-valued function for the spatial position of the chain as a function of contour position s. We choose to scale s so that its domain runs from 0 to 1. As shown in Figure 1.1, $s \in [0, f)$ corresponds to the A block and $s \in [f, 1]$ corresponds to the B block.

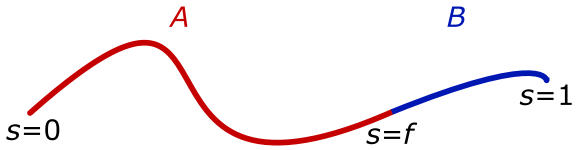

Figure 1.1: A schematic of an AB diblock copolymer chain indicating contour positions $s = 0, f$, and 1.

The potential energy consists of two terms, the chain stretching energy

$$U_0[\mathbf{r}^{nN}] = \frac{1}{4}\sum_{j=1}^{n}\int_0^1 ds \left|\frac{d\mathbf{r}_j(s)}{ds}\right|^2, \tag{1.2}$$

and a sum over pairwise interactions,

$$U_1[\mathbf{r}^{nN}] = \sum_{j=1}^{n}\sum_{k=1}^{n}\int_0^f ds \int_f^1 ds'\, u(|\mathbf{r}_j(s) - \mathbf{r}_k(s')|). \tag{1.3}$$

For both terms, we have used the notation $[\mathbf{r}^{nN}]$ to denote a functional dependence on n space curves each with N statistical segments—but note that, rigorously, each chain has an infinite number of degrees of freedom because it is a function of the continuous variable s. In the bounds of integration in (1.3), we have assumed that monomers of type A interact only with monomers of type B and vice versa. For numerical convenience, we further assume that the interaction $u(r)$ occurs only on contact:

$$u(r) = v_0\chi\delta(r) \tag{1.4}$$

where v_0 is the volume of a statistical segment and χ is the Flory-Huggins parameter characterizing the strength of the repulsion between A- and B-type monomers in units of k_BT. This choice of pairwise interaction allows us to write

$$U_1[\mathbf{r}^{nN}] = v_0\chi\int d\mathbf{r}\,\check{\rho}_A(\mathbf{r})\check{\rho}_B(\mathbf{r}) \tag{1.5}$$

where on the right-hand side, $\mathbf{r}$ is the position vector (not a space curve), and we have used Dirac delta functions to define microscopic species density operators $\check{\rho}_A$ and $\check{\rho}_B$

according to

$$\check{\rho}_A(\mathbf{r}) = \sum_{j=1}^{N} \int_0^f ds\, \delta(\mathbf{r} - \mathbf{r}_j(s)) \tag{1.6}$$

$$\check{\rho}_B(\mathbf{r}) = \sum_{j=1}^{N} \int_f^1 ds\, \delta(\mathbf{r} - \mathbf{r}_j(s)). \tag{1.7}$$

Finally, we briefly discuss the compressibility constraint $\mathcal{K}$. Its purpose is to embed the assumption of incompressibility into $\mathcal{Z}_C$. That is,

$$\check{\rho}_A(\mathbf{r}) + \check{\rho}_B(\mathbf{r}) = \rho_0 \tag{1.8}$$

at all points $\mathbf{r}$, where $\rho_0 = \frac{1}{v_0} = \frac{nN}{V}$ is the system average density. The constraint is expressed as a delta functional

$$\mathcal{K} = \delta[\check{\rho}_A + \check{\rho}_B - \rho_0], \tag{1.9}$$

which eliminates from the integrals in (1.1) any configuration that violates (1.8). This grants us the useful property that, under an integral, we can make any replacement using (1.8) (as long as we preserve the delta functional itself).

In Chapter 4, we will use a compressible model that relaxes the constraint (1.8) and instead assigns a large energetic penalty for local deviations from the average density, often referred to as the Helfand compressibility:

$$\mathcal{K}_\zeta = e^{-v_0\zeta/2 \int d\mathbf{r}\, (\check{\rho}_A(\mathbf{r}) + \check{\rho}_B(\mathbf{r}) - \rho_0)^2}, \tag{1.10}$$

We typically use a compressibility $(\zeta N)^{-1} = 0.001$, indicating that the melt is only weakly compressible.

1.1.2 Field-based model

We now transform the particle-based model defined by (1.1), (1.2) and (1.5) into a field-based model. Our goal is to eliminate explicit dependence on $\{\mathbf{r}_j\}$, and to reexpress all instances of $\check{\rho}_A$ and $\check{\rho}_B$ in terms of fluctuating density fields ρ_A and ρ_B. To this end, we will introduce the following integral and delta functional (and similar for species B):

$$F[\check{\rho}_A] = \int \mathcal{D}\rho_A \, F[\rho_A] \, \delta[\rho_A - \check{\rho}_A]. \tag{1.11}$$

When we apply this to the right-hand side of equation (1.1), we obtain

$$\mathcal{Z}_C = \frac{1}{n! \lambda_T^{3nN}} \int \mathcal{D}\rho_A \int \mathcal{D}\rho_B \prod_{j=1}^{n} \int \mathcal{D}\mathbf{r}_j \, e^{-U_0[\mathbf{r}^{nN}] - U_1[\mathbf{r}^{nN}]} \mathcal{K} \, \delta[\rho_A - \check{\rho}_A] \delta[\rho_B - \check{\rho}_B], \tag{1.12}$$

and we can now replace occurrences of $\check{\rho}_A$ and $\check{\rho}_B$ in the integrand (in U_1 and in $\mathcal{K}$) with ρ_A and ρ_B respectively. We also apply an exponential representation of the delta functional,

$$\delta[\rho_A - \check{\rho}_A] = \int \mathcal{D}w_A \, e^{i \int d\mathbf{r} \, w_A(\mathbf{r})(\rho_A(\mathbf{r}) - \check{\rho}_A(\mathbf{r}))}, \tag{1.13}$$

which introduces the auxiliary fields w_A and w_B. Finally, we collect terms in the integrand that still depend on $\mathbf{r}_j$, $\check{\rho}_A$ or $\check{\rho}_B$, noting that they factor by chain:

$$\begin{aligned}
&\prod_{j=1}^{n} \int \mathcal{D}\mathbf{r}_j \, e^{-U_0[\mathbf{r}^{nN}] - i \int d\mathbf{r} \, w_A(\mathbf{r}) \check{\rho}_A(\mathbf{r}) - i \int d\mathbf{r} \, w_B(\mathbf{r}) \check{\rho}_B(\mathbf{r})} \\
&\quad = \left(\int \mathcal{D}\mathbf{r}_1 \, e^{-1/4 \int_0^1 ds \, |d\mathbf{r}_1(s)/ds|^2 - \int_0^f ds \, i w_A(\mathbf{r}_1(s)) - \int_f^1 ds \, i w_B(\mathbf{r}_1(s))} \right)^n && (1.14) \\
&\quad = (Z_0 Q[i w_A, i w_B])^n. && (1.15)
\end{aligned}$$

Z_0 is a normalization factor and Q is the single-chain partition function for a diblock copolymer, given by

$$Q[iw_A, iw_B] = \frac{1}{V} \int d\mathbf{r}\, q(\mathbf{r}, 1; [iw_A, iw_B]) q^\dagger(\mathbf{r}, 0; [iw_A, iw_B]), \tag{1.16}$$

which in turn requires the solution to Fokker-Planck equations for the propagators q and $q^\dagger$:

$$\frac{\partial q(\mathbf{r}, s; [iw_A, iw_B])}{\partial s} = \nabla^2 q(\mathbf{r}, s; [iw_A, iw_B]) - iNw(\mathbf{r}, s) q(\mathbf{r}, s; [iw_A, iw_B]) \tag{1.17}$$

subject to the initial condition $q(\mathbf{r}, 0) = 1$; $w(\mathbf{r}, s) = w_A(\mathbf{r})$ for contour positions s within the A block ($0 \leq s < f$), or $w_B(\mathbf{r})$ otherwise. The complementary propagator $q^\dagger$ solves the analogous equation starting from the B end of the chain.

We now have a density-explicit expression for the field-based model suitable for numerical simulation:

$$\mathcal{Z}_C = \mathcal{Z}_0 \int \mathcal{D}\rho_A \int \mathcal{D}\rho_B \int \mathcal{D}w_A \int \mathcal{D}w_B\, e^{-H[w_A, w_B, \rho_A, \rho_B]} \delta[\rho_A + \rho_B - \rho_0], \tag{1.18}$$

where $\mathcal{Z}_0$ is the ideal gas contribution, and the action or effective Hamiltonian is

$$\begin{split} H[w_A, w_B, \rho_A, \rho_B] = -v_0 \chi \int d\mathbf{r}\, \rho_A(\mathbf{r}) \rho_B(\mathbf{r}) - i \int d\mathbf{r}\, \left[w_A(\mathbf{r}) \rho_A(\mathbf{r}) - w_B(\mathbf{r}) \rho_B(\mathbf{r}) \right] \\ - n \ln Q[iw_A, iw_B]. \end{split} \tag{1.19}$$

Because H is quadratic in the densities ρ_A and ρ_B, the model is often further simplified by applying a Hubbard-Stratonovich transform, which uses Gaussian integrals to eliminate both density fields, leaving a functional dependence only on w_A and w_B. Instead, to facilitate the connection to the next section, we write an equivalent model that leaves one density field explicit and eliminates the other using the remaining delta functional in (1.18) (incompressibility). By convention, phase field models also typically scale the density fields by ρ_0, reexpressing them in terms of

$$\phi(\mathbf{r}) = \phi_A(\mathbf{r}) = \rho_A(\mathbf{r})/\rho_0 \tag{1.20}$$

$$= 1 - \phi_B(\mathbf{r}) = 1 - \rho_B(\mathbf{r})/\rho_0. \tag{1.21}$$

Our model is now

$$\mathcal{Z}_C = \mathcal{Z}_0' \int \mathcal{D}\phi \int \mathcal{D}w_A \int \mathcal{D}w_B \, e^{-H[w_A, w_B, \phi]} \tag{1.22}$$

with the simplified Hamiltonian

$$\frac{H[w_A, w_B, \phi]}{C} = -\chi N \int d\mathbf{r}\, \phi(\mathbf{r})^2 - i \int d\mathbf{r}\, [N w_A(\mathbf{r}) - N w_B(\mathbf{r})]\phi(\mathbf{r}) - V \ln Q[i w_A, i w_B], \tag{1.23}$$

where $C = \frac{n}{V}$ is the chain density expressed in units of chains per R_{g}^3. Note that H/C is still an extensive energy. Later, we will also make use of intensive energies H/CV, with units of $k_B T$ per chain, and H/V, with units of $k_B T / R_{\mathrm{g}}^3$.

We can numerically approximate the path integrals in (1.22) using a complex Langevin technique that explores different field configurations and accumulates their contributions, or simplify the equations using mean field theory, *i.e.*, self-consistent field theory (SCFT). SCFT approximates the integrals by the field configuration with the largest contribution, (ϕ^*, w_A^*, w_B^*), corresponding to a stationary point in H. This leads to the self-consistent field equations for equilibrium configurations (ϕ^*, w_A^*, w_B^*),

$$\left.\frac{\delta H[w_A, w_B, \phi]}{\delta \phi(\mathbf{r})}\right|_{\phi=\phi^*, w_A=w_A^*, w_B=w_B^*} = 0 \tag{1.24}$$

$$\left.\frac{\delta H[w_A, w_B, \phi]}{\delta w_A(\mathbf{r})}\right|_{\phi=\phi^*, w_A=w_A^*, w_B=w_B^*} = 0 \tag{1.25}$$

$$\left.\frac{\delta H[w_A, w_B, \phi]}{\delta w_B(\mathbf{r})}\right|_{\phi=\phi^*, w_A=w_A^*, w_B=w_B^*} = 0, \tag{1.26}$$

which we solve numerically by the pseudospectral method and iterative relaxation methods based on gradient descent, typically the semi-implicit Seidel (SIS) scheme [30], as we will discuss in the next section. Note that equilibrium states in SCFT are independent of the chain density C. Furthermore, if we use the groupings χN (hereafter the segregation strength), Nw_A and Nw_B everywhere in (1.23), we find that the equations are also independent of the molecular weight N.

Finally, we briefly comment on the compressible model obtained by substituting $\mathcal{K}_\zeta$ from (1.10) for $\mathcal{K}$. The particle-to-field transformation proceeds mostly unchanged until (1.18). At this point, the delta functional is replaced by an expression like $\mathcal{K}_\zeta$, but with ρ_A and ρ_B rather than $\check{\rho}_A$ and $\check{\rho}_B$, that is usually appended to the Hamiltonian. We can then rescale the ρ fields, but we cannot eliminate one. In place of (1.22) and (1.23), we find

$$\mathcal{Z}_C = \mathcal{Z}_0' \int \mathcal{D}\phi_A \int \mathcal{D}\phi_B \int \mathcal{D}w_A \int \mathcal{D}w_B \, e^{-H[w_A, w_B, \phi_A, \phi_B]}, \tag{1.27}$$

$$\begin{aligned} \frac{H[w_A, w_B, \phi_A, \phi_B]}{C} &= \chi N \int d\mathbf{r}\, \phi_A(\mathbf{r})\phi_B(\mathbf{r}) + \frac{\zeta N}{2} \int d\mathbf{r}\, [\phi_A(\mathbf{r}) + \phi_B(\mathbf{r}) - 1]^2 \\ &\quad - i \int d\mathbf{r}\, [Nw_A(\mathbf{r})\phi_A(\mathbf{r}) - Nw_B(\mathbf{r})\phi_B(\mathbf{r})] - V \ln Q[iw_A, iw_B]. \end{aligned} \tag{1.28}$$

1.2 Numerical methods

We now discuss our methods of choice for computing solutions to self-consistent equations like (1.24), the pseudospectral method and gradient descent relaxation. The essence of the pseudospectral method is that we can freely alternate between a real-space and a Fourier-space representation of each field, choosing whichever is more convenient at any time. This will be convenient for calculating the force for our relaxation dynamics.

In this work, we will denote the Fourier representation of a real-space field $g(\mathbf{r})$ as

$$\mathcal{F}[g] = \hat{g}(\mathbf{k}) = \int d\mathbf{r}\, e^{-i\mathbf{k}\cdot\mathbf{r}} g(\mathbf{r}). \tag{1.29}$$

An advantage of the pseudospectral method over spectral methods is that we can quickly and directly compute products in real space, rather than as convolutions in Fourier space. Given fields $g(\mathbf{r})$ and $h(\mathbf{r})$, the convolution is

$$\begin{aligned}
\mathcal{F}[gh] &= \int d\mathbf{r}\, e^{-i\mathbf{k}\cdot\mathbf{r}} g(\mathbf{r}) h(\mathbf{r}) \\
&= \int d\mathbf{r} \int d\mathbf{r}'\, e^{-i\mathbf{k}\cdot\mathbf{r}} g(\mathbf{r}) h(\mathbf{r}') \delta(\mathbf{r}-\mathbf{r}') \\
&= \int d\mathbf{r} \int d\mathbf{r}' \int d\mathbf{k}'\, e^{-i\mathbf{k}\cdot\mathbf{r}} g(\mathbf{r}) h(\mathbf{r}') e^{-i\mathbf{k}'\cdot(\mathbf{r}-\mathbf{r}')} \\
&= \int d\mathbf{k}' \left(\int d\mathbf{r}\, e^{-i(\mathbf{k}-\mathbf{k}')\cdot\mathbf{r}} g(\mathbf{r}) \right) \left(\int d\mathbf{r}'\, e^{-i\mathbf{k}'\cdot\mathbf{r}'} h(\mathbf{r}') \right) \\
&= \int d\mathbf{k}'\, \hat{g}(\mathbf{k}-\mathbf{k}') \hat{h}(\mathbf{k}').
\end{aligned} \tag{1.30}$$

For a spatial resolution of M, the convolution has a cost of $\mathcal{O}(M^2)$, while the product is only $\mathcal{O}(M)$ (and, if needed, the Fourier transform is $\mathcal{O}(M \log M)$). An advantage of the pseudospectral method over finite difference methods is the accuracy of derivative calculations. We will often exploit the following property of the Fourier transform:

$$\begin{aligned}\mathcal{F}[\nabla g] &= \int d\mathbf{r}\, e^{-i\mathbf{k}\cdot\mathbf{r}} \nabla g(\mathbf{r}) \\ &= -\int d\mathbf{r}\, \nabla e^{-i\mathbf{k}\cdot\mathbf{r}} g(\mathbf{r}) \\ &= i\mathbf{k} \int d\mathbf{r}\, e^{-i\mathbf{k}\cdot\mathbf{r}} g(\mathbf{r}) \\ &= i\mathbf{k}\, \hat{g}(\mathbf{k}), \end{aligned} \tag{1.31}$$

which shows that a derivative in real space, an approximate calculation in a finite difference scheme, can be computed with spectral accuracy as a product in Fourier space.

Let us briefly explain the gradient descent method (also sometimes called steepest descent). For simplicity, suppose we have a Hamiltonian H that depends only on one field ϕ. The self-consistent equation for this Hamiltonian is

$$\left.\frac{\delta H[\phi]}{\delta \phi(\mathbf{r})}\right|_{\phi=\phi^*} = 0. \tag{1.32}$$

The left side of this equation, the "gradient" of H with respect to ϕ (not $\mathbf{r}$) will be used as the force for our relaxation. In general, it has some components that are convenient to calculate in real space and others that are convenient to calculate in Fourier space. A basic gradient descent scheme to solve equation (1.32) for the equilibrium state ϕ^* is

$$\frac{\partial}{\partial t}\phi(\mathbf{r}, t) = -\frac{\delta H[\phi]}{\delta \phi(\mathbf{r}, t)}, \tag{1.33}$$

where we have introduced a fictitious time variable t. We can choose the initial condition $\phi(\mathbf{r}, 0)$ arbitrarily, for example, using a simple sinusoidal pattern or random noise. We then iteratively solve for ϕ by discretizing t into timesteps of size Δt. Because t here does not correspond to a physical time, we are not interested in intermediate values of

$\phi(\mathbf{r},t)$, so the timestep Δt is limited by numerical stability only, not accuracy. As long as equation (1.33) converges to a steady state for long times, we will find

$$\lim_{t\to\infty}\frac{\partial}{\partial t}\phi(\mathbf{r},t) = -\frac{\delta H[\phi]}{\delta\phi(\mathbf{r},t)} = 0, \tag{1.34}$$

indicating that $\phi(\mathbf{r},t)$ converges to $\phi^*(\mathbf{r})$:

$$\lim_{t\to\infty}\phi(\mathbf{r},t) = \phi^*(\mathbf{r}). \tag{1.35}$$

In practice, we decide that numerical relaxation is sufficiently converged when the L^2 norm of the force reaches a chosen tolerance, say, 10^{-5}, or perhaps smaller if we must compute the energy to high precision to resolve small energy differences.

In this work, we will use a number of modifications to the fully-explicit gradient descent scheme in equation (1.33), the most important of which are the semi-implicit Seidel (SIS) scheme from reference [30] and the nonlinear conjugate gradient method in Section 3.1.1. We also mention another class of relaxation methods, known as diffusive dynamics, that would be necessary to describe the physical evolution of a system over time (unlike the fictitious time variable in equation (1.33)). A simple diffusive dynamics scheme is

$$\frac{\partial}{\partial t}\phi(\mathbf{r},t) = \nabla^2\frac{\delta H[\phi]}{\delta\phi(\mathbf{r},t)}. \tag{1.36}$$

Finally, we note that in practice, we will actually relax the Fourier representations of each field, *i.e.*,

$$\frac{\partial}{\partial t}\hat{\phi}(\mathbf{k},t) = -\frac{\delta H[\phi]}{\delta\hat{\phi}(-\mathbf{k},t)}. \tag{1.37}$$

Also, because we must discretize the continuous fields to a spatial resolution of M grid points, we should actually replace ϕ with a finite M-dimensional vector $\boldsymbol{\phi}$, which will replace functional derivatives $\frac{\delta}{\delta\phi(\mathbf{r})}$ with vector derivatives $\frac{\partial}{\partial\boldsymbol{\phi}}$. Apart from these notational changes, the derivations in this section still hold.

1.3 Attribution

Parts of this dissertation are reproduced (adapted) in part with permission from:

Jimmy Liu, Nabil Laachi, Kris T. Delaney and Glenn H. Fredrickson, "Advantages and limitations of density functional theory in block copolymer directed self-assembly," *Proc. SPIE* **9423**, 94231I (Mar 19, 2015). doi:10.1117/12.2085666,

Jimmy Liu, Kris T. Delaney and Glenn H. Fredrickson, "Phase field mapping for accurate, ultrafast simulations of directed self-assembly," *Proc. SPIE* **9779**, 977920 (Mar 25, 2016). doi:10.1117/12.2219311,

Jimmy Liu, Kris T. Delaney and Glenn H. Fredrickson, "Optimized phase field models in confinement: fast and accurate simulations of directed self-assembly," *Proc. SPIE* **10146**, 101460Z (Mar 27, 2017). doi:10.1117/12.2258106, and

Jimmy V. Liu, Carlos J. García-Cervera, Kris T. Delaney and Glenn H. Fredrickson, "The optimized phase field model for the diblock copolymer," in preparation.

Chapter 2

Phase field mapping method development

In this chapter, we develop a method for parametrizing real-valued phase field models from complex-valued theories. First, starting from the complex-valued model of Section 1.1.2, we derive a real-valued model and point out the types of approximations that may be invoked. We then focus on adapting the force-matching method from the coarse-graining literature to our needs. Simply producing a sensible model consistently can be a challenge: our first naive attempts to use force-matching to parametrize coefficients often resulted in terms with the wrong sign. By exploring variations in the procedure and in the choice of basis set, we will attempt to elucidate elements that are critical to a robust mapping method.

2.1 Reduction to real-valued field theory

By evaluating the integrals over w configurations in (1.22), we can in principle express the partition function in terms of an exact reduced action $H_{\mathrm{e}}[\phi]$:

$$e^{-H_{\mathrm{e}}[\phi]} = \int \mathcal{D}w_A \int \mathcal{D}w_B \, e^{-H[w_A, w_B, \phi]}, \tag{2.1}$$

$$\mathcal{Z}_C = \int \mathcal{D}\phi \, e^{-H_{\mathrm{e}}[\phi]}. \tag{2.2}$$

The functional H_{e} rigorously defines a phase field model whose statistics are consistent with the field theory from the previous section. Numerically, though, the form of H_{e} grants it several advantages over the original complex-valued Hamiltonian H. Because H_{e} is purely real-valued, the Boltzmann weight $e^{-H_{\mathrm{e}}}$ is positive definite, circumventing the sign problem associated with the original weight e^{-H}. Because H_{e} is a locally convex functional, we can perform phase field calculations using efficient numerical methods such as the nonlinear conjugate gradient method. Finally, because the single-chain partition functions have been integrated out, the theory does not require the chain contour variable s, nor the solution to the modified diffusion equation (1.17), reducing the theory from $d+1$ dimensions to d spatial dimensions.

In the following sections, it will be useful to express the thermodynamic force for this phase field model in terms of the original ensemble. By differentiating equation (2.1) with respect to $\phi(\mathbf{r})$, we find that

$$\left.\frac{\delta H_{\mathrm{e}}[\phi]}{\delta \phi(\mathbf{r})}\right|_{\phi=\phi_0} = \left\langle \frac{\delta H[w_A, w_B, \phi]}{\delta \phi(\mathbf{r})} \right\rangle_{\phi_0}, \tag{2.3}$$

where the average over w configurations at some value of $\phi = \phi_0$ is defined as

$$\langle G[w_A, w_B, \phi] \rangle_{\phi_0} = \frac{\int \mathcal{D}w_A \int \mathcal{D}w_B \, G[w_A, w_B, \phi_0] e^{-H[w_A, w_B, \phi_0]}}{\int \mathcal{D}w_A \int \mathcal{D}w_B \, e^{-H[w_A, w_B, \phi_0]}}. \tag{2.4}$$

We can also apply a partial saddle approximation (a mean field approximation for the w fields only) that picks out the largest contribution to each of the $\int \mathcal{D}w$ integrals. In this case, equations (2.1), (2.3), and (2.4) simplify to

$$e^{-H_{\mathrm{e}}[\phi]} \approx e^{-H[w_A^*, w_B^*, \phi]}, \tag{2.5}$$

$$\left. \frac{\delta H_{\mathrm{e}}[\phi]}{\delta \phi(\mathbf{r})} \right|_{\phi=\phi_0} \approx \left. \frac{\delta H[w_A^*, w_B^*, \phi]}{\delta \phi(\mathbf{r})} \right|_{\phi=\phi_0} \tag{2.6}$$

$$\langle G[w_A, w_B, \phi] \rangle_{\phi_0} \approx G[w_A^*, w_B^*, \phi_0], \tag{2.7}$$

where w_A^* and w_B^* minimize H for any given choice of ϕ.

Whether or not we apply the partial saddle approximation, H_{e} can be studied either at the mean-field level or accounting for fluctuations in ϕ. For this study, we again focus on mean-field solutions ϕ^*. At these minima, $H_{\mathrm{e}}[\phi^*]$ represents a classical density functional theory for the Helmholtz free energy.

Unfortunately, the functional form of H_{e} cannot be obtained analytically [31] except in simple cases [32], so we must approximate it. We will denote the approximate reduced Hamiltonian H_{r}: $H_{\mathrm{e}}[\phi] \approx H_{\mathrm{r}}[\phi]$. Other authors have tried various forms for H_{r}, but these approximations are often severe—for example, the random phase approximation (RPA) only recovers the same results as Section 1.1 in the asymptotic limit of small density perturbations about the homogeneous (disordered) state. Consequently, for many applications, SCFT has been more successful.

2.2 Basis set framework

As we explore various avenues for improving phase field models, it will be valuable to have a framework for defining models that we can easily modify and that clearly delineates inputs and outputs to a phase field mapping procedure. This framework should also encompass existing models (for the diblock copolymer melt) like the Landau-Brazovskii (LB) [25], Ohta-Kawasaki (OK) [26] and generalized Ohta-Kawasaki (gOK) models [33].

To this end, we express H_r as a linear expansion in a set of basis functionals $\{h_i\}$:

$$H_\mathrm{r}[\phi] = \sum_i c_i h_i[\phi]. \tag{2.8}$$

The basis set $\{h_i\}$ is an input to the mapping procedure. To build a phase field model, we first choose the basis set from intuitive arguments, for example, using Landau's theory of phase transitions [34] or the random phase approximation [27] (note that the LB, OK and gOK models are all derived from the RPA). We are only interested in the functional dependence on ϕ: we ignore any numerical prefactors given by other models. Instead, we obtain the coefficients $\{c_i\}$ as outputs from the mapping procedure, as we will explain in the next section.

For example, in our notation, a LB-type model can be written

$$\frac{H_{\mathrm{r,LB}}[\phi]}{C} = \int d\mathbf{r} \left\{ c_2 \delta\phi(\mathbf{r})^2 + c_3 \delta\phi(\mathbf{r})^3 + c_4 \delta\phi(\mathbf{r})^4 + c_5 \left|\nabla\phi(\mathbf{r})\right|^2 + c_6 [\nabla^2\phi(\mathbf{r})]^2 \right\}, \tag{2.9a}$$

and an OK-type model can be written

$$\frac{H_{\mathrm{r,OK}}[\phi]}{C} = \int d\mathbf{r} \left\{ c_2 \delta\phi(\mathbf{r})^2 + c_3 \delta\phi(\mathbf{r})^3 + c_4 \delta\phi(\mathbf{r})^4 + c_5 \left|\nabla\phi(\mathbf{r})\right|^2 + c_6 \int d\mathbf{r}'\, G(\mathbf{r}-\mathbf{r}')\delta\phi(\mathbf{r})\delta\phi(\mathbf{r}') \right\}, \quad (2.9\mathrm{b})$$

where $\delta\phi \equiv \phi - f$ serves as an order parameter for microphase separation (it is positive in an A-rich region and negative in a B-rich region). G is the Green's function for Laplace's equation: it satisfies $-\nabla^2 G(\mathbf{r}-\mathbf{r}') = \delta(\mathbf{r}-\mathbf{r}')$ and has units of R_{g}^{2-d}, where d is the number of spatial dimensions. This reflects the connectivity of the diblock copolymer and prevents macrophase separation. We outline the derivation of (2.9b) in Appendix A.2.

We can study these energy functionals analytically to learn about properties of $\{c_i\}$ that we should expect from a successful mapping. Both forms of H_{r} above can be divided into two parts, one local in real space and one local in Fourier space. Each part dictates the properties of $\delta\phi$ in some asymptotic limit. (Note that the appropriate division is somewhat arbitrary, since h_2 is local in both real space and Fourier space, while h_5 and the LB form of h_6 are semilocal in real space and local in Fourier space.)

The first part is an integral over a Landau polynomial $\mathcal{L}(\delta\phi)$, where

$$\mathcal{L}(\delta\phi) = c_2\delta\phi^2 + c_3\delta\phi^3 + c_4\delta\phi^4. \quad (2.10)$$

The Landau polynomial dominates H_{r} in the narrow interface limit. This is because at any point $\mathbf{r}$ where we can neglect the wavevector-dependent part (*i.e.*, away from the interfaces), the magnitude of $\delta\phi$ will try to minimize $\mathcal{L}$ to lower its contribution to the energy. If the system is capable of (micro)phase separation, we know from Landau's theory of phase transitions that $\mathcal{L}$ should have a double-well structure as shown in Figure 2.1. Thus we expect to find $c_4 > 0$ and $c_2 < 0$. The sign of c_3 depends on f: it should be negative for $f < 0.5$, zero for $f = 0.5$, and positive for $f > 0.5$.

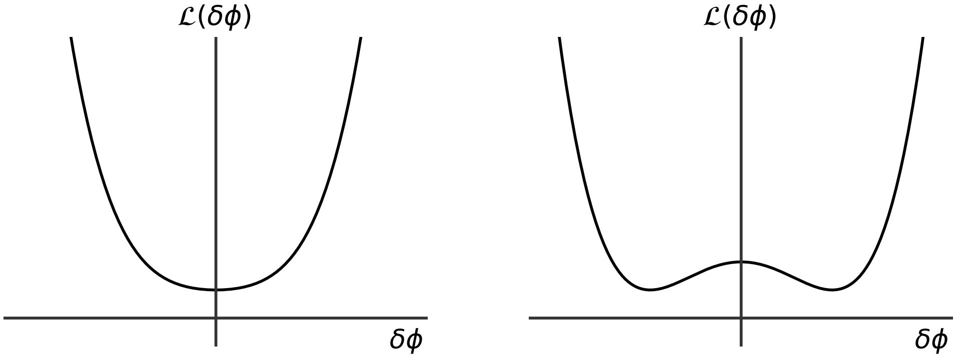

Figure 2.1: Examples of the Landau polynomial $\mathcal{L}(\delta\phi)$ for temperatures on either side of a phase transition. In Landau theory, as the temperature is decreased below the spinodal, $\mathcal{L}$ changes from having only one minimum, corresponding to the homogeneous disordered phase (left), to having a double-well structure with two minima, one positive and one negative, corresponding to the A-rich and B-rich phases respectively (right).

The second part of H_r dominates in the weak segregation limit, where $\delta\phi$ is small in amplitude. In this case, we can neglect the Landau polynomial and rewrite H_r in terms of the Fourier transform $\widehat{\delta\phi}(\mathbf{k})$ to find

$$\frac{H_{\mathrm{r,LB}}[\phi]}{C} \approx \frac{1}{V}\sum_{\mathbf{k}}\left(c_5k^2 + c_6k^4\right)\left|\widehat{\delta\phi}(\mathbf{k})\right|^2 \tag{2.11a}$$

or

$$\frac{H_{\mathrm{r,OK}}[\phi]}{C} \approx \frac{1}{V}\sum_{\mathbf{k}}\left(c_5k^2 + c_6k^{-2}\right)\left|\widehat{\delta\phi}(\mathbf{k})\right|^2. \tag{2.11b}$$

Now, apply the single-mode approximation: assume that a single Fourier mode $k^* > 0$ dominates $\left|\widehat{\delta\phi}(\mathbf{k})\right|$. The value of k^* should minimize H_r, so it must be

$$k^* = (-c_5/2c_6)^{\frac{1}{2}} \tag{2.12a}$$

or

$$k^* = (c_6/c_5)^{\frac{1}{4}}, \tag{2.12b}$$

and the signs of the coefficients must be $c_5 < 0$ and $c_6 > 0$ for LB-type models, or $c_5 > 0$ and $c_6 > 0$ for OK-type models. This sets a preferred length scale for domain sizes $L_0 = \frac{2\pi}{k^*}$. As χN increases above the weak segregation limit, the terms from the Landau polynomial begin to play a role in setting L_0 and the single-mode approximation breaks down.

We have outlined two possible choices for the basis set, those that we used most extensively, but there are many others. In fact, it can be shown that the vector space of H_e is spanned by an uncountably infinite basis. It will become clear that the choice of basis set has a large impact on the quality of the model produced by phase field mapping (or any other method of determining the coefficients). Much effort in this chapter was put towards identifying appropriate metrics for model quality and assessing whether failures arise from deficiencies in the basis set or from deficiencies in the coefficient mapping.

2.3 Force-matching

2.3.1 Method

Phase field mapping is a novel method for producing phase field models [35]. It systematically parametrizes a phase field model using only a small number of inexpensive SCFT calculations. The method draws inspiration from the force-matching technique for coarse-graining particle and field theories. Phase field mapping is analogous to coarse-graining in that it reduces one theory to another that is more efficient to solve numerically. Unlike conventional coarse-graining, though, there is in principle no loss of accuracy in switching from SCFT to a phase field description. The new model is not tied to a coarse discrete spatial mesh, as it is in renormalization group theory—it is still a functional of a continuous density field. Given an ideal set of basis functionals, we expect that the reduced action would agree perfectly with SCFT. In this sense, phase field mapping shares more in common with electronic density functional theory.

Given the Hamiltonian H, a representative configuration ϕ^*, and a reduced action H_r with undetermined parameters $\{c_i\}$, we minimize the following cost metric Ψ quantifying the disagreement between the two models:

$$\Psi(\{c_i\}) = \frac{1}{V}\int d\mathbf{r}\, \left[\left.\frac{\delta H_\mathrm{r}[\phi]}{\delta\phi(\mathbf{r})}\right|_{\phi=\phi^*} - \left\langle \frac{\delta H[w_A, w_B, \phi]}{\delta\phi(\mathbf{r})} \right\rangle_{\phi^*} \right]^2 . \tag{2.13}$$

For the linear form of H_r in (2.8), Ψ is a quadratic form in $\{c_i\}$ and minimization amounts to solving a system of linear equations in those parameters. We can choose to optimize some or all of the $\{c_i\}$. Any coefficients not being optimized should be fixed to some predetermined values, for example, those prescribed in RPA-based models.

Equation (2.13) represents force-matching. It penalizes differences between the thermodynamic forces in the two models. This penalty is zero in the ideal case where the forces exactly match, such as when H_r is exactly equal to H_e, as shown in (2.3), and positive otherwise.

If the representative configuration ϕ^* is chosen according to the conditions described in the previous sections (i.e., if it is a stationary point in H), then the SCFT force is zero. Then minimizing (2.13) amounts to selecting parameters $\{c_i\}$ that minimize the phase field force when evaluated at the configuration ϕ^*. If we attempt to minimize with respect to all of the $\{c_i\}$, the linear system becomes homogeneous, so the mapping admits a family of solutions that differ only by a multiplicative factor on all of the $\{c_i\}$. In this case, we fix one of the coefficients to a constant value (typically 1 or -1, whichever is appropriate) before minimization. The choice of multiplicative factor does not affect any of the stationary points of H_{r}, so we will not concern ourselves with it for now, but we can later choose it through another method, such as the one explained in Section 2.4.1.

2.3.2 Results

We applied the force-matching scheme defined in Section 2.3.1 to determine optimal values for c_2, c_3 and c_4 for LB-type and OK-type models (2.9a) and (2.9b), holding other coefficients fixed at values given in the literature, at various values of χN for $f = 0.5$ (a symmetric diblock). We first analyze the coefficients themselves to see if the mapping is sensible, then we move on to study properties of the mapped model by computing equilibrium solutions to $H_{\mathrm{r}}[\phi]$.

Figure 2.2 shows the mapped coefficients c_2 and c_4 and compares them to the values from the literature. As expected by symmetry for this block fraction, the mapping effectively found that c_3 was zero (typically it was order 10^{-5} due to numerical errors). Note that in the original OK model, no values are given for the c_3 and c_4 parameters—the value may be freely adjusted. To be as fair as possible to the original model, in subsequent results, we defined the “original” values using phase field mapping with only the c_3 and c_4 parameters optimized.

The results of Figure 2.2 are encouraging in two ways. First, the mapping produced coefficient values with the correct signs $c_2 < 0$, $c_3 = 0$ and $c_4 > 0$. (We did not see the same success when optimizing the semilocal/nonlocal term coefficients c_5 and c_6 until Section 2.4.1.) Second, the mapping seems to recover the RPA result in the weak segregation limit $\chi N \approx \chi N_s$, where those models were derived and should be most accurate.

Next, we studied one-dimensional equilibrium density fields, minima of $H_{\mathrm{r}}[\phi]$, using

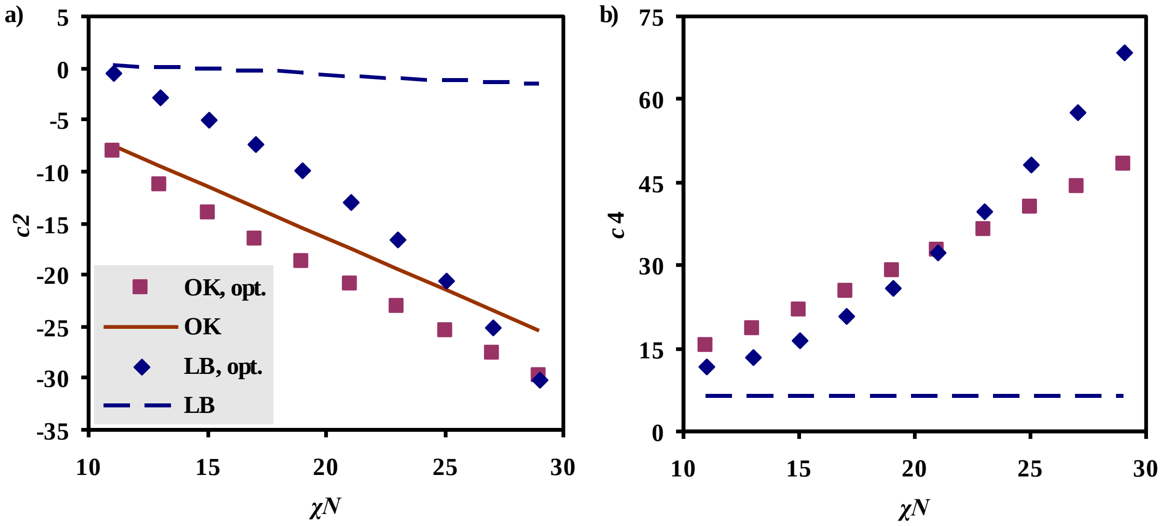

Figure 2.2: Values for phase field model coefficients (a) c_2 and (b) c_4 versus χN. Each plot shows original values for the LB model (dashed line) and the OK model (solid line), and values optimized by phase field mapping for an LB-type model (diamonds) and an OK-type model (squares). Note that the original formulation of the OK model does not give a value for c_4.

numerical simulations in a periodic cell. (Note that equilibrium solutions of H_{r} will generally not be identical to equilibrium solutions of H.) Figure 2.3 shows typical density fields ϕ^*_{PF} for original and optimized phase field models compared to the SCFT solution ϕ^*_{SCFT} under commensurate conditions—that is, the size of the simulation cell is consistent with the equilibrium SCFT period $L_{0,\mathrm{SCFT}}$. Note that in weakly segregated systems $\chi N = 15$, the SCFT density profile is roughly sinusoidal, while at higher values ($\chi N = 35$), it has an increasingly “square” character. The original LB model does not capture either the shape nor the saturation of the SCFT profile. On the other hand, the optimized LB model captures both in weakly segregated systems ($\chi N = 15$); at higher segregation strengths ($\chi N = 35$), it finds roughly the correct saturation but fails to capture the shape, instead showing unexpected “creasing” behavior in the center of each domain. The OK-type model shows similar trends, but because the “original” model already captured the density profile fairly well, the effect is less pronounced. We can understand this improvement in terms of the Landau polynomial (2.10): the mapping procedure correctly sets its coefficients to capture the right saturation values for ϕ in each (A-rich or B-rich) domain.

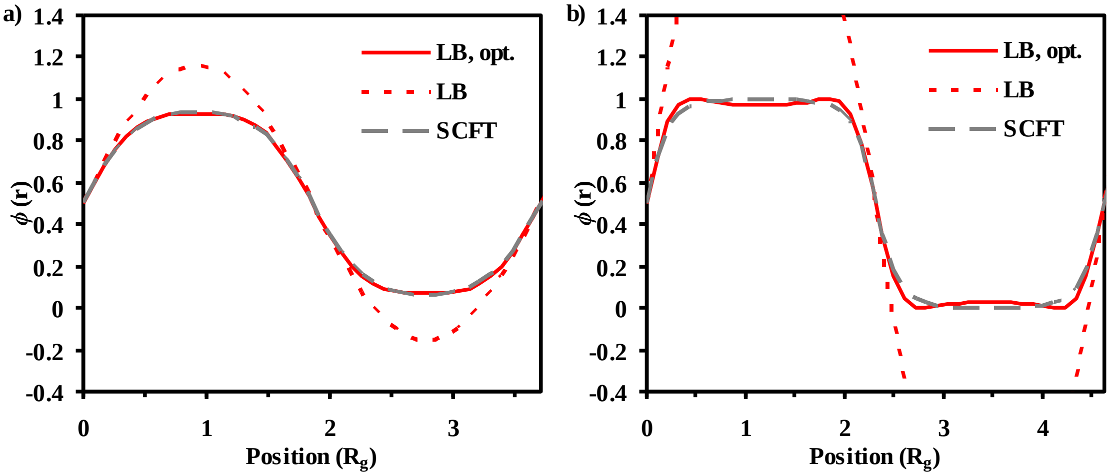

Figure 2.3: Equilibrium density fields predicted by the original LB model (dotted red line) and optimized LB model (solid red line) compared to SCFT (dashed grey line) in a commensurate cell (a) at $\chi N = 15$, and (b) at $\chi N = 35$, both at $f = 0.5$.

In spite of the creasing issue, the improvement in the density fields from model optimization is clear. We quantified the improvement in Figure 2.4 by measuring the root mean square (L^2 norm) of the error made by phase field models density relative to SCFT,

$$r = \left(\frac{1}{V} \int d\mathbf{r} \left[\phi^*_{\mathrm{PF}}(\mathbf{r}) - \phi^*_{\mathrm{SCFT}}(\mathbf{r}) \right]^2 \right)^{1/2} \tag{2.14}$$

at each value of χN. We present results for original and unoptimized version of the LB and OK models and, for comparison, the original version of the gOK model (we did not find good results from optimizing a gOK-type model). In all cases, optimized models make smaller errors than the original versions, thanks to the improved form of the Landau polynomial. As χN increases, though, all of the phase field models seem unable to reproduce the increasingly "square" character of the SCFT density profile, instead showing creasing behavior. We attribute this remaining disagreement to a limitation of the basis sets (2.9a) and (2.9b).

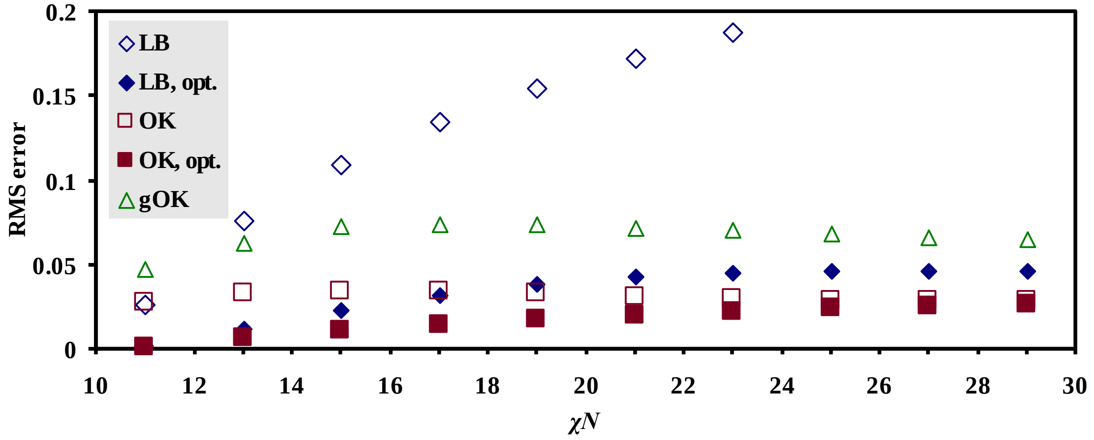

Figure 2.4: Root mean square error in density made by phase field models relative to SCFT versus χN in a commensurate cell with $f = 0.5$. Shown are original (open shapes) and optimized (closed shapes) versions of the LB model (diamonds) and OK model (squares), as well as the original gOK model (triangles).

The improvements we obtained in the equilibrium density fields using optimized models are an early success of our optimization procedure. However, note that the optimized values for c_2 and c_4 are both strong functions of χN. From the derivation of $H_{\mathrm{e}}[\phi]$, we expect that only the quadratic coefficient, c_2, should depend on χN, and that dependence must be linear. We believe this to be a limitation of the basis sets (2.9a) and (2.9b), just like the remaining disagreement in the density fields.

Next, we investigated the performance of these models under incommensurate conditions. When the system is subjected to an incommensurate cell size, the density profile must be reshaped to accomodate the resulting internal stress. We found that phase field models, both original and optimized, responded to incommensurate conditions differently than SCFT.

Figure 2.5 shows two types of nonphysical behavior that arise. First, we now found the creasing effect in all three types of phase field models (LB-type, OK-type, and gOK). This is particularly notable for the gOK model, which is designed to perform well in the strong segregation regime and is typically better at reproducing square density profiles. Secondly, LB and OK density profiles, even optimized ones, sometimes exceed physically relevant values for ϕ, predicting volume fractions less than 0 or greater than 1.

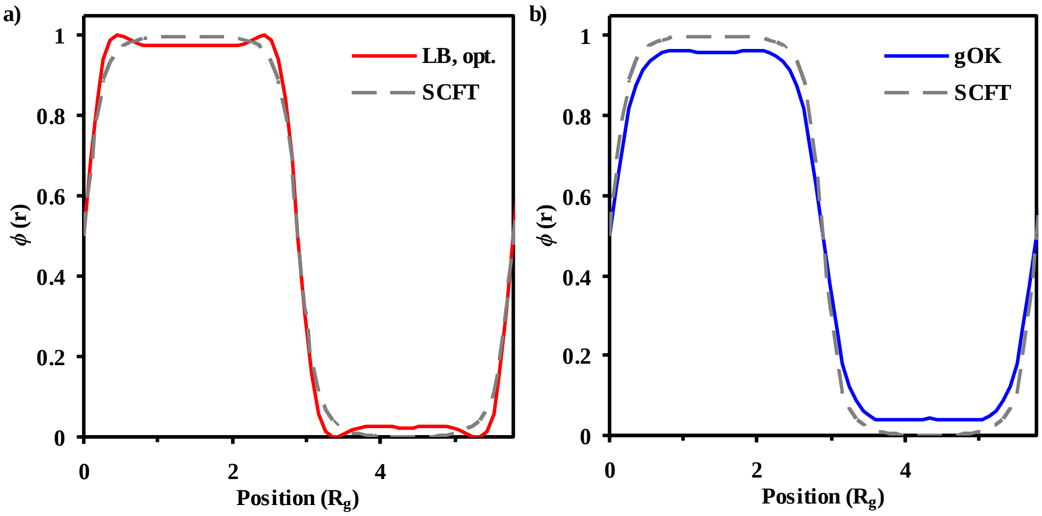

Figure 2.5: Equilibrium density fields from phase field models showing nonphysical behavior under strongly incommensurate conditions. Rather than using the commensurate domain size $L_{0,\mathrm{SCFT}}$, the system size is fixed at $1.25L_{0,\mathrm{SCFT}}$. In (a), the optimized LB model predicts volume fractions less than 0 and greater than 1, and in (b), the gOK model shows creasing, both at $\chi N = 35$ and $f = 0.5$.

We found that we could constrain the densities to stay between 0 and 1 by adding logarithmic terms to H_r like $\int d\mathbf{r}\, \phi \ln \phi$ as done in some other models [36, 33]. However, we were unable to prevent creasing in any of the models. Because confinement often induces incommensurability effects, these issues must be considered in any confined studies.

Next, we continued our investigation of commensurability effects by performing a variable cell size calculation for each phase field model, as demonstrated in Figure 2.6. (In this case, we are not evolving the cell size over the course of a single simulation, but instead computing equilibrium configurations in cells of various sizes.) We found local minima in H_r corresponding to lamellar configurations with two, three and four periods (of which two are metastable or unstable) and then plotted their intensive free energies $H_\mathrm{r}[\phi^*]/CV$ as a function of the cell size L. We can then identify the domain spacing $L_{0,\mathrm{PF}}$ for each phase field model from the location of the minima (divided by the number of lamellae there). In Figure 2.6, the cell size is listed in units of $L_{0,\mathrm{SCFT}}$ the domain spacing obtained in SCFT, so that if the phase field model agrees perfectly with SCFT, the minima should occur at integer multiples of $L_{0,\mathrm{SCFT}}$. Instead, in this case, we find that the gOK model at $\chi N = 15$ reaches a minimum for three lamellae at 2.8 L_0, a difference of 0.72 R_g or about 5 nm for a typical PS-PMMA diblock copolymer.

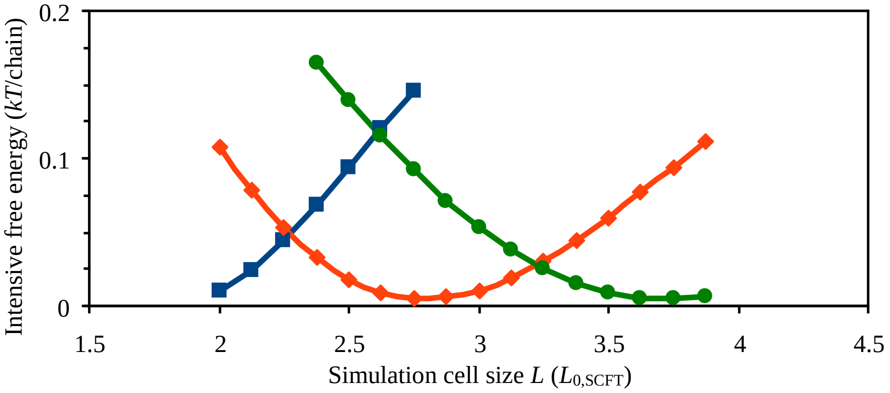

Figure 2.6: A typical variable cell calculation, shown here for the gOK model at $\chi N = 15$ and $f = 0.5$. We plot the intensive free energy H_r/CV for two- (left, blue), three- (middle, red) and four-period lamellar configurations (right, green) as a function of the cell size (in units of the SCFT domain spacing L_0). The minimum of each curve corresponds to an integer multiple of the gOK model's predicted domain spacing $L_{0,\mathrm{gOK}}$. Each curve is harmonic in the vicinity of the minimum with a curvature related to the Young's modulus, but then becomes anharmonic as L deviates farther from the minimum.

By repeating this variable cell size calculation over a range of χN for several models, we obtained predicted domain spacings for various phase field models (and for SCFT), as shown in Figure 2.7. We discovered that none of the phase field models predicts domain spacings that agree in value or in scaling with SCFT. From previous studies using SCFT,

L_0/R_g is known to scale as $N^{\alpha-0.5}$, where α is approximately 1 just above the weak segregation limit and gradually decreases towards $\frac{2}{3}$ as χN increases [37]. Note that this scaling is given for L_0 in units of $R_\mathrm{g} = b\sqrt{N/6}$, consistent with the rest of our work—if lengths are instead given in dimensional units, the relation becomes $L_0 \sim N^\alpha$.

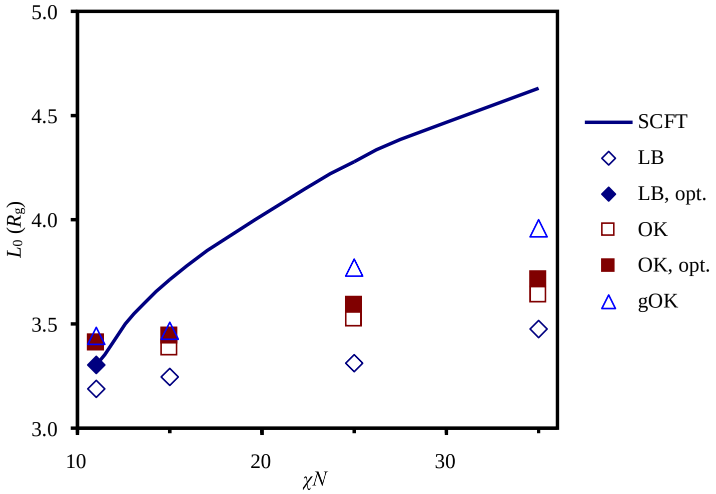

Figure 2.7: Domain spacing L_0 in units of R_g versus χN predicted by the original OK (open squares), optimized OK (closed squares), original LB (open diamonds), optimized LB (closed diamonds) and original gOK models (open triangles) compared to the SCFT values (solid line). The domain spacing for the optimized LB model for $\chi N > 15$ was too large to fit on the scale of the figure.

The disagreement in L_0 has significant ramifications for the quality of these phase field models. Because the commensurability window is shifted, we do not expect predictions of defect energies to agree with SCFT. As an example, in Figure 2.8, we computed the defect formation energy for a simple defect, four lamellae in a cell of size $3L_{0,\mathrm{SCFT}}$, at various values of χN. In this case, the phase field model defect energy prediction is both quantitatively and qualitatively useless: because of the incorrect domain spacing scaling, at higher values of χN, all of the phase field models (except for the optimized LB model) predict the four-period state to be more stable than the three-period state.

The conclusion from Figure 2.8 is that comparisons between simulations using SCFT

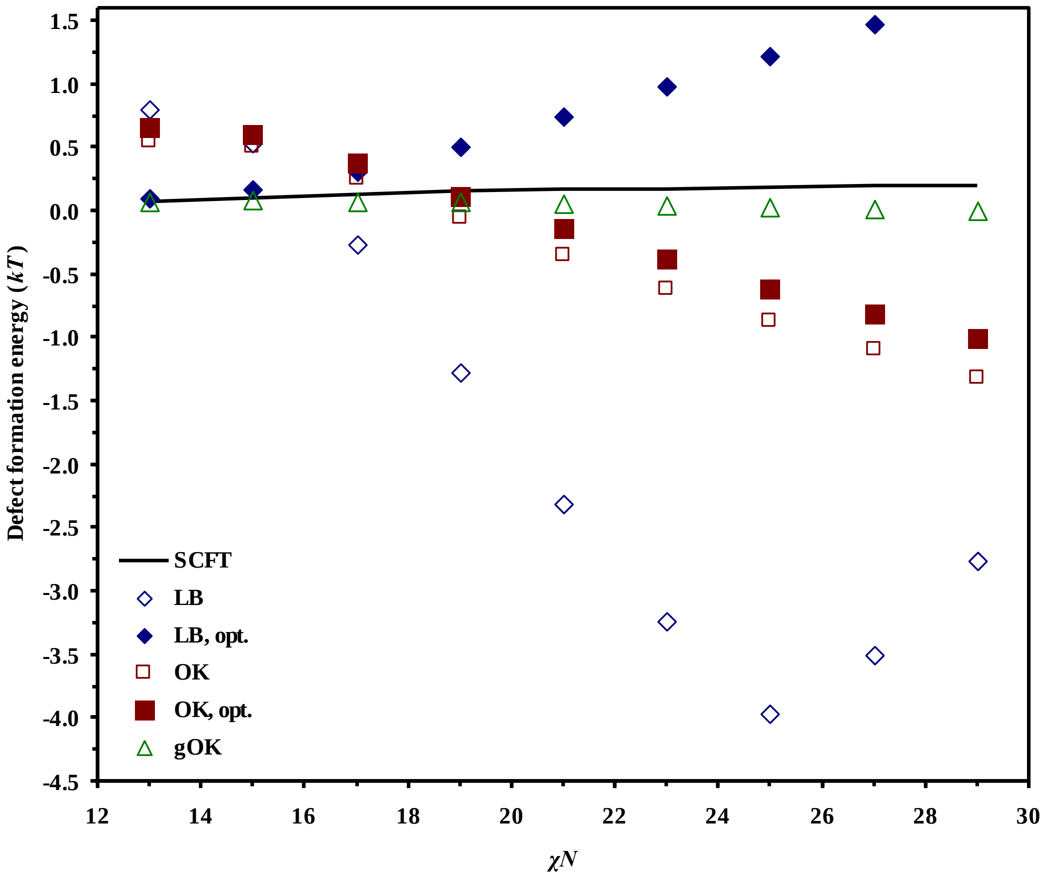

Figure 2.8: Defect formation energy for a four-period lamellar state in a cell of size $3L_{0,\mathrm{SCFT}}$ as predicted by SCFT (solid line), original LB (open diamonds), optimized LB (closed diamonds), original OK (open squares), optimized OK (closed squares), and original gOK models (open triangles) versus χN. The reference energy is taken to be the energy of the globally stable state (according to SCFT), three lamellae. Negative values for the defect energy indicate that the defect is more stable than the three-period state.

using these phase field model simulations must be done carefully, accounting for the mismatch in the model domain spacing L_0, and the results should be viewed with some skepticism. We are unlikely to find quantitative measurements of lengths or energies. As a partial solution, we may be able to observe qualitative trends using phase field model simulations in cell dimensions rescaled by the ratio $\frac{L_{0,\mathrm{PF}}}{L_{0,\mathrm{SCFT}}}$, but this amounts to changing the physical constant R_g to a value inconsistent with the polymer's molecular weight. Our results in this section, particularly Figures 2.6 and 2.7, led us next to revisit and improve the mapping procedure.

2.4 Force-matching with stress-matching

In Section 2.3, we found that force-matching gave us a way to systematically parametrize coefficients in the Landau polynomial using only an equilibrium density field from SCFT. Still, we encountered a limitation to the method: we were unable to obtain sensible results when trying to optimize coefficients for semilocal and nonlocal terms c_5, c_6 and c_6, so we fixed them to their literature values. Because these terms are primarily responsible for setting the domain spacing L_0, it is unsurprising that these phase field models, optimized or not, did not match length scales with SCFT.

Can we modify the phase field mapping procedure to embed SCFT values of L_0 into the optimized models? We sought a functional of ϕ that is to L_0 as the force $\frac{\delta H}{\delta \phi(\mathbf{r})}$ is to the equilibrium density ϕ^*. We proposed to use the derivative $\frac{\partial H/V}{\partial L}$: just as $\frac{\delta H}{\delta \phi(\mathbf{r})}$ is zero when evaluated at (ϕ^*, w_A^*, w_B^*), $\frac{\partial H/V}{\partial L}$ is zero when evaluated at $L = L_0$ (and (ϕ^*, w_A^*, w_B^*)). Figure 2.6 demonstrates an analogous situation using the phase field energy H_r/V in place of H/V and the phase field equilibrium density in place of ϕ^*. We can reexpress our new functional in more conventional terms by defining the strain

$$\epsilon = \frac{L - L_0}{L_0}, \tag{2.15}$$

where it is understood that L_0 is strictly the correct SCFT value, not necessarily the domain spacing for the current model. Then the stress is

$$\frac{\partial H_V[w_A, w_B, \phi]}{\partial \epsilon} = -C \frac{\partial \ln Q[iw_A, iw_B]}{\partial \epsilon}, \tag{2.16}$$

which we will try to match to the analogous stress for the real-valued field theory,

$$\frac{\partial H_{\mathrm{r},V}[\phi]}{\partial \epsilon} = \sum_i c_i \frac{\partial h_i[\phi]}{\partial \epsilon}. \tag{2.17}$$

For brevity, we have written $H_V = H/V$ and $H_{\mathrm{r},V} = H_{\mathrm{r}}/V$. Note that these stresses have units of energy per volume ($k_B T/R_{\mathrm{g}}^3$), just like the forces $\frac{\delta H}{\delta\phi(\mathbf{r})}$ and $\frac{\delta H_r}{\delta\phi(\mathbf{r})}$. An example derivation of a stress is given in Section A.3.

2.4.1 Method

We now use equations (2.16) and (2.17) to develop an improved procedure for phase field mapping that addresses the model's predictions of domain size and defect energies. As before, we minimize Ψ given the Hamiltonian H, a representative configuration ϕ^*, and a reduced action H_{r} with undetermined parameters $\{c_i\}$, where

$$\begin{aligned}\Psi(\{c_i\}) = \frac{1}{V}\int d\mathbf{r}\, &\left[\left.\frac{\delta H_{\mathrm{r}}[\phi]}{\delta\phi(\mathbf{r})}\right|_{\phi=\phi^*} - \left\langle \frac{\delta H[w_A, w_B, \phi]}{\delta\phi(\mathbf{r})} \right\rangle_{\phi^*} \right]^2 \\ &+ \lambda \left[\left.\frac{\partial H_{\mathrm{r},V}[\phi]}{\partial\epsilon}\right|_{\phi=\phi^*} - \left\langle \frac{\partial H_V[w_A, w_B, \phi]}{\partial\epsilon} \right\rangle_{\phi^*} \right]^2 .\end{aligned} \tag{2.18}$$

For the form of H_{r} in (2.8), Ψ is again a quadratic form in $\{c_i\}$ and can be minimized by solving a system of linear equations. The first half of the equation is the force-matching term, unchanged from (2.13). The second half of (2.18) matches stresses between the two models by assigning a penalty to differences between them. This penalty is zero in the ideal case where the stresses exactly match, such as when H_{r} is exactly equal to H_{e}, as shown in (2.3), and positive otherwise. When evaluating the derivatives, it is understood that the density field $\phi = \phi^*$ also carries information about the simulation cell size L in which it was obtained (and therefore the value of ϵ). The dimensionless parameter λ controls the balance between force- and stress-matching. As it is increased, the parametrized values change and lead to improved predictions of length scales until the values eventually saturate. We studied the dependence of $\{c_i\}$ on λ and found that setting $\lambda = 100$ was sufficient to produce parameters within 1% of their saturated values.

In the following sections, we will choose a stress-free stationary point in H as the representative configuration ϕ^*, so that both the SCFT force and stress are zero. The minimum of equation (2.18) then tries to minimize both the phase field force and stress at ϕ^*, with the relative importance of the stress determined by λ. As before, if we optimize with respect to all of the $\{c_i\}$, the linear system becomes homogeneous, so the mapping admits a family of solutions that differ only by a multiplicative factor. In this case, we fix $c_2 = -1$ before minimization, then determine the multiplicative factor by matching the elastic modulus from SCFT:

$$\left.\frac{\partial^2 H_{\mathrm{r},V}[\phi]}{\partial \epsilon^2}\right|_{\phi=\phi^*} = \left.\frac{\partial^2 H_V[w_A^*, w_B^*, \phi]}{\partial \epsilon^2}\right|_{\phi=\phi^*}. \tag{2.19}$$

We can compute these derivatives analytically at ϕ^*, or approximate them by computing H and H_r for several values of ϵ evenly spaced around 0 and measuring the curvature [38], whichever is more convenient. In the latter case, small values of ϵ, say ±0.01, will produce better estimates of the modulus, since cubic and higher order terms begin to play a role at larger values.

2.4.2 Results

As a test of the improved mapping procedure, we parametrized an optimized phase field (OPF) model of the form (2.9b) for a symmetric diblock copolymer ($f = 0.5$). With the addition of the stress term to the cost function, we were able to parametrize all of the model coefficients simultaneously, and obtain useful values for the semilocal coefficient c_5 and the nonlocal coefficient c_6. Therefore, we have for the first time succeeded in producing a phase field mapping without any help in the form of information about coefficients from previous models.

Figure 2.9 compares coefficients from the OPF model with coefficients from the unoptimized OK model as given in Appendix A.2. Since the OK model does not specify a value for c_4, we used the mapping procedure to determine its best possible value given the unoptimized values of the other coefficients (for this mapping, equation (2.18) is equivalent to (2.13) because $h_4[\phi]$ does not contribute to the stress).

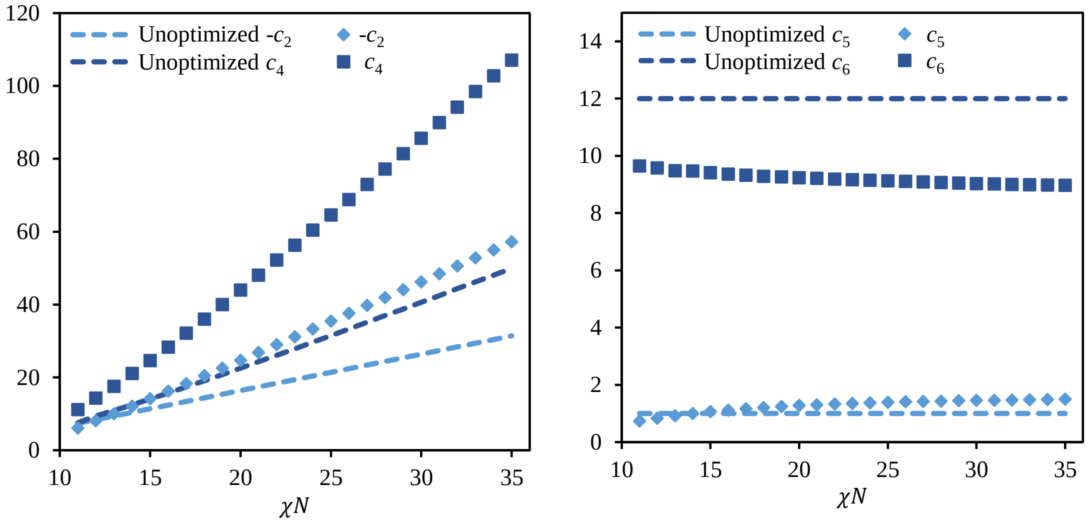

Figure 2.9: Phase field model coefficients for a symmetric diblock copolymer melt for χN from 11 to 35. Left: optimized local coefficients $-c_2$ (diamonds) and c_4 (squares) and unoptimized local coefficients (dotted lines). Right: optimized semilocal/nonlocal coefficients c_5 (diamonds) and c_6 (squares) and unoptimized coefficients (dotted lines).

As in Section 2.3, the optimization procedure correctly identified that c_3 should be zero for the symmetric case. The optimized local coefficients also seem consistent with the standard OK model values in the weak segregation limit $\chi N \approx \chi N_s = 10.495$. On the other hand, the optimized values for c_5 and c_6 clearly do not reduce to the OK model values in this limit—why?

In the OK model, c_5 and c_6 are chosen to match the behavior of the structure factor $\tilde{S}(\mathbf{k})$ for large and small wavevectors, respectively (for more details, see Appendix A.2). These choices immediately determine the critical wavevector k^*, as shown in (2.12b), reproduced here:

$$k^* = (c_6/c_5)^{\frac{1}{4}}, \tag{2.20}$$

but this does not agree exactly with the RPA critical wavevector. In the weak segregation regime where the single-mode approximation is valid, the OK model predicts that

$$L_0 = 2\pi/k^* = 2\pi(c_5/c_6)^{\frac{1}{4}}, \tag{2.21}$$

but this also does not agree exactly with the RPA value of L_0. On the other hand, because the OPF model is parametrized with the goal of improving its predicted domain spacing, it can choose values for c_5 and c_6 that produce a better match to the RPA in the weak segregation regime (and to SCFT at all values of χN). Note that the single-mode approximation rapidly becomes inaccurate as χN increases above χN_s, since many harmonics are already engaged in SCFT solutions even quite near the ODT.

Now, we demonstrate the ability of the improved mapping procedure by repeating the type of variable cell calculation from Figure 2.6. Using SCFT, the OPF model and the unoptimized OK model, we calculated the intensive free energy H/CV or H_r/CV for two-, three- and four-period lamellar states for simulation cell sizes from $2L_{0,\mathrm{SCFT}}$ to $4L_{0,\mathrm{SCFT}}$. Figure 2.10 compares the results for these models at $\chi N = 25$. We observe that the OK model underestimates the location of the minimum for three lamellae by $0.5L_{0,\mathrm{SCFT}}$. The OPF model properly predicts the minima to occur at integer multiples of $L_{0,\mathrm{SCFT}}$ and captures the overall shape of the SCFT curve, which is important for calculating defect formation energies.

By fitting several points on these curves to a quadratic function and calculating the location of the minima, we obtained the predicted domain spacing L_0 for each model as a function of χN. Figure 2.11 shows that the OPF model successfully predicts L_0 to within one percent of $L_{0,\mathrm{SCFT}}$ across the entire range of χN studied, a property that we did not find for any previously studied phase field model.

The OPF model domain spacing still shows a small systematic error at larger values

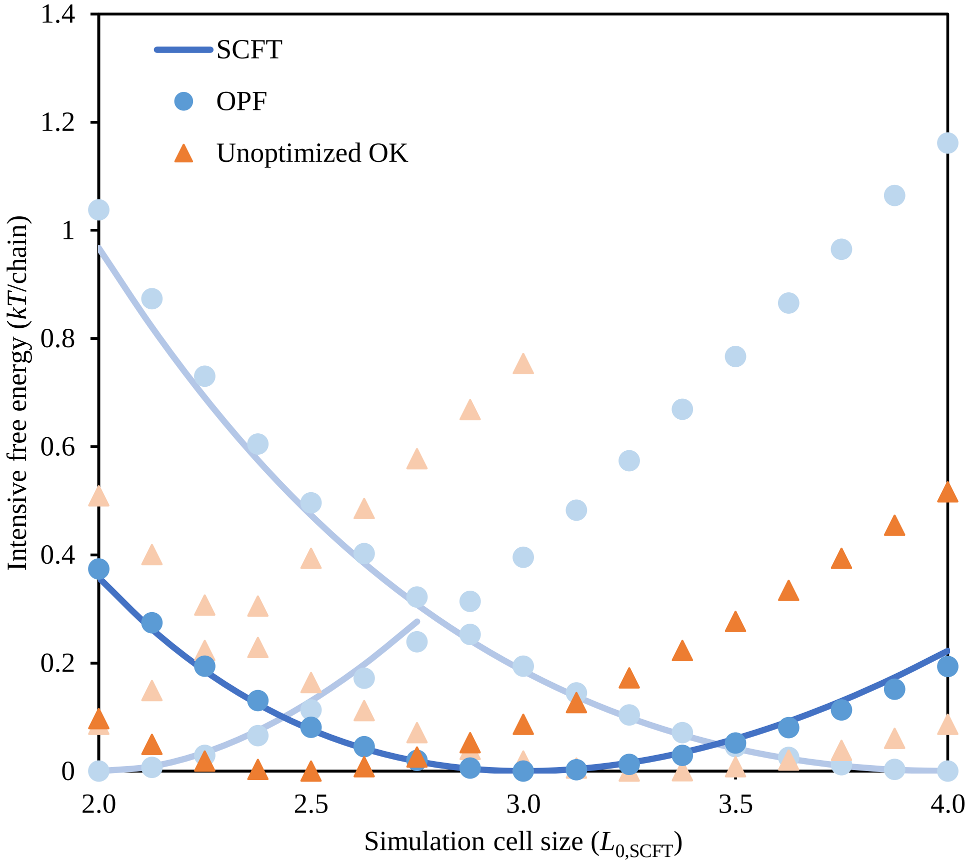

Figure 2.10: Intensive free energy of a lamellar diblock copolymer system at $\chi N = 25$ as a function of the simulation cell size in units of the SCFT domain spacing $L_{0,\mathrm{SCFT}}$ for SCFT (solid blue lines), the OPF model (blue circles), and the unoptimized OK model (orange triangles). From left to right, the curves represent free energies for two-, three- and four-period lamellar configurations. The minimum of each curve occurs at a multiple of the model's predicted domain spacing.

of χN. This error comes from the discrepancy between the density fields of an OK-type model and SCFT, which is a limitation of the basis set (2.9b). This result reinforces our message that, even with our improved phase field mapping procedure, identifying a strong basis set has a significant effect on the quality of the model.

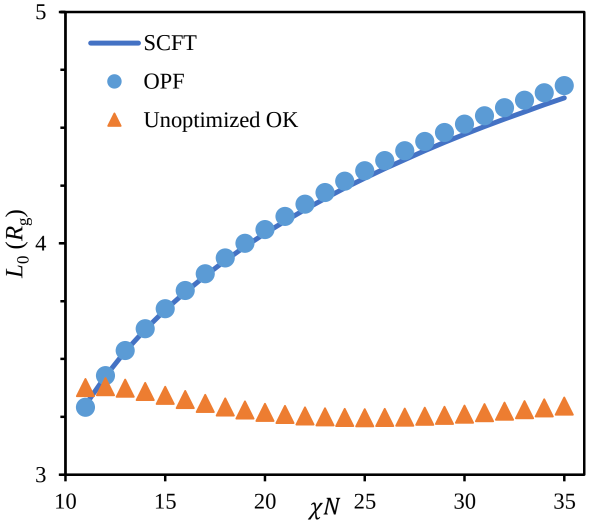

Figure 2.11: Predicted domain spacing L_0 in units of R_g versus χN for SCFT (solid line), the unoptimized OK model (triangles) and the OPF model (circles) for the lamellar phase in a symmetric diblock copolymer melt.

2.5 Conclusions

In this chapter, we developed phase field mapping, a method that can quickly and accurately parametrize an optimized phase field model using only a stress-free equilibrium configuration for the SCFT density ϕ^*. After the mapping is done once, the resulting model can be used as a substitute or partial substitute for SCFT to significantly reduce computation time. By investigating the mapped models, we identified useful metrics for gauging the quality of a phase field model, in particular, the error made by its equilibrium density fields and its predicted domain spacing L_0. Matching the domain spacing is especially important for making comparisons between two different states, since their relative stability can be strongly dependent on the size of the simulation cell, so we developed a mapping method to target the correct value of L_0.

We found that the force-matching method in our original formulation was effective at parametrizing coefficients in the Landau polynomial that dictates the amplitude of the density fields. Using only force-matching, however, we were unable to obtain sensible values for the semilocal and nonlocal coefficients in H_r that control the domain size (coefficients from our attempts often had the wrong sign according to simple analytical arguments). Adding a stress-matching term to the cost function rectified the issue. With this improved mapping procedure, we can successfully parametrize every coefficient in an OPF model and eliminate all dependence on values from the literature. The OPF model also predicts with high accuracy the same value of L_0 as SCFT (to within 1% for symmetric diblock melts).

A crucial element of a successful mapping is identifying a set of basis functionals for H_r that is a good approximation for H_e. Any inconsistencies will manifest as disagreements in the equilibrium density fields and lower the quality of the OPF model. We must always assess whether issues that we encounter with mapped models come from the basis set or from other aspects of the method, a situation that makes method development more difficult. As an example, a strong candidate for a useful basis functional is the mixing entropy $\int d\mathbf{r}\,\phi(\mathbf{r})\ln\phi(\mathbf{r})$, but it is complex-valued for negative ϕ, and its contribution to the force, $1+\ln\phi(\mathbf{r})$, diverges as ϕ approaches zero.

Of course, improving the basis set is also a difficult task, since there is no algorithmic way to do so (a similar problem exists in the exchange-correlation functionals of electronic density functional theory). Some ideas for other potentially useful basis functionals are:

- $\int d\mathbf{r}\,\frac{|\nabla\phi|^2}{\phi}$, the Lifshitz entropy, which appears in the ground state dominance (GSD) approximation [3] and as a generalized replacement for the square gradient term in various density functional theories [39], including the "improved" Ohta-Kawasaki model [40] and the gOK model [33] (there, it is expressed as $\int d\mathbf{r}\ |\nabla\psi|^2$, where $\psi = \sqrt{\phi}$);

- $\int d\mathbf{r}\,\phi\ln\phi$, the mixing entropy or configurational entropy from Flory-Huggins theory, which appears in the slow gradient expansion [3], in the DFT by Bohbot-Raviv and Wang [36], and in the gOK model [33];
- $\sum_{\mathbf{k}}\sum_{\mathbf{k}'}\ \hat{\Gamma}_3(\mathbf{k},\mathbf{k}')\widehat{\delta\phi}(\mathbf{k})\widehat{\delta\phi}(\mathbf{k}')\widehat{\delta\phi}(\mathbf{k}-\mathbf{k}')$, where $\hat{\Gamma}_3$ is the third-order vertex function Γ_3 from Leibler's RPA [27, 41], or some other nonlocal treatment of terms beyond quadratic order in ϕ.

Chapter 3

The optimized phase field model for the diblock copolymer melt

Now that we have a robust method for producing optimized phase field models, we explore deeper into numerical properties of the OPF model for the diblock copolymer melt. Whereas our goal in Chapter 2 was to analyze the phase field mapping method and improve it using feedback from model properties, now we leave the mapping method fixed (for the most part) and focus on the comparison between SCFT and our best OPF model.

3.1 Methods

The phase field mapping method for this study remains in the same form given in Section 2.4.1, but we will now also apply it to parametrize the model at asymmetric block fractions. Because the model for an AB diblock copolymer at any given block fraction $f = f_0$ is equivalent to a BA diblock copolymer with $f = 1 - f_0$, we need only consider the case $f \leq 0.5$. We will also later explore an alternate mapping produced from the SCFT configuration ϕ^*_{HEX}, an equilibrium state corresponding to the hexagonally-packed cylinder phase (HEX).

Let us discuss two aspects of our simulation code that we will use to benchmark the

OPF model: an efficient numerical relaxation strategy, the nonlinear conjugate gradient method, that will be used for timing comparisons to SCFT; and code optimizations around memory usage, that will dictate the maximum size of an OPF calculation. All of our simulation code was written in the `feature-PhaseFieldModels` branch of PolyFTS, the Fredrickson group's extensive and versatile central codebase for equilibrium field-theoretic simulations.

3.1.1 Nonlinear conjugate gradient method

The nonlinear conjugate gradient method is an efficient solver for high-dimensional optimization problems. As written in Chapters 1 and 2, our field theories are, in fact, infinite-dimensional, since a continuous field like $\phi(\mathbf{r})$ can be thought of as a vector

$$\boldsymbol{\phi} = \begin{bmatrix} \phi_1 \\ \phi_2 \\ \vdots \\ \phi_M \end{bmatrix} \tag{3.1}$$

in the limit that the number of points $M \to \infty$. Of course, to simulate field theories numerically, the fields must be discretized at M finite grid points. Since M can be larger than 10^6, finding an equilibrium solution for $\boldsymbol{\phi}$ (minimizing $H_\mathrm{r}(\boldsymbol{\phi})$) certainly qualifies as a high-dimensional problem and benefits greatly from conjugate gradients. In SCFT, the presence of a pressure-like field leads to a mixed saddle point problem and precludes the use of the conjugate gradient method.

For this study, we implemented a conjugate gradient solver based on the Polak-Ribière algorithm [42] to perform numerical relaxation, replacing our previous gradient descent-based method. We first discretize the field degrees of freedom so that H_r is now a function

$F(\boldsymbol{\phi})$ of the M-vector $\boldsymbol{\phi}$.

The key innovation of the conjugate gradient method is that the direction $\mathbf{p}^j$ for the j^{th} field update is chosen to be conjugate to all previous directions by a formula involving only the previous step. Two vectors $\mathbf{p}^j$ and $\mathbf{p}^k$ are mutually conjugate if

$$\mathbf{p}^{j\,T}(\nabla\nabla F)\mathbf{p}^k = 0. \tag{3.2}$$

This property is like orthogonality for the inner product weighted by the Hessian of F. In the Polak-Ribière method, the formula for the direction is

$$\mathbf{p}^j = -\nabla F_j + \beta_j \mathbf{p}^{j-1}, \tag{3.3}$$

where $\boldsymbol{\phi}^j$ is the field configuration for step j and ∇F_j is the discrete representation of the force $\frac{\delta H_{\mathrm{r}}[\phi]}{\delta\phi(\mathbf{r})}$ for step j. Notice that if $\beta_j = 0$, which should occur infrequently if ∇F is mostly linear in $\boldsymbol{\phi}$, the next direction $\mathbf{p}^j$ will be the steepest descent direction. In this case, we say that the history of conjugate directions has been reset. The scalar β_j is zero for $j = 0$ and otherwise given by

$$\beta_j = \max\left\{0, \frac{\nabla F_j^T(\nabla F_j - \nabla F_{j-1})}{||\nabla F_{j-1}||^2}\right\}. \tag{3.4}$$

To preserve conjugacy, the size of the step α_j taken in the $\mathbf{p}^j$ direction must be determined by line search (*i.e.*, minimization in one dimension). The minimization can be approximate as long as it satisfies the strong Wolfe conditions,

$$f(x) \leq f(0) + c_1 x f'(0) \tag{3.5}$$

$$|f'(x)| \leq -c_2 f'(0) \tag{3.6}$$

$$c_1 < c_2 < 0.5. \tag{3.7}$$

Here, the function to minimize is given by $f(x) = F(\boldsymbol{\phi}^j + x\mathbf{p}^j)$, and its derivative is $f'(x) = \mathbf{p}^{j\,T}\nabla F_j$. Then α_j will be the final value of x that we find by approximately minimizing f. Equation (3.5), the Armijo condition, ensures that f decreases sufficiently from its previous value. Equation (3.6) is known as the curvature condition and ensures that f' approaches zero sufficiently quickly.

We took $c_1 = 0.0001$ and $c_2 = 0.1$ and followed the line search algorithm laid out by Algorithms 3.5 and 3.6 in [42]. We do not attempt to reproduce all of the details here, only to give a rough overview. We first take small "blind steps" until we have bracketed the minimum. The first step size is chosen in some way using the minimizer of the previous line search, for example, by fitting two points and a slope to a quadratic function. Each subsequent blind step doubles the previous value of x. If we find that f is increasing or f' is positive, indicating that the minimum is bracketed between 0 and x, we switch to an interpolation strategy. We use the most recent known value of f and the two most recent known values of f' to fit $f(x)$ to a cubic polynomial and step directly to its minimum. We repeat this last step indefinitely to improve the accuracy of the minimum. At any point in the line search, including the blind steps, if the Wolfe conditions are met, we assign $\alpha_j = x$, terminate the line search, and compute the next conjugate direction. We end the optimization when the L^2 norm of the force ∇F is within a specified tolerance, usually 10^{-5}, or when the line search can no longer resolve differences between energies due to floating-point precision.

In reference [42], Nocedal remarks that it is often better to use an existing implementation of the line search than to write a new one because it is difficult to correctly implement the many important minutiae. We found this to be true, but chose to do so anyway, to make full use of the existing structure of PolyFTS and its `Field` class, which is efficiently designed for parallelization across multiple CPUs exploiting both shared and distributed memory or, most advantageously, for GPUs [43]. In Section 3.2.1, we characterize the performance of our conjugate gradient method relative to our most efficient numerical solvers for self-consistent field theory.

3.1.2 Monitoring memory usage

Running very large simulations can be expensive in terms of both computational time and memory usage. To reduce the former, we try to write code that uses efficient algorithms for a given task, such as fast Fourier transforms for applying matrix operations that are diagonal in Fourier space, or the nonlinear conjugate gradient method (rather than gradient descent methods) for high-dimensional optimization. For the latter, we try to reduce the amount of data that participates in any calculation and must be kept in memory. Whereas a simulation that is processor-intensive can be completed given enough compute time, a simulation that is too memory-intensive simply cannot be run without upgrading the hardware. Memory usage thus sets a strict upper limit on the accessible size of a simulation cell.

We counted the number of fields allocated during our simulations using a custom build of PolyFTS that defines two static class variables `Field::numFieldsAllocated` and `Field::maxFieldsAllocated`, updated in the constructor and destructor of the `Field` class. For a bulk simulation with $N_s = 100$ contour points, we found that SCFT must allocate 109 fields, most of which correspond to the propagator $q(\mathbf{r}, s)$ at different contour points s. We can then calculate the memory usage as the product of the memory required per floating point number, the number of grid points and the number of fields. For example, a calculation in a simulation cell with grid dimensions $768 \times 128 \times 40$ using complex-valued double-precision floating-point numbers in SCFT will require computer hardware with about $768 \times 128 \times 40 \times 16\,\mathrm{B} \times 109 = 6.8\,\mathrm{GB}$ of memory.

Because phase field simulations do not track the contour variable s, they do not need to store fields for each contour point. After being careful to allocate temporary fields only when needed, our implementation in PolyFTS requires 13 fields for any bulk simulation. Therefore, a phase field model calculation corresponding to the previous SCFT calculation would require only $768 \times 128 \times 40 \times 16\,\mathrm{B} \times 13 = 800\,\mathrm{MB}$ of memory. We can also conclude that, for a given amount of available memory, a phase field simulation in PolyFTS can access system volumes nine times as large as SCFT simulations.

3.2 Results

3.2.1 Computational efficiency

First, we briefly note the result of our benchmark testing for the computational efficiency of OPF calculations compared to SCFT calculations. On the same hardware, a single Intel Ivy Bridge CPU core, we ran serial calculations on a test problem (a symmetric diblock copolymer melt at $\chi N = 12$ with fields seeded from uniformly distributed random noise) with a spatial resolution of $M = 128 \times 128$ grid points. These conditions ensure that the computation time for each serial calculation is dominated by the cost of fast Fourier transform operations, as would be the case for an expensive large-cell calculation taking advantage of CPU or GPU parallelism [43]. Averaged over at least one hour of computation time and at least 10,000 field updates, we found that the time required per field update was 0.20 s for SCFT (using the SIS updater) and 0.011 s for the OPF model (using the Polak-Ribière conjugate gradient method). Thus, we expect that a field update for a large-cell bulk OPF calculation will complete roughly 20 times faster than a field update for the corresponding bulk SCFT calculation.

Note that to complete our characterization of the speed of the OPF model, we also need to estimate the number of field updates required to attain convergence. This number is strongly system-dependent and varies with relaxation parameters and initial conditions. We found that it is typically smaller for the conjugate gradient method than for the SCFT relaxation algorithms, further improving the relative performance of the OPF model.

As mentioned previously, not only are phase field models faster than SCFT, they are also less memory-intensive. For all of the simulations performed for this study, the chain contour in SCFT was resolved at 100 points. Under these conditions, we found that a bulk phase field calculation required roughly nine times less memory. Thus, given some amount of available memory, the largest accessible system size is nine times larger using a phase field model than using SCFT.

3.2.2 Optimized coefficients

Using a commensurate one-dimensional (lamellar) density profile from SCFT as ϕ^*, we performed phase field mapping to obtain model parameters $c_2, \ldots, c_6$ that represent the optimal values according to the metric of equation (2.18). Together with the basis set in equation (2.9b), these parameters define the optimized phase field model for the diblock copolymer melt. We repeated the mapping process at various points in the diblock copolymer phase space ($0.2 \leq f \leq 0.5$ and $10.6 \leq \chi N \leq 35$) for which the lamellar phase is at least metastable. Throughout this range, all of the parameters appear to be smooth functions of both variables. Figure 3.1 compares the mapped parameters and fitted curves to the Ohta-Kawasaki model parameters. In the weak segregation regime (near the spinodal), the mapped parameters recover similar values to the RPA and the OK model. As χN increases away from the spinodal, the optimized parameters diverge from the RPA values. In particular, we note that the ratio c_6/c_5, which plays a key role in setting the domain spacing, adjusts to reflect the information obtained from SCFT.

For convenience, we fit the OPF model parameters to simple analytic functions of f and χN using least-squares regression to the intermediate segregation data and taking advantage of the symmetry about $f = 0.5$:

$$c_2 = -\sum_{j=0}^{2}\sum_{k=0}^{2} b_{jk}^{(2)} x^j g^{2k} \tag{3.8}$$

$$c_3 = -\sum_{j=0}^{2}\sum_{k=0}^{2} b_{jk}^{(3)} x^j g^{2k+1} \tag{3.9}$$

$$c_4 = \sum_{j=0}^{2}\sum_{k=0}^{2} b_{jk}^{(4)} x^j g^{2k} \tag{3.10}$$

$$c_5 = \frac{\sum_{k=0}^{2}(b_{0k}^{(5)} + b_{1k}^{(5)} x) g^{2k}}{1 + \sum_{k=0}^{2} b_{2k}^{(5)} x g^{2k}} \tag{3.11}$$

$$c_6 = -c_2 / \sum_{j=0}^{2}\sum_{k=0}^{2} b_{jk}^{(6)} x^j g^{2k}. \tag{3.12}$$

Here, we have defined the block fraction asymmetry $g = 0.5 - f$ and the distance from the spinodal $x = \chi N - \chi N_s$, where χN_s is computed numerically from the RPA for each value of g (some values are shown in Table 3.1). The parameters $b_{jk}^{(i)}$ appearing in equations (3.8)–(3.12) are listed in Table 3.2. These expressions are valid in the region $0.2 \leq f \leq 0.8$ and $10.6 \leq \chi N \leq 35$ (provided $\chi N > \chi N_s$). Values indicated by a dash were set to zero manually because they did not significantly impact the quality of the fit.

As Figure 3.1 shows, the regression is in good agreement with the original data throughout, particularly in the intermediate segregation regime. In Figure 3.2, we plot the residuals from the fit and find that the error made by the regression is within 2% in intermediate segregation. Although the individual coefficients show some discrepancy in the weak segregation regime, the ratio c_6/c_5 is still accurate to within 5%. The regression thus retains the advantage of the OPF model over the OK model, as we discuss next.

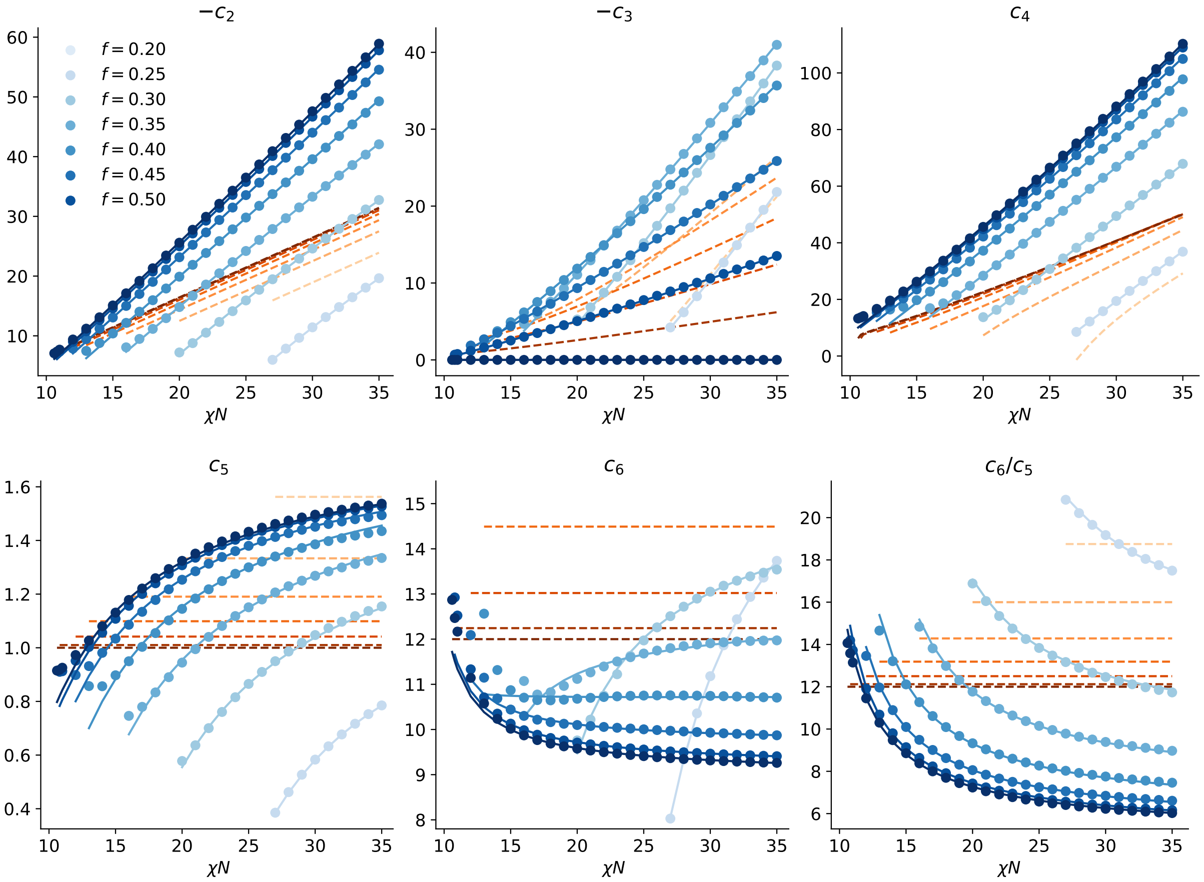

Figure 3.1: From left to right: OPF model parameters $-c_2$, $-c_3$, c_4, c_5, c_6, and the ratio c_6/c_5 as functions of χN for block fractions f from 0.5 (darkest) to 0.2 (lightest) obtained from phase field mapping (points), the regression (solid lines), and values from the Ohta-Kawasaki model (dashed lines).

Table 3.1: RPA spinodal conditions for the diblock melt.

$\|g\|$	χN_s
0.00	10.495
0.05	10.698
0.10	11.344
0.15	12.562
0.20	14.635
0.25	18.172
0.30	24.613
0.35	38.038

Table 3.2: Diblock copolymer OPF model parameters.

		$k=0$	$k=1$	$k=2$
$b^{(2)}_{jk}$	$j=0$	5.920	-14.31	398.5
	$j=1$	2.025	-4.285	39.47
	$j=2$	0.005522	-0.1915	-1.003
$b^{(3)}_{jk}$	$j=0$	9.741	-39.46	-999.0
	$j=1$	9.224	14.69	-510.3
	$j=2$	0.06433	-1.281	15.70
$b^{(4)}_{jk}$	$j=0$	9.686	53.00	-1775.
	$j=1$	36	–	–
	$j=2$	0.02068	-0.2385	-0.4559
$b^{(5)}_{jk}$	$j=0$	0.7853	-5.654	-16.22
	$j=1$	0.2356	-1.170	3.659
	$j=2$	0.1185	-0.7423	5.481
$b^{(6)}_{jk}$	$j=0$	0.5	–	–
	$j=1$	0.2357	-1.956	7.147
	$j=2$	0.0006666	-0.02858	0.05316

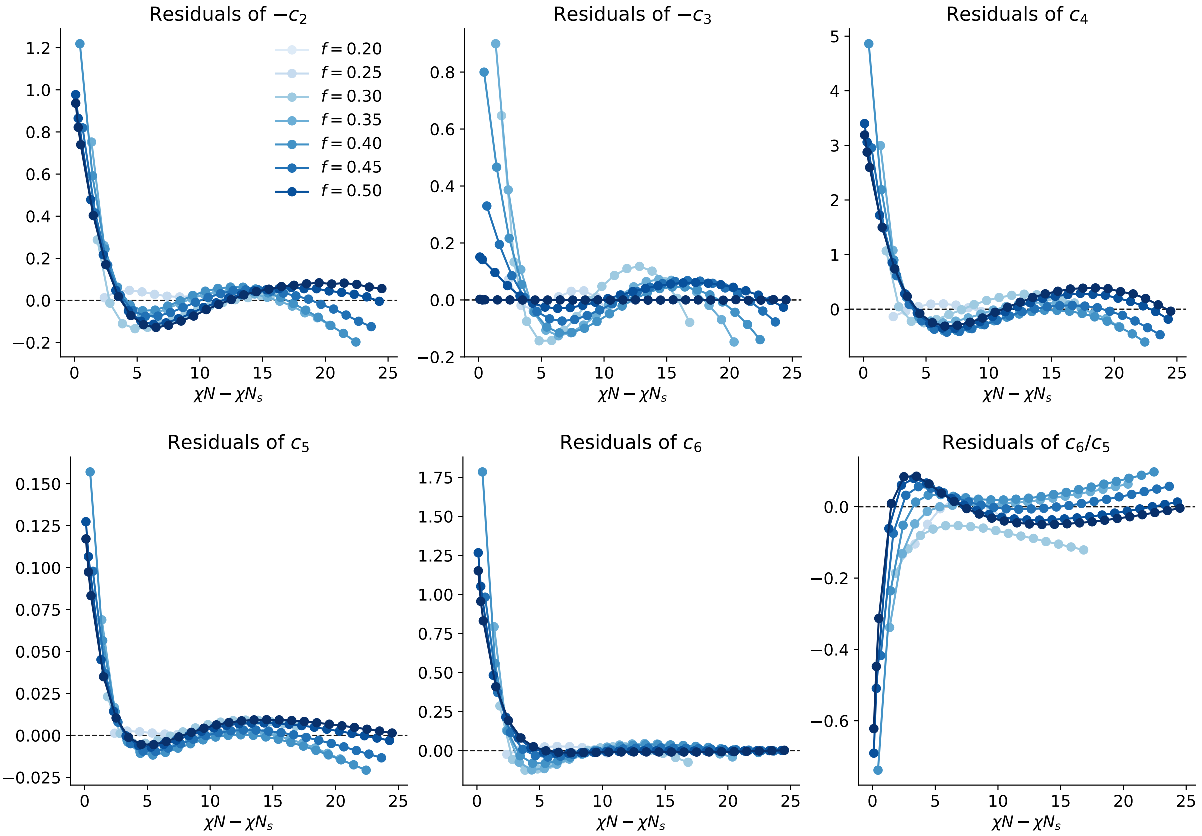

Figure 3.2: From left to right: residuals of OPF model parameters $-c_2$, $-c_3$, c_4, c_5, c_6, and the ratio c_6/c_5 as functions of χN for block fractions f from 0.5 (darkest) to 0.2 (lightest) from regression to data obtained by phase field mapping.

3.2.3 Density fields

Now that we have generalized the model to asymmetric block fractions, it is worth revisiting the density profiles to see how well the OK-type models perform with $c_3 \neq 0$. Figure 3.3 shows stress-free equilibrium density fields for the lamellar phase predicted by SCFT, the OK model and the OPF model at small and large asymmetries. Because we know that the OK model makes poor predictions of $L_{0,\mathrm{SCFT}}$, here we allowed each model to use a periodic cell with its own commensurate domain spacing, unlike in Section 2.3 where we enforced $L = L_{0,\mathrm{SCFT}}$. As expected, the OPF model is consistently closer to SCFT than the OK model in terms of both density profile and L_0 value. As χN or the asymmetry increase, though, neither phase field model captures the shape of ϕ well.

Note that, in spite of the shape only partially matching SCFT, phase field models still describe the interfaces well enough to predict the existence of other equilibrium morphologies like hexagonally-packed cylinders (HEX) and the bicontinuous double gyroid (GYR), as we will discuss in Section 3.2.7.

3.2.4 Domain spacing

Next, we expand our results from Figure 2.11 to study the effects of asymmetric block fractions on predictions of the lamellar domain spacing L_0 for OPF and OK models. Note that as the diblock becomes more asymmetric, the stability of the lamellar phase gradually decreases relative to other morphologies like GYR and HEX. Each morphology will have a different lattice spacing that we would also like to reproduce. We defer this to the discussion of transferability in Section 3.2.7 and focus for now on the lamellar domain spacing L_0. We are interested in matching both its magnitude and its scaling with $N^{\alpha-0.5}$, where α is approximately 1 just above the spinodal and gradually decreases towards $\frac{2}{3}$ as χN increases [37]. Note that this scaling is given for L_0 in units of R_g—if

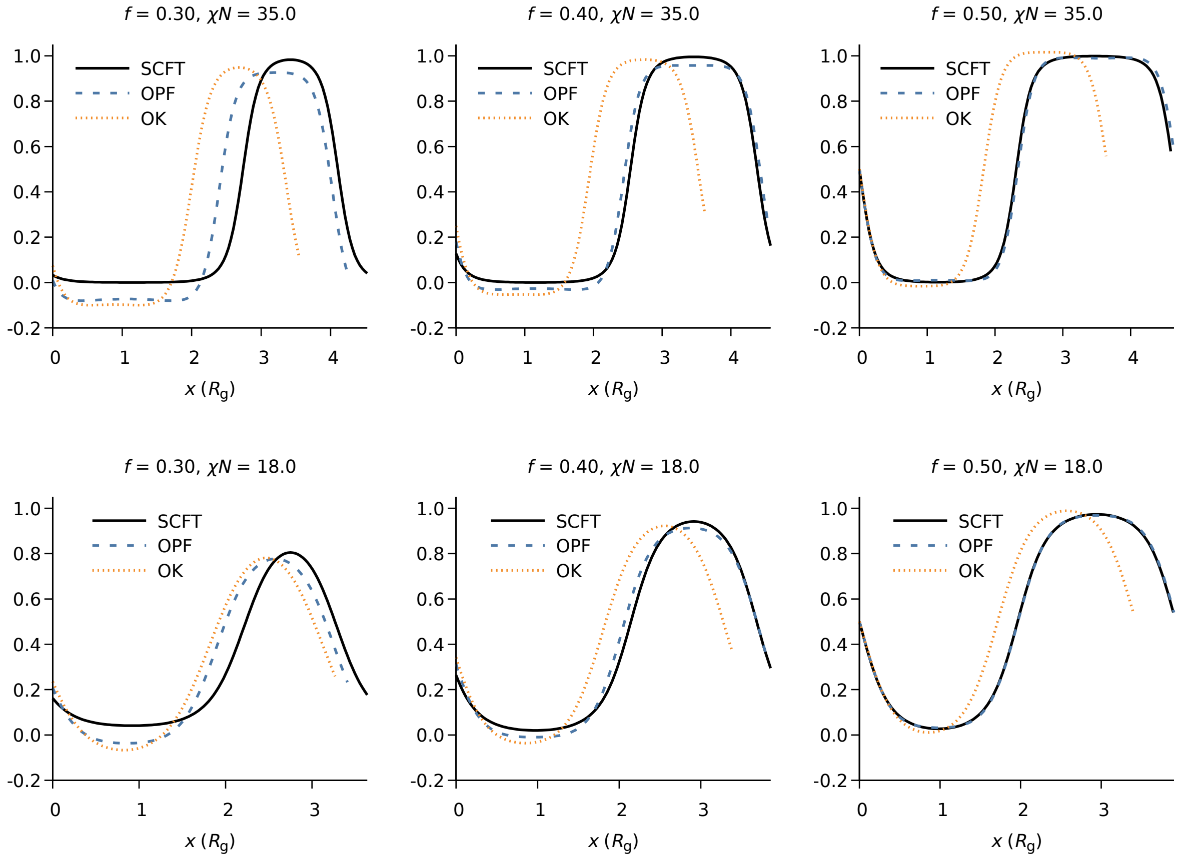

Figure 3.3: Stress-free equilibrium density fields for the OK (solid blue) and OPF models (dashed orange) and SCFT (solid black). From left to right, plots correspond to $f = 0.3$ (large asymmetry), $f = 0.4$ (small asymmetry), and $f = 0.5$ (no asymmetry). The top row corresponds to $\chi N = 35$, and the bottom row to $\chi N = 18$. Because we know that the OK model makes poor predictions of $L_{0,\mathrm{SCFT}}$, here we allowed each model to use a periodic cell with its own commensurate value of L_0, unlike in Section 2.3.

lengths are written in dimensional units, the relation becomes $L_0/R_{\mathrm{g}} \sim N^{\alpha}$.

We minimized H_V and $H_{\mathrm{r},V}$ with respect to the simulation cell size to obtain predictions of L_0 for SCFT, for the OPF model, and for the OK model throughout the range of f and χN described above. We then computed the signed fractional error η made by each phase field model relative to SCFT, given by

$$\eta = \frac{L_{0,\mathrm{PF}} - L_{0,\mathrm{SCFT}}}{L_{0,\mathrm{SCFT}}}. \tag{3.13}$$

Figure 3.4 shows that the OK model fails to capture the scaling of L_0 as χN increases. We attribute this to several approximations in the model. The asymptotic expansion of the RPA may not be appropriate at intermediate segregation, where density perturbations are no longer small. Neglecting the nonlocal behavior from the third- and fourth-order RPA vertex functions will also distort predictions of L_0. Furthermore, approximating the second-order vertex function by its limiting behavior for small and large wavevectors causes k^* to be incorrect (according to equation (2.12b)), and thus the model overestimates L_0 even in the weak segregation limit where the RPA is valid. On the other hand, by modifying the ratio c_6/c_5 as χN increases, the OPF model provides qualitative and sometimes quantitative agreement with SCFT, especially for block fractions near symmetry where the lamellar phase is globally stable. It also correctly captures the scaling of L_0 with increasing N: the error quickly approaches a constant value as χN increases above the spinodal.

3.2.5 Defect states

We now study the performance of the OPF model in defective thin films in the weak and intermediate segregation regimes. We ran two-dimensional calculations to produce defective metastable structures $\phi^*_{\mathrm{d,SCFT}}$ using SCFT at two values of χN. At $\chi N = 12$,

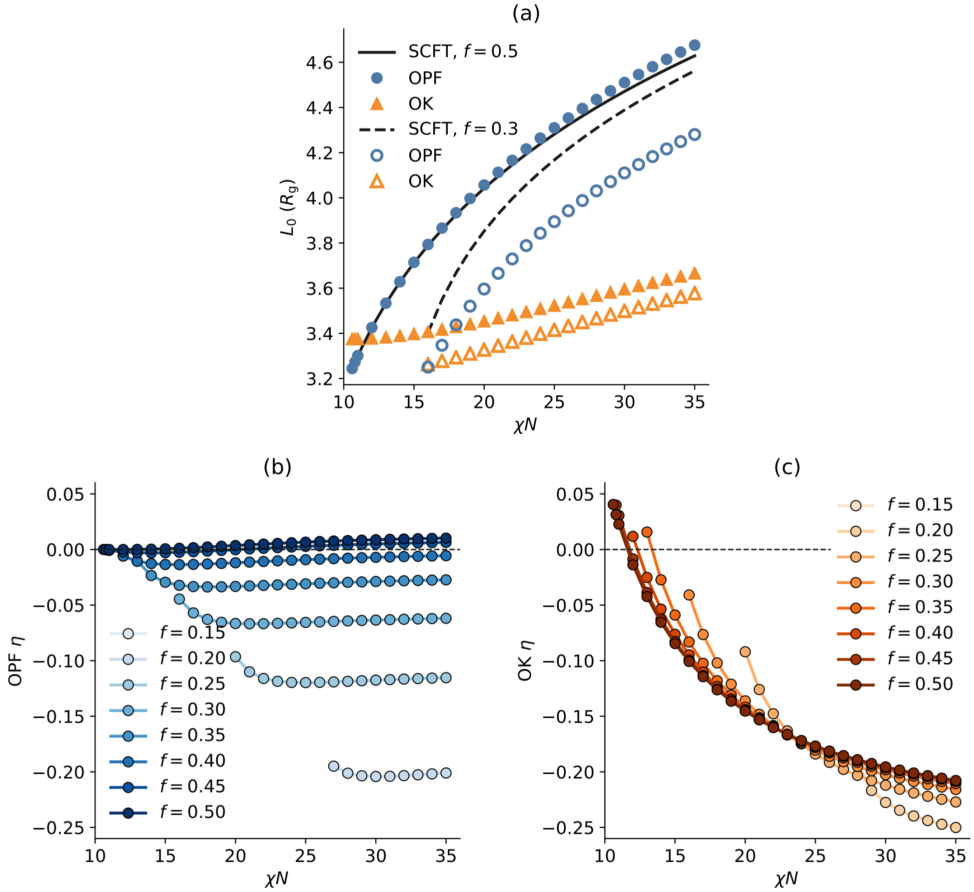

Figure 3.4: (a) Predicted domain spacing L_0 in units of R_g for SCFT at $f = 0.5$ (solid line) and at $f = 0.3$ (dashed line), for the OPF model at $f = 0.5$ (closed circles) and at $f = 0.3$ (open circles), and for the OK model at $f = 0.5$ (closed triangles) and at $f = 0.3$ (open triangles). (b)–(c) Error η (see Equation (3.13)) in the lamellar domain spacing predicted by two phase field models, (b) the OPF model and (c) the Ohta-Kawasaki model, functions of χN for various values of f.

we used a resolution of 512 × 512 plane waves for an 82 R_g × 82 R_g simulation cell (corresponding approximately to 400 nm × 400 nm for a PS-*b*-PMMA diblock copolymer with molecular weight 72 kg/mol [44]). At $\chi N = 25$, we used a resolution of 128 × 128 plane waves for a 16 R_g × 16 R_g simulation cell (or 120 nm × 120 nm for PS-*b*-PMMA).

Next, we relaxed the unoptimized OK and OPF models to their respective local minima $\phi^*_{\mathrm{d,OK}}$ and $\phi^*_{\mathrm{d,OPF}}$ using as initial conditions the previously obtained states $\phi^*_{\mathrm{d,SCFT}}$ to determine whether they remain valid metastable states in the approximate models. Figures 3.5 and 3.6 show representative samples of the results. The defect states found in SCFT do not correspond to similar metastable states in the unoptimized OK model: in the large-cell simulations at $\chi N = 12$, many defective regions are changed or removed entirely, and at $\chi N = 25$, the OK model tends to shrink domains to its predicted domain size. On the other hand, the OPF model predicts similar features and domain sizes as those in the SCFT defect states throughout.

Finally, we study predictions of defect formation energies. We define the defect formation energy ΔF of a state ϕ^*_d with respect to a reference energy corresponding to the perfect configuration ϕ^*_p, regularly aligned commensurate lamellae:

$$\Delta F_{\mathrm{SCFT}} = H[w^*_A, w^*_B, \phi^*_{\mathrm{d,SCFT}}] - H[w^*_A, w^*_B, \phi^*_{\mathrm{p,SCFT}}] \tag{3.14}$$

for SCFT, or

$$\Delta F_{\mathrm{PF}} = H_\mathrm{r}[\phi^*_{\mathrm{d,PF}}] - H_\mathrm{r}[\phi^*_{\mathrm{p,PF}}] \tag{3.15}$$

for a phase field model. To compute this extensive quantity in units of $k_B T$, we assume a film thickness of 4 R_g and a chain density of 3.1 R_g^{-3}, corresponding to a PS-*b*-PMMA diblock copolymer with a molecular weight of 72 kg/mol, a monomer density of 1 g/cm^3,

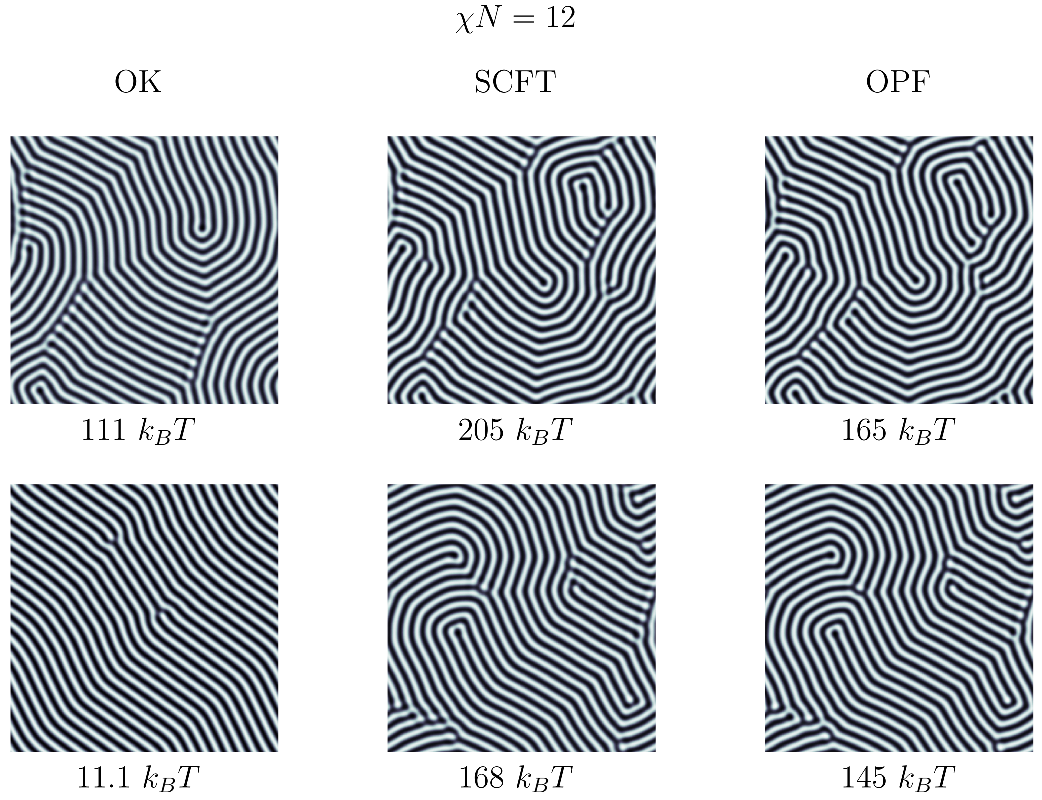

Figure 3.5: Defective structures predicted by the unoptimized OK model (left column), SCFT (center column), and the OPF model (right column) in weak segregation (at $\chi N = 12$) in an 82 R_g × 82 R_g simulation cell and their corresponding defect formation energies.

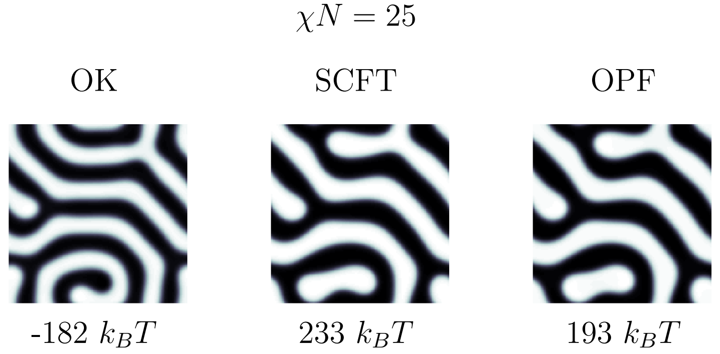

Figure 3.6: Defective structures predicted by the unoptimized OK model (left), SCFT (center), and the OPF model (right) in intermediate segregation (at $\chi N = 25$) in a 16 R_g × 16 R_g simulation cell. Models predicted defect formation energies of -182, 233, and 193 k_BT, respectively. Note that the unoptimized OK model predicts this configuration to be more stable than perfectly ordered lamellae.

and a radius of gyration $R_{\mathrm{g}} = 7.2$ nm [44]. Figure 3.7 compares the phase field model defect formation energies to the exact SCFT values over ten simulations at $\chi N = 12$ and over five simulations at $\chi N = 25$. Note that the diagonal line corresponds to a perfect match between SCFT and the phase field model defect formation energy. In all cases, the OPF model is a significant improvement over the unoptimized OK model. At $\chi N = 12$, the OPF model typically makes errors of 14%, whereas the OK model typically makes errors of 47%. At $\chi N = 25$, due to the drastic mismatch in L_0, the unoptimized OK model predicts negative defect formation energies, *i.e.*, it predicts that the defect is more stable than perfectly placed lamellae.

We point out that the inaccuracy of the unoptimized OK model is largely due to the disagreements between their equilibrium density fields $\phi^*_{\mathrm{d,OK}}$ and $\phi^*_{\mathrm{d,SCFT}}$. However, even if we remove this effect by defining an alternate defect formation energy that simply evaluates the energy at $\phi^*_{\mathrm{d,SCFT}}$ (which is not a local minimum in H_{r}), *i.e.*,

$$\Delta F^{\dagger}_{\mathrm{PF}} = H_{\mathrm{r}}[\phi^*_{\mathrm{d,SCFT}}] - H_{\mathrm{r}}[\phi^*_{\mathrm{p,SCFT}}] \tag{3.16}$$

we still consistently find large errors from the OK model. We show this now using the relative errors

$$x = \frac{|\Delta F_{\mathrm{PF}} - \Delta F_{\mathrm{SCFT}}|}{\Delta F_{\mathrm{SCFT}}} \tag{3.17}$$

$$x^{\dagger} = \frac{\left|\Delta F^{\dagger}_{\mathrm{PF}} - \Delta F_{\mathrm{SCFT}}\right|}{\Delta F_{\mathrm{SCFT}}} \tag{3.18}$$

for each phase field model. We collected statistics on its mean, standard deviation, minimum and maximum values from the points in Figure 3.7. Table 3.3 shows the results for each data set. Even using the alternate definition of the defect formation energy in $x^{\dagger}$, the OK model still makes over twice the error of the OPF model.

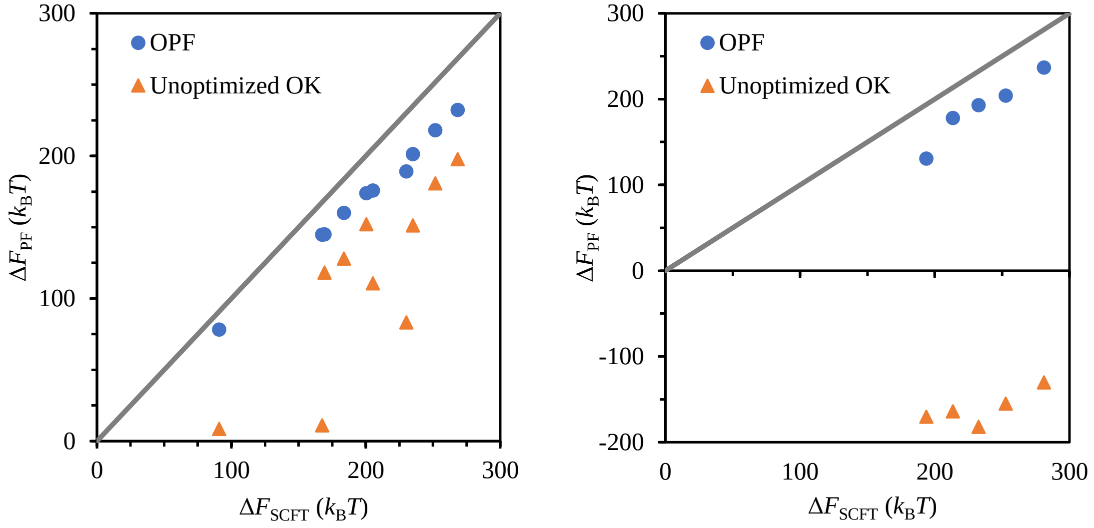

Figure 3.7: Defect formation energies predicted by the unoptimized OK (orange triangles) and OPF models (blue circles) compared to SCFT. Each point represents a simulation of a different metastable defect, at $\chi N = 12$ (left) or at $\chi N = 25$ (right).

Table 3.3: Statistics for the errors in defect formation energy predictions.

		OPF x	OK x	OPF $x^\dagger$	OK $x^\dagger$
$\chi N = 12$	Mean	0.14	0.47	0.086	0.21
	Std. dev.	0.014	0.27	0.0052	0.17
	Minimum	0.13	0.24	0.079	0.081
	Maximum	0.18	0.93	0.097	0.66
$\chi N = 25$	Mean	0.20	1.7	0.078	0.58
	Std. dev.	0.070	0.16	0.015	0.054
	Minimum	0.16	1.5	0.063	0.49
	Maximum	0.33	1.9	0.10	0.63

3.2.6 Defect annihilation and kinetic barriers

For many applications, a pure ordered state serves only as a reference, while the main focus of study are defect states and their associated energies. In a previous study, we showed that the OPF model can consistently predict the same types of lamellar defect states as SCFT. We also showed that at $f = 0.5$ and $\chi N = 25$, the OPF model predicts defect formation energies that are within 20% of the SCFT values, whereas the OK model predicts energies with the wrong sign [38]. Here, we extend our analysis of the

OPF model to kinetic pathways for defect annihilation.

A number of studies have investigated kinetic effects in SCFT by applying the string method [45, 14, 15, 16, 46]. To do this, we use the mean-field approximation to construct a free energy landscape $F[\phi] = H[w_A^*, w_B^*, \phi]$ that allows arbitrary configurations for the density field ϕ while relaxing the remaining fields to values stationary in H. For the OPF model, the analogous free energy functional is simply $F[\phi] = H_{\mathrm{r}}[\phi]$. We then use the string method [47] to compute a minimum energy path (MEP) connecting two states, such as a metastable defect ϕ_d and the stable perfect lamellar configuration ϕ_p. This MEP consists of a continuous curve of configurations $\phi(\alpha)$ beginning at $\phi(0) = \phi_d$ and ending at $\phi(1) = \phi_p$, such that the entire curve is always parallel to the force ∇F. That is,

$$(\nabla F)^{\perp}(\phi(\alpha)) = 0, \tag{3.19}$$

where the arclength α is a distance defined by the L^2 norm of ϕ, normalized to 1, and $(\nabla F)^{\perp}$ represents the component of the force normal to $\phi(\alpha)$. Along the MEP, the free energy is maximized at an intermediate barrier state ϕ^* with energy $F[\phi^*]$. Given this information, we can estimate the barrier crossing frequency as proportional to $e^{-E_b/kT}$, where the barrier height is $E_b = F[\phi^*] - F[\phi_d]$.

To validate the OPF model, we replicated an SCFT calculation from Takahashi et al. for the annihilation of a disclination defect in a lamellar diblock copolymer melt [14]. We chose to study the most relevant melting pathway (the one predicted to have the lowest energy barrier), an asymmetric pathway that passes through a second metastable state, a dislocation defect. To avoid the use of confining walls on the top and bottom of the system, which would require additional methods and a generalization of the OPF model [24], we use periodic boundary conditions as usual, but surround the defect region with additional nondefective lamellae. These are meant to stabilize the system against finite size effects by isolating the defect from the edges of the cell. Our version of this system contains seven commensurate lamellar periods at $f = 0.5$ and has dimensions of $6\ L_0 \times 7\ L_0$. At $\chi N = 25$, this corresponds to $25.7\ R_{\mathrm{g}} \times 30.0\ R_{\mathrm{g}}$. As done in reference [14], to obtain extensive energies, we assume a film thickness of $4\ R_{\mathrm{g}}$ and a chain density of $3.1\ R_{\mathrm{g}}^{-3}$, corresponding to a PS-b-PMMA diblock copolymer with a molecular weight of 72 kg/mol, a monomer density of 1 g/cm^3, and a radius of gyration $R_{\mathrm{g}} = 7.2$ nm.

Figure 3.8 compares the minimum energy pathways predicted by SCFT and the OPF model for asymmetric melting of the disclination defect at $\chi N = 25$. Qualitatively, the two models are in strong agreement for the entire MEP. Both models predict MEPs containing two barriers (local maxima), and snapshots of the density fields along the string are indistinguishable between the two models. At the first transition state, the polymer chains rearrange to form a narrow bridge across the break in the lower lamella (for SCFT: $E_b = 2.7\,kT$; for OPF: $E_b = 10.\,kT$). Next, we find a local minimum representing a dislocation defect. A second bridge then forms to repair the remaining broken lamella (for SCFT: $E_b = 5.0\,kT$; for OPF: $E_b = 20.\,kT$). This second transition state gradually heals to the perfect lamellar state at $\alpha = 1$. We see a slight finite size error in the intermediate states: in spite of the extra lamellae surrounding the defect, the defect still interacts slightly with the ends of the cell, as evidenced by a slight tilting of the lamellae most distant from the asymmetric defect.

Although the qualitative shape of the MEP is captured by the OPF model, the OPF model underestimates the formation energy for the defect $F(0)$ by about 20%, just as in our previous work. We also find that the OPF model significantly overestimates the barrier heights for both the disclination and dislocation. We further investigated these trends by repeating the string calculation for different values of χN for which the disclination remained metastable (down to $\chi N = 20$). Figure 3.9 shows the resulting defect formation energies and barrier heights as a function of χN. We observe that

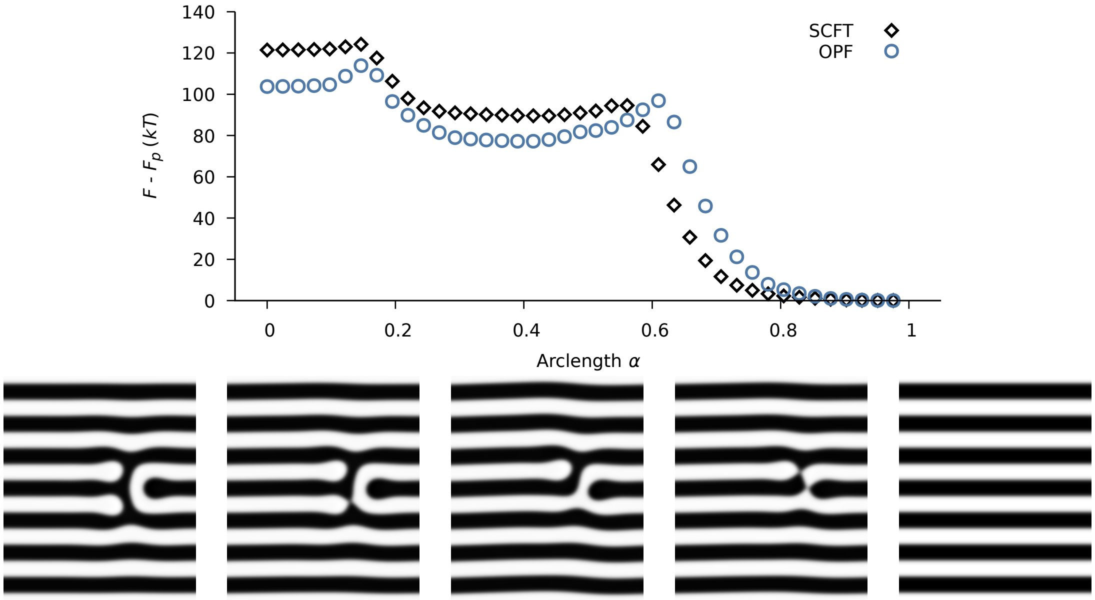

Figure 3.8: Top: Minimum energy pathway for the annihilation of a disclination defect in a lamella-forming diblock copolymer melt with $\chi N = 25$ and $f = 0.5$ as found in SCFT (diamonds) and the OPF model (circles). Bottom, left to right: snapshots of density profiles along the MEP from the OPF model (visually indistinguishable from SCFT) corresponding to the local extrema of F.

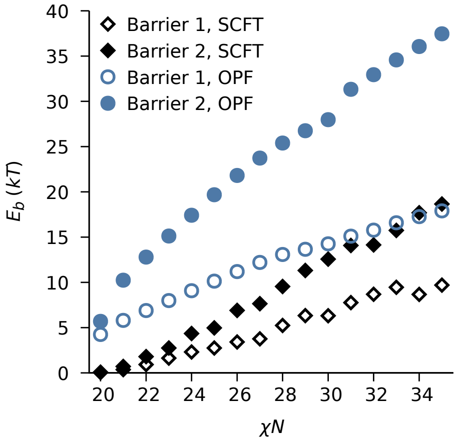

Figure 3.9: Energy barriers E_b for the melting of disclination (open shapes) and dislocation (closed shapes) defects versus χN as predicted by SCFT (diamonds) and the OPF model (circles).

the OPF model correctly predicts increases in E_b with χN, but that it consistently overestimates its magnitude. It may also allow both defects to remain metastable for smaller values of χN where SCFT will indicate they are unstable.

3.2.7 Transferability across different morphologies

We have demonstrated that the OPF model produced by mapping from the commensurate lamellar choice for ϕ^* can be used to study defects and transition states. Is the lamellar mapping still valid for studying a different morphology? We studied the hexagonally-packed cylinder (HEX) phase and the gyroid (GYR) phase using SCFT, the OK model and the OPF model from Table 3.2. By minimizing H_V and $H_{\mathrm{r},V}$ with respect to the simulation cell size, we obtained predictions for the domain spacing for the HEX phase $L_{0,\mathrm{HEX}}$, defined as the side length of a rhombic unit cell (equivalent to the shortest center-to-center distance between cylinders), and for the GYR phase $L_{0,\mathrm{GYR}}$, defined as the side length of the cubic unit cell. Figures 3.10 and 3.11 compare the errors η_{HEX} and η_{GYR} made by the OPF model and by the OK model relative to SCFT. As in the lamellar case, the OPF model qualitatively captures the correct magnitudes of $L_{0,\mathrm{HEX}}$ and $L_{0,\mathrm{GYR}}$ both in the weak segregation and intermediate segregation regimes, whereas the OK model does not. For both the HEX and GYR phases, the OPF model performs best for block fractions near $f = 0.3$, where $L_{0,\mathrm{HEX}}$ is accurate to within 4%. This result is especially encouraging as HEX and GYR become the globally stable phase near these conditions.

An alternate approach to studying the HEX phase is to redo the mapping from an SCFT configuration for the same phase, ϕ^*_{HEX}. For points in the phase space where the HEX phase was at least metastable, we used phase field mapping to obtain another set of values for the model parameters that we will refer to as OPF-HEX. Note that the OPF-

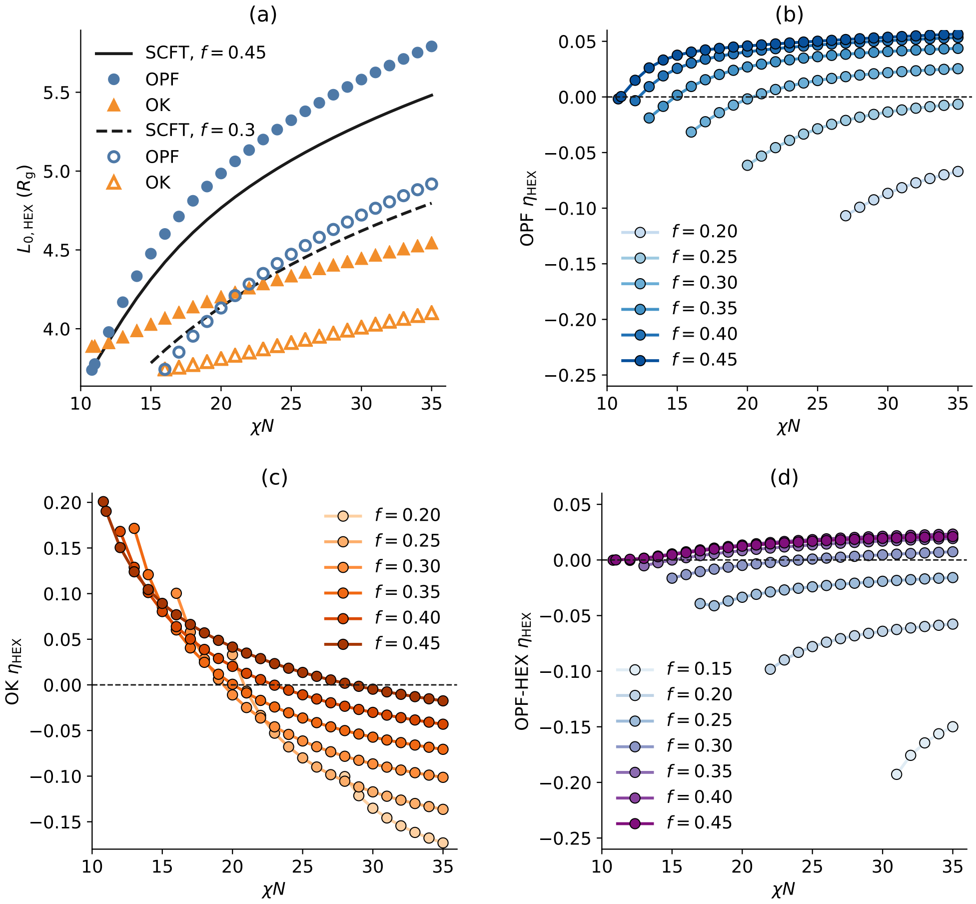

Figure 3.10: (a) Predicted domain spacing $L_{0,\mathrm{HEX}}$ in units of R_{g} for SCFT at $f = 0.45$ (solid line) and at $f = 0.3$ (dashed line), for the OPF model at $f = 0.45$ (closed circles) and at $f = 0.3$ (open circles), and for the OK model at $f = 0.45$ (closed triangles) and at $f = 0.3$ (open triangles). (b)–(d) Error η_{HEX} in the cylindrical domain spacing predicted by phase field models, (b) the OPF model, (c) the Ohta-Kawasaki model, and (d) the OPF-HEX model, as functions of χN for various values of f.

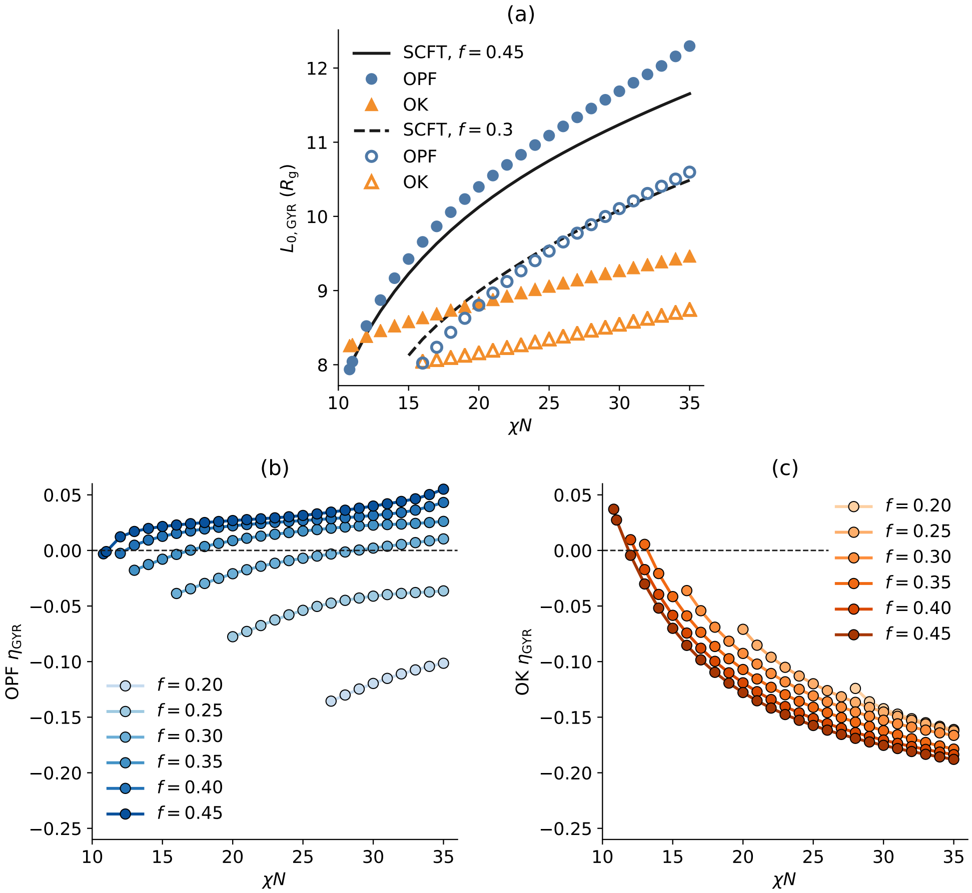

Figure 3.11: (a) Predicted domain spacing $L_{0,\mathrm{GYR}}$ in units of R_g for SCFT at $f = 0.45$ (solid line) and at $f = 0.3$ (dashed line), for the OPF model at $f = 0.45$ (closed circles) and at $f = 0.3$ (open circles), and for the OK model at $f = 0.45$ (closed triangles) and at $f = 0.3$ (open triangles). (b)–(c) Error η_{GYR} in the gyroid phase domain spacing predicted by two phase field models, the OPF model (center) and the Ohta-Kawasaki model (right), as functions of χN for various values of f.

HEX mapping extends to $f = 0.15$, since the HEX phase remains metastable for stronger asymmetries than the lamellar phase, but it could not be parametrized for the symmetric case $f = 0.5$. The coefficient values differ somewhat from the lamellar mapping but still follow similar trends in χN and f; the data are shown in Figure 3.12.

We computed values of $L_{0,\mathrm{HEX}}$ predicted by the OPF-HEX mapping. The resulting error with respect to SCFT is shown in Figure 3.10(d). As expected, because the OPF-HEX model was trained in the HEX geometry, it tends to make slightly better predictions of $L_{0,\mathrm{HEX}}$ than the lamellar mapping. Still, the original mapping obtained simply from a one-dimensional SCFT calculation performs comparably well for block fractions near $f = 0.30$.

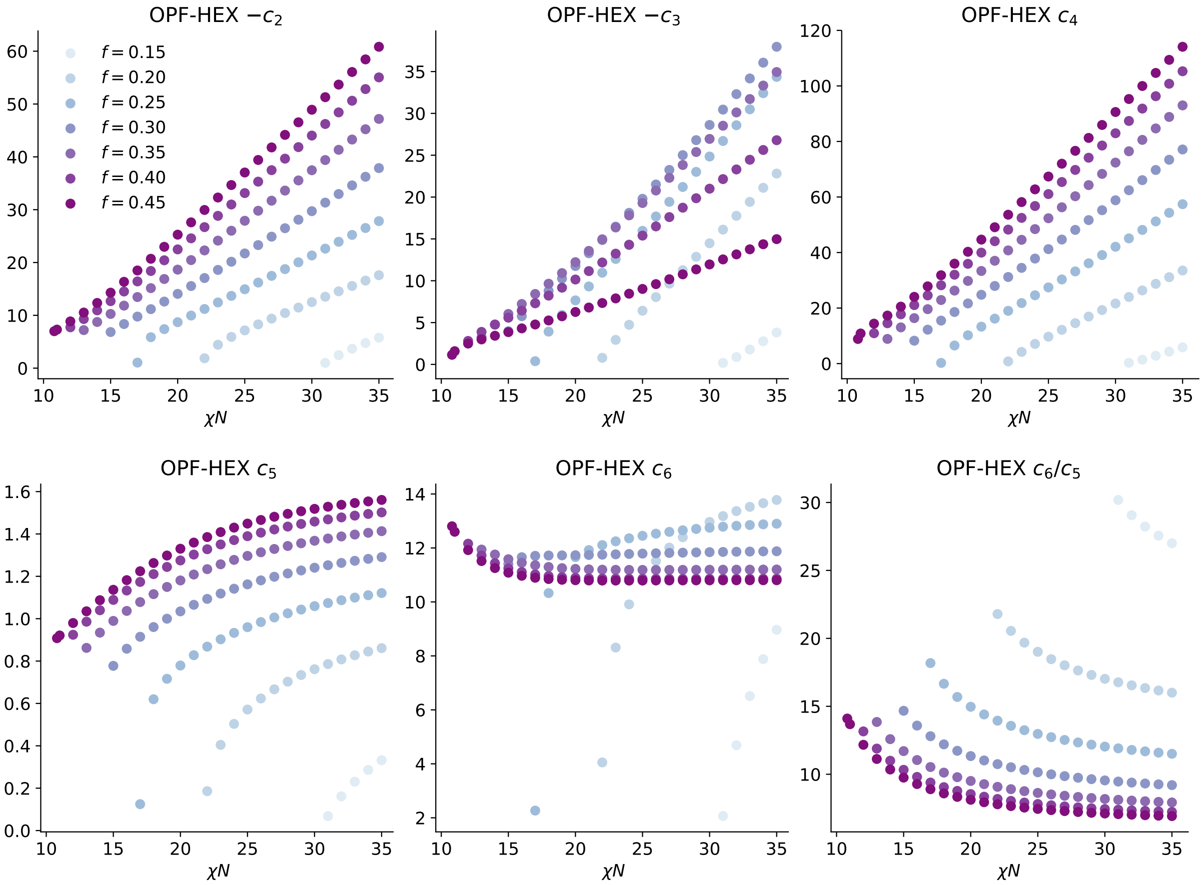

Figure 3.12: From left to right: OPF-HEX model parameters $-c_2$, $-c_3$, c_4, c_5, c_6, and the ratio c_6/c_5 as functions of χN for block fractions f from 0.5 (darkest) to 0.2 (lightest) obtained from phase field mapping (points) and values from the Ohta-Kawasaki model (dashed lines).

3.3 Conclusions

In this chapter, we studied in detail the numerical properties of the OPF model, our best phase field model so far. We found that it is fast—OPF simulations can be completed roughly one to two orders of magnitude faster than corresponding SCFT simulations, thanks to the elimination of the modified diffusion equation for the propagators and to a nonlinear conjugate gradient solver. We can also simulate systems about nine times larger using OPF simulations than SCFT.

The OPF model is qualitatively and sometimes quantitatively accurate in predictions of density fields, length scales, and defect formation energies, more so than the OK model. We were even able to find a defect melting pathway that aligns nicely to the SCFT result. The quality of the model is highest for symmetric diblocks and decreases as f deviates from 0.5. We interpret this as an indication that the basis set (2.9b) is poor for describing asymmetric diblocks—there must be significant terms in H_{e} that are absent from our approximation and that vanish on symmetry.

We find it likely that identifying new terms to add to H_{r} that capture these density profiles will lead to further improvements in other aspects of the model, such as its phase behavior. A possible lead is to introduce some semilocal or nonlocal character at cubic (and higher) order in ϕ, for example, the Lifshitz entropy, $\int d\mathbf{r}\, \frac{|\nabla\phi|^2}{\phi}$.

We point out that even if the OPF model is not quantitatively accurate, it can still be used in a multiscale approach in combination with SCFT. To speed up the overall calculation, we can perform an initial relaxation using the OPF model, then use the resulting fields as the starting point for an SCFT simulation.

Chapter 4

Phase field models in confinement

An attractive application for OPF models is directed self-assembly (DSA), a patterning technique for semiconductor device manufacturing that produces controlled features on length scales on the order of 10 nanometers. The name comes from the fact that, although a block copolymer melt below its spinodal temperature will spontaneously self-assemble to an ordered structure, we can direct the type of pattern that is formed by carefully choosing conditions for the environment surrounding the polymer, like the geometry of the walls and the affinity of each wall to each monomer type, often referred to as the wetting conditions. Of course, as usual, we can also manipulate polymer properties like the block architecture and composition to obtain different patterns. The design space for a confined polymer system is thus even larger than for a bulk polymer system. Furthermore, it is generally not enough to study one equilibrium configuration ϕ^* for each design condition. We must also look at a collection of possible defective metastable states and try to characterize how likely they are to occur. To optimize a process for DSA, therefore, we must have a thorough understanding of all of these considerations: the thermodynamics of the self-assembling polymer, parameters for the confining walls, stability and defectivity.

A number of studies have used SCFT to study various templates and patterns for DSA [11, 12, 13, 48, 14, 15, 46, 16, 17, 18], producing results in good agreement with experiments [49, 3, 50]. These studies employ a wall masking strategy [51, 11] that introduces a new field for the wall density ϕ_w. The wall density interacts with the polymers in two ways: through the compressibility (equation (1.9) for the incompressible model or (1.10) for the weakly compressible model), and through a new enthalpic term analogous to the χ interaction term. The first type of interaction is associated with graphoepitaxy, in which walls are used as arbitrarily complicated effective boundary conditions to confine the polymer; the second is associated with chemoepitaxy, in which surface interactions cause preferential wetting of one monomer type (or the other, or neither) to direct polymer self-assembly. In general, both interactions are present and play a role.

In this chapter, we attempt to develop a phase field model compatible with the wall masking method and analogous to the successful confined SCFT model. Our confined OPF model should extend the computational advantages of the OPF model to confined systems. We discover that several steps are required to make this happen. First, we formulate a compressible version of the model, and validate the result against the bulk incompressible OPF model. We then introduce the wall masking method and motivate the need for more modifications to the OPF model. Then we define a variable transformation for the density fields to impose a physical constraint necessary in confinement. Throughout, we test our modifications against SCFT in some simple confined systems.

4.1 Methods

4.1.1 Compressible model extension

Though it is not strictly required, confined studies using SCFT typically represent the polymer using a compressible model like (1.28) instead of the incompressible model discussed in Chapters 2 and 3. This is because of numerical difficulties associated with resolving sharp features in the fields near the walls (specifically, in the pressure-like field w_+, the eigenfunction proportional to $w_A + w_B$) [48]. Chantawansri et al. found that the compressible model has a faster rate of convergence, enabling us to obtain equilibrium solutions in less simulation time. The compressible model tends to make similar qualitative predictions to the incompressible one, except that it allows the total density $\phi_A(\mathbf{r})+\phi_B(\mathbf{r})$ to deviate slightly from the system average of 1 everywhere in space. This is a well-controlled approximation of the incompressibility constraint $\phi_A+\phi_B = 1$: in the limit that the Helfand compressibility parameter $(\zeta N)^{-1}$ approaches zero, we exactly recover the incompressible model. In practice, we typically choose a compressibility of 0.001. For this value, we find at equilibrium that the total density at any given point in space is close to 1, so we say that the model is weakly compressible. For example, in a bulk lamellar system at $f = 0.5$ and $\chi N = 25$, we found that the standard deviation in the total density was 0.003. In a simulation of lamellae confined to a three-period channel at $f = 0.5$ and $\chi N = 25$, the standard deviation in the total density was 0.009.

Let us generalize the reduced Hamiltonian H_r to explicitly depend on two density fields ϕ_A and ϕ_B representing the A- and B-species of the diblock copolymer, first for bulk systems, and later for confined ones. We start with the form of H_r in equation (2.9b). In direct analogy to (1.28), we add a Helfand compressibility term to keep the total density roughly constant everywhere in space,

$$\frac{H_{\mathrm{r},\zeta}[\phi_A,\phi_B]}{C} = \frac{\zeta N}{2}\int d\mathbf{r}\left(\phi_A(\mathbf{r}) + \phi_B(\mathbf{r}) - 1\right)^2, \tag{4.1}$$

or, in terms of the zero-average order parameters that tend to appear in H_r,

$$\frac{H_{\mathrm{r},\zeta}[\phi_A,\phi_B]}{C} = \frac{\zeta N}{2}\int d\mathbf{r}\left(\delta\phi_A(\mathbf{r}) + \delta\phi_B(\mathbf{r})\right)^2. \tag{4.2}$$

where $\delta\phi_A \equiv \phi_A - f$ and $\delta\phi_B \equiv \phi_B - (1-f)$. As in SCFT, we will study a weakly compressible model by choosing a compressibility $(\zeta N)^{-1}$ of 0.001.

Next, we would like to generalize all of the other terms in our basis set for H_r from (2.9b) to depend on both $\delta\phi_A$ and $\delta\phi_B$, instead of just $\delta\phi$, which in the incompressible model is equivalent to $\delta\phi_A = -\delta\phi_B$. If we try to do this simply by enumerating all of the possible terms that reduce to H_r under the substitution $\delta\phi_B = -\delta\phi_A$ (valid strictly in the incompressible limit), we will end up with an explosion in the number of terms and associated mapping parameters. This is because a term at order j in $\delta\phi$ could have come from $j+1$ possible terms in a compressible model. For example, at cubic order, we can combine all four of the possible compressible model terms to write one term in the incompressible limit:

$$\begin{aligned} &c_{3AAA}\delta\phi_A(\mathbf{r})^3 + c_{3AAB}\delta\phi_A(\mathbf{r})^2\delta\phi_B(\mathbf{r}) + c_{3ABB}\delta\phi_A(\mathbf{r})\delta\phi_B(\mathbf{r})^2 + c_{3BBB}\delta\phi_B(\mathbf{r})^3 \\ &\qquad = (c_{3AAA} - c_{3AAB} + c_{3ABB} - c_{3BBB})\delta\phi(\mathbf{r})^3 = c_3\delta\phi(\mathbf{r})^3. \quad (4.3) \end{aligned}$$

To reduce the number of terms and coefficients needed for our model, we take advantage of the fact that $\delta\phi_B \approx -\delta\phi_A$ is still approximately true in a weakly compressible model. If the standard deviation in the total density is within 1%, we expect that all of the $j+1$ compressible terms will be mutually equivalent to within about 1% locally, or even less when integrated over the system volume due to cancellation. For the same reason, if we attempt phase field mapping with each of these nearly-redundant terms treated as separate basis functionals, we expect that the linear system to solve would be nearly singular. We therefore arbitrarily choose to keep a set of terms that preserves the symmetry about $f = 0.5$, for example:

$$\begin{aligned}\frac{H_{\mathrm{r,compr}}[\phi_A, \phi_B]}{C} &= \int d\mathbf{r} \biggl\{ - c_2 \delta\phi_A(\mathbf{r})\delta\phi_B(\mathbf{r}) + c_3 \frac{\delta\phi_A(\mathbf{r})^3 - \delta\phi_B(\mathbf{r})^3}{2} \\ &\quad + c_4 \frac{\delta\phi_A(\mathbf{r})^4 + \delta\phi_B(\mathbf{r})^4}{2} + c_5 \frac{|\nabla\phi_A(\mathbf{r})|^2 + |\nabla\phi_B(\mathbf{r})|^2}{2} \\ &\quad - c_6 \int d\mathbf{r}'\, G(\mathbf{r} - \mathbf{r}')\delta\phi_A(\mathbf{r})\delta\phi_B(\mathbf{r}') + \frac{\zeta N}{2}\Bigl(\delta\phi_A(\mathbf{r}) + \delta\phi_B(\mathbf{r})\Bigr)^2 \biggr\}. \end{aligned} \tag{4.4}$$

This expression for H_{r} preserves the symmetry in f, since it is unchanged if we make the replacement $f \to 1 - f$ and switch A and B. Another reasonable choice would be to partition coefficients according to the relative weights of their RPA values (for example, by using reference [33]). With either strategy, we can exclude certain terms that are not present in the RPA, such as

$$\int d\mathbf{r}\, \nabla\phi_A(\mathbf{r}) \cdot \nabla\phi_B(\mathbf{r}), \tag{4.5}$$

because the gradient terms only appear in A–A and B–B correlations, and

$$\int d\mathbf{r} \int d\mathbf{r}'\, G(\mathbf{r} - \mathbf{r}')\delta\phi_A(\mathbf{r})\delta\phi_A(\mathbf{r}), \tag{4.6}$$

because only the A–B correlation diverges in the limit of small wavevectors.

4.1.2 Wall interactions

We now further generalize the compressible phase field model to confined systems using the masking method. The procedure that we wish to apply is essentially identical to the one used in SCFT [11]. We begin by defining a microscopic field ϕ_w representing the wall density. Unlike the polymer density fields, ϕ_w is specified as an input to a simulation. Roughly, the idea is that ϕ_w is 1 where the wall is present, and 0 otherwise. In practice, we also introduce a transition region at the edges of all of the walls, for two reasons: first, on physical grounds, the wall should not be atomistically sharp, and second, the rate of convergence for numerical calculations benefits from fields smooth in as many derivatives as possible.

The masking method gives us the flexibility to design ϕ_w however we wish, effectively imposing arbitrarily complicated boundary conditions on the polymer. We developed a procedure that takes a two-dimensional black-and-white bitmap image in which each pixel corresponds to a block of grid points in a field (we used a block of size 16×16), resizes the image, applies one or more blur filters, scales the result to the range $[0, 1]$, and writes field data to a text file compatible with PolyFTS. During the resizing step, we used MATLAB's algorithm for Lanczos resampling, but only allowed the output to take values of zero or one. We found that this step helped to smooth corners in the image. For the filter, we used a Gaussian blur with a size of 16 pixels and a standard deviation of 3 pixels. Figure 4.1 shows an example of an initial bitmap drawn by hand and the result after resizing and filtering.

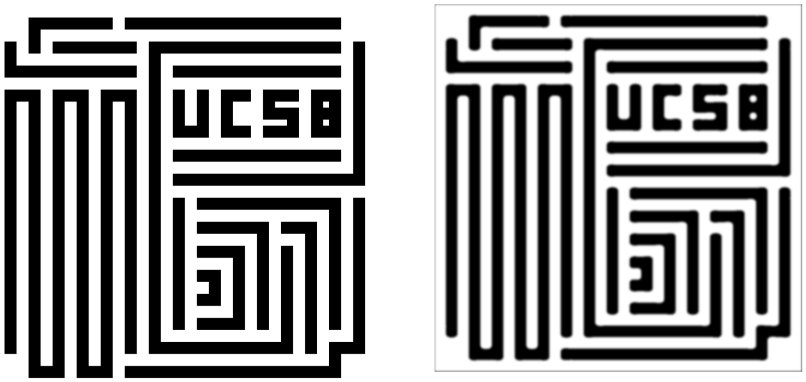

Figure 4.1: Left: a hand-drawn bitmap image depicting a pattern of trenches (black) into which block copolymer will be deposited. Right: the same pattern after applying Lanczos-3 resampling and a Gaussian filter to smooth the wall density field.

The wall should affect the partition function and Hamiltonian in two places, whether the model is real or complex. First, the incompressibility condition (1.8) is modified to read

$$\check{\rho}_A(\mathbf{r}) + \check{\rho}_B(\mathbf{r}) + \rho_0 \phi_w(\mathbf{r}) = \rho_0, \tag{4.7}$$

leading to a different expression for (1.9),

$$\mathcal{K} = \delta[\check{\rho}_A + \check{\rho}_B + \rho_0 \phi_w - \rho_0], \tag{4.8}$$

and a different expression for the replacement of ϕ_B,

$$\phi(\mathbf{r}) = \phi_A(\mathbf{r}) = 1 - \phi_B(\mathbf{r}) - \phi_w(\mathbf{r}). \tag{4.9}$$

In principle, we should be able to trace the effect of this change through to the reduced Hamiltonian H_r to embed the same constraint into a real-valued incompressible model, but we did not find it straightforward to do so, as we will show in Section 4.2.2. We found better success with the compressible model. In SCFT, we simply modify the Helfand compressibility term from (1.10) to account for the wall density,

$$\mathcal{K}_\zeta = e^{-v_0 \zeta/2 \int d\mathbf{r}\, (\check{\rho}_A(\mathbf{r}) + \check{\rho}_B(\mathbf{r}) + \rho_0 \phi_w(\mathbf{r}) - \rho_0)^2}, \tag{4.10}$$

leading to the following expression for the Hamiltonian in place of (1.23),

$$\begin{aligned} \frac{H[w_A, w_B, \phi_A, \phi_B]}{C} &= \chi N \int d\mathbf{r}\, \phi_A(\mathbf{r}) \phi_B(\mathbf{r}) + \frac{\zeta N}{2} \int d\mathbf{r}\, [\phi_A(\mathbf{r}) + \phi_B(\mathbf{r}) + \phi_w(\mathbf{r}) - 1]^2 \\ &\quad - i \int d\mathbf{r}\, [N w_A(\mathbf{r}) \phi_A(\mathbf{r}) - N w_B(\mathbf{r}) \phi_B(\mathbf{r})] - V \ln Q[i w_A, i w_B]. \end{aligned} \tag{4.11}$$

where, as before, $(\zeta N)^{-1}$ is the compressibility and we can see that the expression reduces to the original one in the bulk where $\phi_w = 0$. In the real-valued field theory, we make an analogous change to the compressibility term from (4.1):

$$\frac{H_{\mathrm{r},\zeta}[\phi_A, \phi_B]}{C} = \frac{\zeta N}{2} \int d\mathbf{r} \left(\phi_A(\mathbf{r}) + \phi_B(\mathbf{r}) + \phi_w(\mathbf{r}) - 1 \right)^2 \tag{4.12}$$

or in terms of zero-average fields,

$$\frac{H_{\mathrm{r},\zeta}[\phi_A, \phi_B]}{C} = \frac{\zeta N}{2} \int d\mathbf{r} \left(\delta\phi_A(\mathbf{r}) + \delta\phi_B(\mathbf{r}) + \delta\phi_w(\mathbf{r}) \right)^2 . \tag{4.13}$$

Note that upon introduction of a wall density into the model, we must change the definitions of the zero-average fields to

$$\delta\phi_A(\mathbf{r}) = \phi_A(\mathbf{r}) - f(1 - f_w) \tag{4.14}$$

$$\delta\phi_B(\mathbf{r}) = \phi_B(\mathbf{r}) - (1 - f)(1 - f_w) \tag{4.15}$$

$$\delta\phi_w(\mathbf{r}) = \phi_w(\mathbf{r}) - f_w, \tag{4.16}$$

where $f_w = 1/V \int d\mathbf{r}\, \phi_w(\mathbf{r})$ is the overall fraction of the system volume occupied by the wall.

The second change is the introduction of new enthalpic interaction terms between each polymer species and the walls. Like the first term in H given in equation (4.11), the new terms are overall quadratic in density fields and have prefactors analogous to χN, and they will take the same form in H_r. We therefore label them $\chi_{Aw}N$ and $\chi_{Bw}N$ and write

$$\frac{H_w[\phi_A, \phi_B]}{C} = \chi_{Aw}N \int d\mathbf{r}\, \phi_A(\mathbf{r})\phi_w(\mathbf{r}) + \chi_{Bw}N \int d\mathbf{r}\, \phi_B(\mathbf{r})\phi_w(\mathbf{r}) \tag{4.17}$$

or in terms of zero-average fields,

$$\frac{H_w[\phi_A, \phi_B]}{C} = \chi_{Aw} N \int d\mathbf{r}\, \delta\phi_A(\mathbf{r})\delta\phi_w(\mathbf{r}) + \chi_{Bw} N \int d\mathbf{r}\, \delta\phi_B(\mathbf{r})\delta\phi_w(\mathbf{r}) \tag{4.18}$$

where we have discarded inconsequential terms that contain ϕ_w but are independent of ϕ_A and ϕ_B. In the incompressible limit, we can combine both terms by defining $\chi_w N = \chi_{Aw} N - \chi_{Bw} N$:

$$\frac{H_w[\phi]}{C} = \chi_w N \int d\mathbf{r}\, \delta\phi(\mathbf{r})\delta\phi_w(\mathbf{r}). \tag{4.19}$$

In either the incompressible or compressible model, we can also make use of multiple types of walls, each with their own interaction strengths χ_{A,w_i} and χ_{B,w_i}, in which case we add another pair of terms to H or H_r for each wall type.

4.1.3 Species mass conservation

Our numerical methods use a relaxation dynamics scheme like (1.33), which, unlike diffusive dynamics, does not automatically satisfy conservation of mass for each species. We sometimes found it necessary to explicitly impose this constraint on each species density to prevent the relaxation algorithm from adding or removing A or B from the system. We found three strategies to enforce the constraint.

In the most naive approach, after each relaxation step, we reset the average value of ϕ_A to its known value $f(1 - f_w)$. This can be done by computing $1/V \int d\mathbf{r}\, \delta\phi_A(\mathbf{r})$ and subtracting it from the current value of ϕ_A, or, equivalently, by setting the zero mode of $\widehat{\delta\phi_A}(\mathbf{k})$ to fV). (We can combine this with a related strategy that sets to zero the average value of the force (or the zero mode) before taking a step, but this is not reliable by itself due to the accumulation of floating-point errors, *e.g.*, from discrete Fourier transforms of

ϕ_A.) We apply a similar procedure to reset the average value of ϕ_B. This simple solution works well for the models we have written so far, but it is problematic for the variable transformations we will propose in Section 4.1.4 because after modification, if at any grid point ϕ_A becomes negative or greater than 1, the corresponding value of ψ_A will become complex-valued.

Our second strategy uses the Lagrange multiplier method. We promote H_r to a Lagrangian $\mathcal{L}$,

$$\mathcal{L}(\lambda_A, \lambda_B; [\phi_A, \phi_B]) = H_\mathrm{r}[\phi_A, \phi_B] + \lambda_A \int d\mathbf{r}\, \delta\phi_A(\mathbf{r}) + \lambda_B \int d\mathbf{r}\, \delta\phi_B(\mathbf{r}), \tag{4.20}$$

and we locate equilibrium solutions $(\lambda_A^*, \lambda_B^*, \phi_A^*, \phi_B^*)$ iteratively by gradient descent, minimizing $\mathcal{L}$ with respect to ϕ_A and ϕ_B and maximizing $\mathcal{L}$ with respect to λ_A and λ_B in alternating steps. At equilibrium, the constraint is satisfied, so the Lagrange multiplier terms vanish and $H_\mathrm{r} = \mathcal{L}$. This method is also effective, but because it creates a mixed optimization problem, we can no longer use the conjugate gradient method.

We finally settled on a third strategy. We add to H_r quadratic penalties for deviations of the average species densities from their expected values:

$$\frac{H_{\mathrm{r},K}[\phi_A, \phi_B]}{C} = \frac{K_A V}{2}\left(\frac{1}{V}\int d\mathbf{r}\, \delta\phi_A(\mathbf{r})\right)^2 + \frac{K_B V}{2}\left(\frac{1}{V}\int d\mathbf{r}\, \delta\phi_B(\mathbf{r})\right)^2, \tag{4.21}$$

where we took $K_A = K_B = 1000$. Note that we have been cautious to write the right-hand side as an extensive quantity, since H_r/C is extensive. During numerical relaxation, these terms create a contribution to the force of

$$\frac{1}{C}\frac{\delta H_{\mathrm{r},K}[\phi_A, \phi_B]}{\delta\phi_A(\mathbf{r})} = K_A\left(\frac{1}{V}\int d\mathbf{r}\, \delta\phi_A(\mathbf{r})\right) \tag{4.22}$$

for the relaxation of A, and

$$\frac{1}{C}\frac{\delta H_{\mathrm{r},K}[\phi_A,\phi_B]}{\delta\phi_B(\mathbf{r})} = K_B\left(\frac{1}{V}\int d\mathbf{r}\,\delta\phi_B(\mathbf{r})\right) \tag{4.23}$$

for the relaxation of B. This strategy for conserving mass is compatible with our conjugate gradient solver and the rest of the confinement methods in this chapter. When we relax ϕ_A and ϕ_B to equilibrium, we will find that the constraint is approximately satisfied, so $H_{\mathrm{r},K}$ is close to zero and the overall energy H_r is left unchanged.

4.1.4 Bounded density constraint

Recall from Figure 2.5 and Section 2.3.2 that LB- and OK-type phase field models, optimized or unoptimized, sometimes predict volume fractions below 0 or above 1. This pathological behavior frequently occurs at large χN values in both compressible and incompressible models, especially when the polymer has a high degree of conformational frustration, like in the confined system shown in Figure 4.5. This behavior does not occur in the weak segregation regime where the basis set was derived and where the densities tend to be small in amplitude. To use our OPF model in the intermediate segregation regime, though, we would like to have a way to impose the constraint

$$0 \leq \phi(\mathbf{r}) \leq 1 - \phi_w(\mathbf{r}) \tag{4.24}$$

at all values of $\mathbf{r}$ in the incompressible model. In the compressible model with both density fields explicit, the corresponding constraint should be

$$0 \leq \phi_A(\mathbf{r}) \tag{4.25}$$

$$0 \leq \phi_B(\mathbf{r}) \tag{4.26}$$

at all values of $\mathbf{r}$. In this case, unlike in the incompressible model, we can allow the local volume fractions to exceed 1 slightly, since the Helfand compressibility term will prevent large deviations between $\phi_A + \phi_B + \phi_w$ and 1.

Ideally, equilibrium solutions for the OPF model that already satisfy these bounded density constraints will be unchanged, and previous solutions that violate the constraints will be replaced by solutions that do not. We can think of two strategies to enforce the constraints. One strategy is to introduce new terms into the energy that diverge as the density approach its bounds, such as $\phi \ln \phi$, which diverges as ϕ approaches 0. A second strategy is to replace ϕ with a function of a new variable ψ so that ϕ always satisfies the constraint. Each strategy has potential advantages and disadvantages.

Logarithm terms

Let us consider the first strategy, adding new terms to the energy that diverge as the density approaches its bounds. For the compressible model, we define a new Hamiltonian $H_{\mathrm{r}+}$ that contains two new terms, corresponding to the constraints (4.25) and (4.26) respectively. As discussed in Section 2.5, these terms resemble the mixing entropy from Flory-Huggins theory:

$$\frac{H_{\mathrm{r}+}[\phi_A, \phi_B]}{C} = \frac{H_{\mathrm{r}}[\phi_A, \phi_B]}{C} + \int d\mathbf{r}\, \phi_A(\mathbf{r}) \ln \phi_A(\mathbf{r}) + \int d\mathbf{r}\, \phi_B(\mathbf{r}) \ln \phi_B(\mathbf{r}). \tag{4.27}$$

In the incompressible limit, we replace ϕ_B with $1 - \phi_A - \phi_w$ and find that the resulting terms enforce the constraint (4.24), as expected:

$$\frac{H_{\mathrm{r}+}[\phi]}{C} = \frac{H_{\mathrm{r}}[\phi]}{C} + \int d\mathbf{r}\, \phi(\mathbf{r}) \ln \phi(\mathbf{r}) + \int d\mathbf{r}\, (1 - \phi(\mathbf{r}) - \phi_w(\mathbf{r})) \ln(1 - \phi(\mathbf{r}) - \phi_w(\mathbf{r})). \tag{4.28}$$

In Section 4.1.3, we were able to ensure that new terms added to the Hamiltonian did not directly add an energetic contribution, since they become zero at equilibrium when the mass conservation constraint is satisfied. In contrast, the logarithm terms do not vanish when the density is bounded. In fact, because these terms enter at all orders of ϕ, they will effectively add undesired contributions to the mapped coefficients c_2, c_3 and c_4. To counteract this, we can subtract those contributions by examining the coefficients of a Taylor expansion about $\phi = f$. Alternately, we can set an arbitrarily small coefficient on the logarithm terms, say, 0.001. Note that no matter what the coefficient is, as long as it is finite and positive, the equilibrium density will be strictly bounded.

In principle, $H_{\mathrm{r}+}$ should diverge to infinity as ϕ approaches its physical bounds, thus guaranteeing the constraint for any minimizer, as long as we begin relaxation within those bounds. In practice, however, we found that in any situation where these terms would be useful for constraining ϕ—even in the incompressible case and in the bulk where $\phi_w = 0$—we also encountered difficulties in the numerical relaxation. Any time that ϕ grows towards a boundary, the driving force for relaxation builds up two large contributions that nearly cancel each other out, a growing outward push from the original action $-\frac{\delta H_{\mathrm{r}}[\phi]}{\delta\phi(\mathbf{r})}$ and a growing inward push from whichever logarithm term is close to diverging:

$$-\frac{1}{C}\frac{\delta H_{\mathrm{r}+}[\phi]}{\delta\phi(\mathbf{r})} = -\frac{1}{C}\frac{\delta H_{\mathrm{r}}[\phi]}{\delta\phi(\mathbf{r})} - \ln\phi(\mathbf{r}) + \ln(1-\phi(\mathbf{r})-\phi_w(\mathbf{r})). \tag{4.29}$$

Presumably, as ϕ continues to grow, both contributions to the force will continue to grow in magnitude nearly matched ($\frac{\delta H_{\mathrm{r}}[\phi]}{\delta\phi(\mathbf{r})}$ will be slightly larger in magnitude, so that the net force still tends to decrease) until they exactly balance out at equilibrium. We speculate that, once the density reaches a certain segregation strength, the two contributions become too large to accurately resolve their difference by floating-point subtraction [52].

Variable transformation

We proposed the following variable transformation as an alternative strategy. In the compressible model, we define new fields ψ_A and ψ_B. These transformed fields will be related to the A- and B-species densities according to a new function $\tau(\psi)$:

$$\phi_A(\mathbf{r}) = \tau(\psi_A)(\mathbf{r}) = \frac{\tanh(a\psi_A(\mathbf{r})) + 1}{2} \tag{4.30}$$

$$\phi_B(\mathbf{r}) = \tau(\psi_B)(\mathbf{r}) = \frac{\tanh(a\psi_B(\mathbf{r})) + 1}{2}. \tag{4.31}$$

This transformation guarantees that the volume fractions ϕ_A and ϕ_B will be strictly between 0 and 1 for any real values of ψ_A and ψ_B between $-\infty$ and ∞, since

$$\lim_{\psi\to-\infty} \tau(\psi) = 0 \tag{4.32}$$

$$\tau(0) = 0.5 \tag{4.33}$$

$$\lim_{\psi\to\infty} \tau(\psi) = 1. \tag{4.34}$$

The prefactor a controls the rate of the approach to saturation for extreme values of ψ. To see this, we can write $\tau(\psi)$ in terms of $x = e^{-2a\psi}$, then perform a Taylor expansion for $x \to 0$ ($\psi \to \infty$):

$$\begin{aligned}\tau(\psi) &= \frac{1}{2}\left(\frac{1 - e^{-2a\psi}}{1 + e^{-2a\psi}} + 1\right)\\ &= \frac{1}{2}\left(\frac{1-x}{1+x} + 1\right)\\ &= 1 - \frac{3}{2}x + \frac{3}{2}x^2 + \mathcal{O}(x^3), \quad |x| < 1. \end{aligned} \tag{4.35}$$

For large values of ψ, then, we find that $\phi = \tau$ becomes very close to 1 according to

$$1 - \phi = \frac{3}{2}e^{-2a\psi} \approx 1.5 \times 10^{-0.87a\psi}, \quad \psi \to \infty. \tag{4.36}$$

Similarly, as ψ becomes large and negative, ϕ approaches 0 according to

$$\phi = \frac{3}{2}e^{2a\psi} \approx 1.5 \times 10^{0.87a\psi}, \quad \psi \to -\infty. \tag{4.37}$$

It is worth asking whether typical equilibrium values of ϕ can be accurately represented by floating-point values for ψ. Of course, before we can address that subject, we first require that the floating-point number representation of ϕ is an adequate approximation for the real numbers. This separate issue deserves some scrutiny, since we encountered ϕ values as small as 10^{-14} in converged confined OPF simulations (and as small as 10^{-21} in problematic simulations). For comparison, machine epsilon or `DBL_EPS`, the smallest representable increment above 1.0 in double-precision floating-point arithmetic, has a value of 2×10^{-16}. We expect roundoff errors in force and timestep calculations to accumulate near this precision.

Setting aside the thorny issue of approximating ϕ using floating-point numbers, we now address the more straightforward subject of representing ϕ using ψ. Because $a\psi$ appears in the exponent in equations (4.36) and (4.37), it scales linearly with the exponent for the floating-point representation of ϕ. Thus, ψ can easily resolve extreme values of ϕ without risk of arithmetic underflow or overflow. For example, if $\phi =$ `DBL_EPS` $= 2\times10^{-16}$, then $a\psi = -16$. Even if $\phi =$ `DBL_MIN` $= 2 \times 10^{-308}$, the smallest positive number representable by a normal double-precision floating-point value, then $a\psi = -308$. We therefore are not concerned that the choice of a will impact the equilibrium solution for ϕ.

To use the variable transformation, we substitute expressions (4.30) and (4.31) into H_r and perform numerical relaxation on the transformed fields ψ_A and ψ_B instead of ϕ_A and ϕ_B. For example, a basic gradient descent scheme for ψ_A (replacing equation (1.33)) is

$$\begin{aligned}\frac{\partial}{\partial t}\psi_A(\mathbf{r},t) &= -\frac{\delta H_\mathrm{r}[\tau(\psi_A),\tau(\psi_B)]}{\delta\psi_A(\mathbf{r},t)} \\ &= -\int d\mathbf{r}'\,\frac{\delta H_\mathrm{r}[\phi_A,\phi_B]}{\delta\phi_A(\mathbf{r}',t)}\frac{\delta\tau(\psi_A)(\mathbf{r}',t)}{\delta\psi_A(\mathbf{r},t)} \\ &= -\frac{\delta H_\mathrm{r}[\phi_A,\phi_B]}{\delta\phi_A(\mathbf{r},t)}\frac{a\,\mathrm{sech}^2(a\psi_A(\mathbf{r}))}{2}. \end{aligned} \tag{4.38}$$

To write the second line, we applied the functional chain rule. We then reduced the functional derivative to an ordinary derivative to obtain the final line:

$$\frac{\delta\tau(\psi_A)(\mathbf{r}')}{\delta\psi_A(\mathbf{r})} = \delta(\mathbf{r}-\mathbf{r}')\frac{d\tau(\psi_A)}{d\psi_A} = \delta(\mathbf{r}-\mathbf{r}')\frac{a\,\mathrm{sech}^2(a\psi_A(\mathbf{r}))}{2}. \tag{4.39}$$

We can think of the factor $\frac{d\tau(\psi_A)}{d\psi_A}$ in equation (4.38) as a damping effect that slows relaxation when ψ_A is large in magnitude. Note that if we omit $\frac{d\tau(\psi_A)}{d\psi_A}$ from equation (4.38), it is still a valid relaxation scheme, as it still leads to a stationary point in ψ_A in the limit $t \to \infty$. In fact, we can in principle multiply the relaxation force by any finite and positive definite function of $\mathbf{r}$ without changing its solutions. However, as written, equation (4.38) uses the direction of steepest descent that serves as the starting point for the SIS scheme and for the nonlinear conjugate gradient method.

Note that the inverse of τ,

$$\begin{aligned}\tau^{-1}(\phi) &= \frac{\tanh^{-1}(2\phi-1)}{a} \\ &= \frac{1}{2a}\ln\left(\frac{\phi}{1-\phi}\right), \end{aligned} \tag{4.40}$$

becomes complex-valued if ϕ is less than 0 or greater than 1. This may happen when using the first approach to mass conservation in Section 4.1.3. Instead, we use one of the other strategies, which do not require the inverse transformation during relaxation (we may still employ it for setting initial conditions).

4.2 Results

4.2.1 Bulk compressible model

Before we introduce confinement into the system, we test the numerical properties of the compressible model that we generalized from the incompressible OPF model. Figure 4.2 shows converged equilibrium density fields for various formulations of the compressible model compared to the incompressible OPF model `Zinf`. We see that the compressible model `Z3`, defined by (4.4) with a compressibility $(\zeta N)^{-1} = 10^{-3}$, matches the predictions of the incompressible model in both weak and intermediate segregation and both on and off symmetry in f. For this small compressibility, we confirmed that $\delta\phi_A + \delta\phi_B$ was consistently close to zero. For example, at $f = 0.3$ and $\chi N = 35$, we found that the mean value of $\delta\phi_A + \delta\phi_B$ averaged across all 128 grid points was 1×10^{-12} (zero to within roundoff error) with a standard deviation of 6×10^{-9}, so the Helfand compressibility term $H_{\mathrm{r},\zeta}/C$ has a negligible energetic contribution of 2×10^{-13}. Also shown in Figure 4.2 are density profiles for `Z1`, a similar model with $(\zeta N)^{-1} = 10^{-1}$. Even for this larger compressibility, we still find that the mean and standard deviation of $\delta\phi_A + \delta\phi_B$ are almost as small: -4×10^{-12} and 1×10^{-8}.

We also tested an alternate model, `Z3A`, that assigns all of the weights $\{c_i\}$ purely to combinations of ϕ_A,

$$\frac{H_{\mathrm{r,Z3A}}[\phi_A, \phi_B]}{C} = \int d\mathbf{r}\, \Big\{ c_2 \delta\phi_A(\mathbf{r})^2 + c_3 \delta\phi_A(\mathbf{r})^3 + c_4 \delta\phi_A(\mathbf{r})^4 + c_5 \left|\nabla\phi_A(\mathbf{r})\right|^2 \\ + c_6 \int d\mathbf{r}'\, G(\mathbf{r}-\mathbf{r}')\delta\phi_A(\mathbf{r})\delta\phi_A(\mathbf{r}') + \frac{10^3}{2}\Big(\delta\phi_A(\mathbf{r}) + \delta\phi_B(\mathbf{r})\Big)^2 \Big\}, \quad (4.41)$$

and another, `Z3B`, that similarly assigns the weights purely to combinations of ϕ_B. Both of these produced nearly indistinguishable results from `Z3`, supporting our claim from

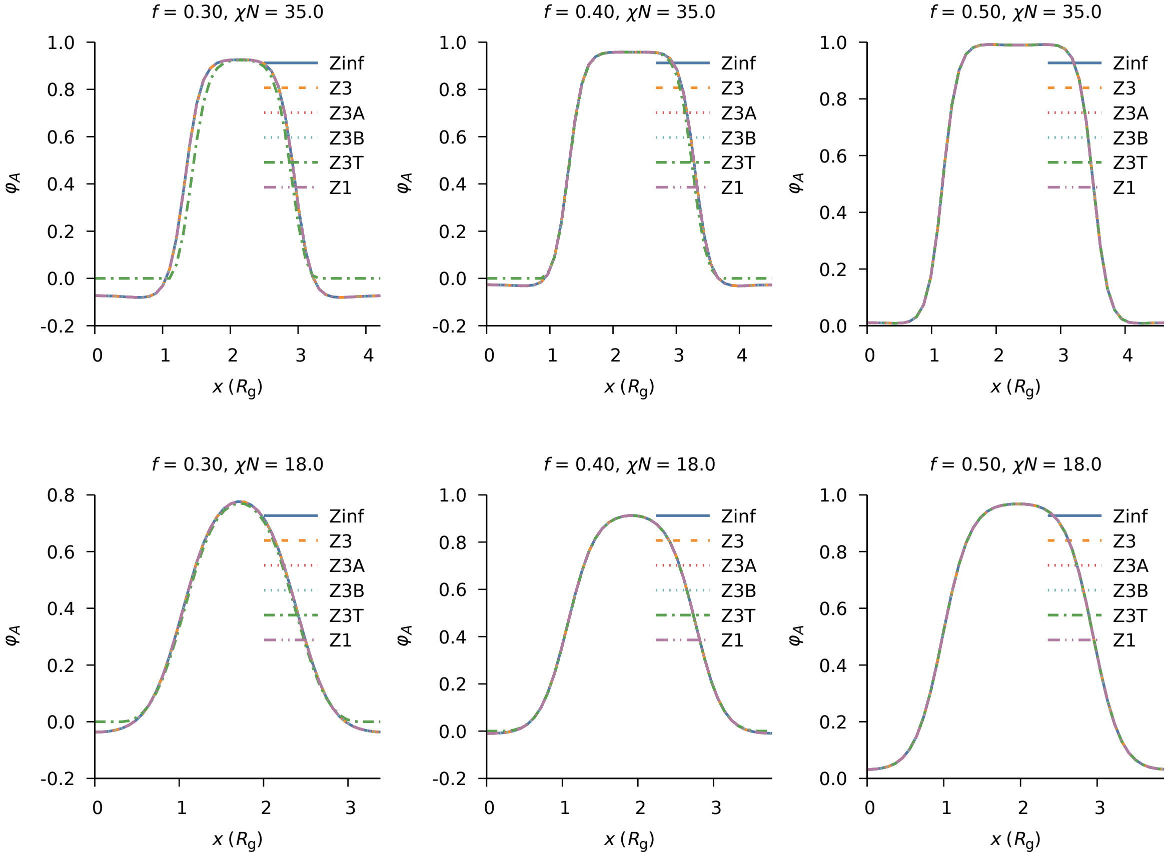

Figure 4.2: Equilibrium density fields $\phi^*(x)$ for various formulations of the OPF model for increasing values of f (left to right) and increasing segregation strengths (bottom to top). `Zinf` is the incompressible model and `Z3` is a compressible model with $\zeta N = 10^3$. The remaining models are variations on `Z3`: `Z1` has $\zeta N = 10^1$; `Z3A` assigns all of the $\{c_i\}$ to combinations of ϕ_A only; `Z3B` assigns the $\{c_i\}$ to combinations of ϕ_B only; and `Z3T` uses the tanh variable transformation to bound densities, and the quadratic penalty strategy to conserve species mass.

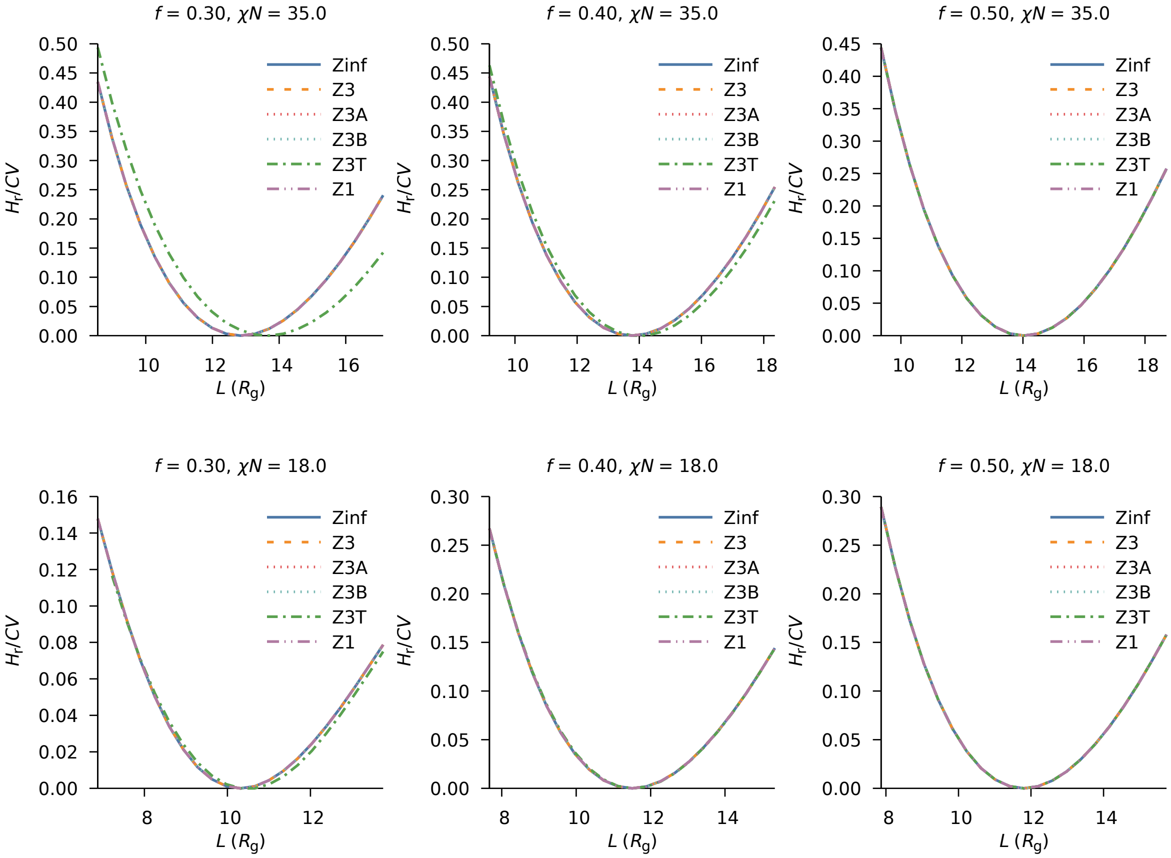

Figure 4.3: Intensive free energy H_{r}/CV of a three-period lamellar state for a diblock copolymer as a function of the simulation cell size L in units of R_{g} for various formulations of the compressible OPF model for increasing values of f (left to right) and increasing segregation strengths (bottom to top). The minimum of each curve occurs at three times the model's predicted domain spacing.

Section 4.1.1 that the compressible terms at a given order are almost mutually equivalent. Additional variants of `Z3A` and `Z3B` that enforce mass conservation for ϕ_A and ϕ_B using the quadratic penalty (4.21) also produced equivalent solutions, though we encountered some numerical issues—we were only able to attain convergence using the fully explicit Euler field updater. We speculate that the issues lies in the handling of the zero Fourier mode of the fields and forces in our implementations of the SIS and conjugate gradient updaters.

We tested a version of the compressible model `Z3T` that uses the tanh variable transformations (4.30) and (4.31) to bound the density and the quadratic penalty (4.21) to conserve mass for each species. We found, as expected, that the density profiles for this model are unchanged as long as the original profile `Z3` stays between the bounds 0 and 1, but as soon as `Z3` steps past these bounds, `Z3T` switches to a new solution. We did not encounter the same numerical issues with `Z3T` as in the previous paragraph, perhaps because the mass conservation constraints are no longer completely determined by the zero Fourier modes of the fields ψ_A and ψ_B.

Next, we tested energy predictions for all of these models using a variable cell calculation like Figure 2.10. Figure 4.3 compares the new results at several combinations of f and χN. As before, we find that `Z3T` yields different results wherever the density is corrected by the bounded constraint, predicting that the stress-free domain spacing L_0 should increase with the severity of the correction. All of the other variations are generally consistent with the incompressible OPF model.

4.2.2 Confined compressible model

We now show some preliminary results investigating the behavior of the new model in confinement. We used SCFT to perform a one-dimensional simulation of a symmetric diblock copolymer melt confined to a channel at $\chi N = 25$, $\zeta N = 1000$ and $\chi_{Aw}N = -10$, corresponding to walls that are slightly selective towards species A. Figure 4.4 shows the stable state with the expected A-wetting at the walls and alternating A and B lamellae in the center of the domain. We also find two metastable states with B wetting at one or both walls. The defect formation energies ΔF for these states are 0.034 k_BT/chain and 0.150 k_BT/chain, computed by taking the difference in H/CV from the stable state. Notice that because the total density is allowed to fluctuate, it rises slightly near the walls, allowing the species densities to decay more gradually into the wall and improving the rate of convergence of the simulation.

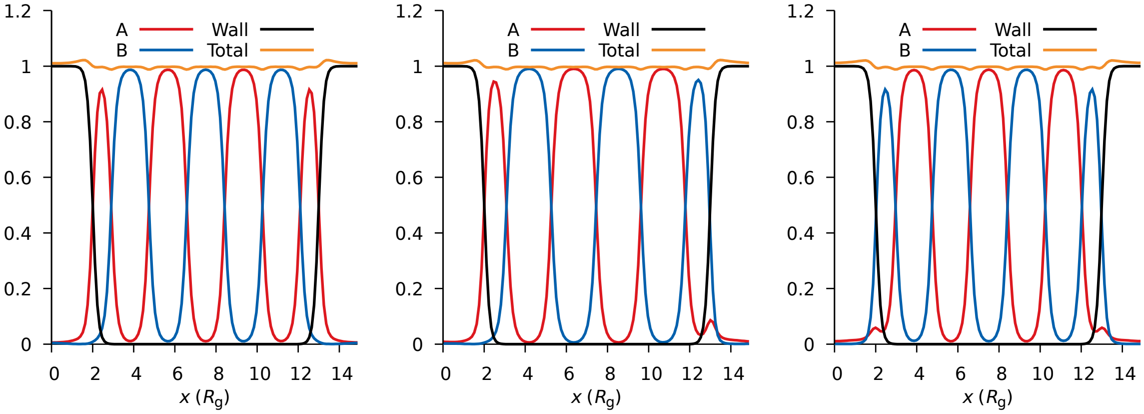

Figure 4.4: Density fields obtained in SCFT for a diblock copolymer at $\chi N = 25$, $f = 0.5$ and $(\zeta N)^{-1} = 0.001$ confined to a channel of width 12 R_g using the masking method. The wall interaction parameter $\chi_w = -10$ favors A-wetting at the walls. Thus, the state with A wetting both walls (left) has the lowest energy and is globally stable. Two metastable states are shown, one with B wetting one wall (center; $\Delta F = 0.034\, k_BT$/chain), and another with B wetting both walls (right; $\Delta F = 0.150\ k_BT$/chain).

Next, we demonstrate the need for the complete set of methods in Section 4.1 by attempting to reproduce Figure 4.4 using a deficient model, shown in Figure 4.5. We use the incompressible OK model from (2.9b) and add only the wall interaction term from (4.19), as was done in reference [53]. Even when seeded from the SCFT solution, the failure of this model is obvious: the densities of both species frequently escape the physical range $[0, 1]$, and the polymer is not excluded from the wall. Note that using a tanh variable transformation would still not be enough to prevent the implicit B-species density from taking on negative values, thereby allowing A to penetrate the walls. This kind of model might instead be appropriate for a chemoepitaxial system in which the polymer is assembled on a flat but chemically patterned surface, and the surface is in contact with, not in, the simulation box.

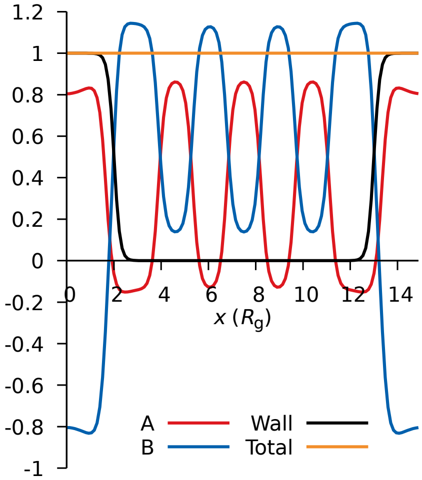

Figure 4.5: Density fields predicted by a standard formulation of the incompressible OK model with only a wall interaction term added for the same confined system as in Figure 4.4.

To contrast this result, Figure 4.6 demonstrates the success of our weakly compressible confined OPF model. We used the variable transformation described in Section 4.1.4 with $a = 0.1$ and the Helfand compressibility term from Section 4.1.1 with $(\zeta N)^{-1} = 0.001$ and reproduced system conditions from the SCFT simulations. The confined OPF solution successfully constrains both densities to $(0, 1)$, thanks to the variable transformation, and correctly predicts that both species densities decay to zero in the walls, thanks to the compressibility term. We also reproduced the metastable defects from Figure 4.4 and computed their defect formation energies as 0.011 $k_BT/$chain and 0.14 $k_BT/$chain. Both values are of the same order of magnitude as predicted by SCFT, but consistent with the trend found in Chapter 3, the OPF model tends to underestimate defect formation energies. Note that the confined OPF model even correctly predicts the small enrichment in the A-density at the edge of a wall with B-wetting. Still, the predicted formation energy for the asymmetric defect is quite poor compared to the 10-20% error expected from Table 3.3. Perhaps the error results from the sharp feature in ϕ_B as it decays into the wall, or from the smaller amplitude of the lamellae in the OPF result relative to SCFT.

At equilibrium, we found that the average species densities for the confined OPF calculation in Figure 4.6 were within 10^{-4} of the desired block fractions $f_A(1 - f_w)$ and $f_B(1 - f_w)$. Consequently, the energy H_r is left practically unchanged by the addition of our constraints from Sections 4.1.1 and 4.1.3. The most extreme value of $\{\psi_i\}$ was -68.5, corresponding to $\phi_B = 1.12 \times 10^{-6}$.

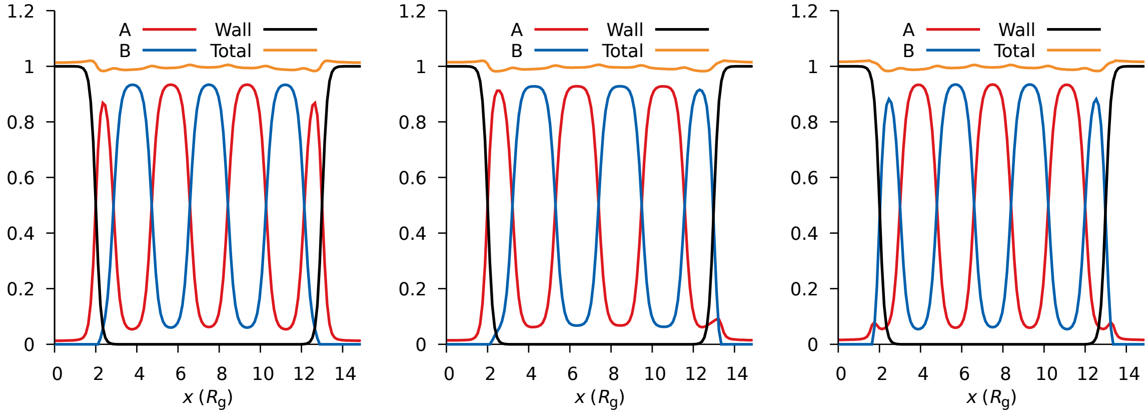

Figure 4.6: Equilibrium density fields ϕ_A and ϕ_B predicted by the weakly compressible confined OPF model with $(\zeta N)^{-1} = 0.001$ for the same confined system as in Figure 4.4. We are able to find the same stable state (left) and the same types of metastable states (center and right) as in SCFT. Defect energies are 0.011 k_BT/chain (center) and 0.14 k_BT/chain (right).

Although the numerical methods we used were sufficient to obtain one-dimensional results like Figure 4.6, we found some other systems challenging. If sharp features are present in the density, like in strong segregation, or when seeding configurations from random noise, we sometimes encountered difficulties in reaching convergence. We have identified at least two possible problems. One is that the conjugate gradient method terminates early because we cannot resolve differences in the energy between two values of the field. Often, though, this occurs when the value of H_{r}/CV seems resolved to a precision of 10^{-5}, or when the L^2 norm of the force is already smaller than 10^{-5}, in which cases we can usually consider the fields fully converged. The second problem is that the relaxation takes a step that causes the energy to diverge.

For example, consider a diblock copolymer melt with $f = 0.3$ and $\chi N = 25$ confined in a cylinder. Our goal is to use a confined OPF model to find the range of cylinder dimensions for which the polymer forms a thinner, unbroken cylinder within its guide pattern. We first approached this problem by seeding an OPF calculation using uniform random initial conditions for ϕ in the range $(0.5, 1)$, which are then converted to initial conditions for ψ by equation (4.40). (We tried using initial conditions for ϕ in the range $(0, 1)$ and found that the simulation diverged in the first 1,000 timesteps.) Figure 4.7 shows the progress of this simulation. After only 1,000 conjugate gradient steps, the polymer already resembles the expected cylindrical configuration. Over the next 12,000 timesteps, the energy H_{r}/CV and the L^2 norm of the force steadily decrease towards convergence. In the density snapshots, we see the texture of the outer cylinder of A continue to smooth out. Then, abruptly, the simulation reports that the energy has diverged. On the other hand, a simulation of the same system but seeded from the converged SCFT density, shown in Figure 4.8, does not diverge and successfully reaches a precision of 10^{-6} k_BT/chain in H_{r}/CV and a force norm of 3×10^{-5}.

Figure 4.9 examines the progress of the conjugate gradient solver for 278 timesteps and line searches leading up to the numerical divergence. We take this opportunity to point out some details about the conjugate gradient method. The conjugate directions

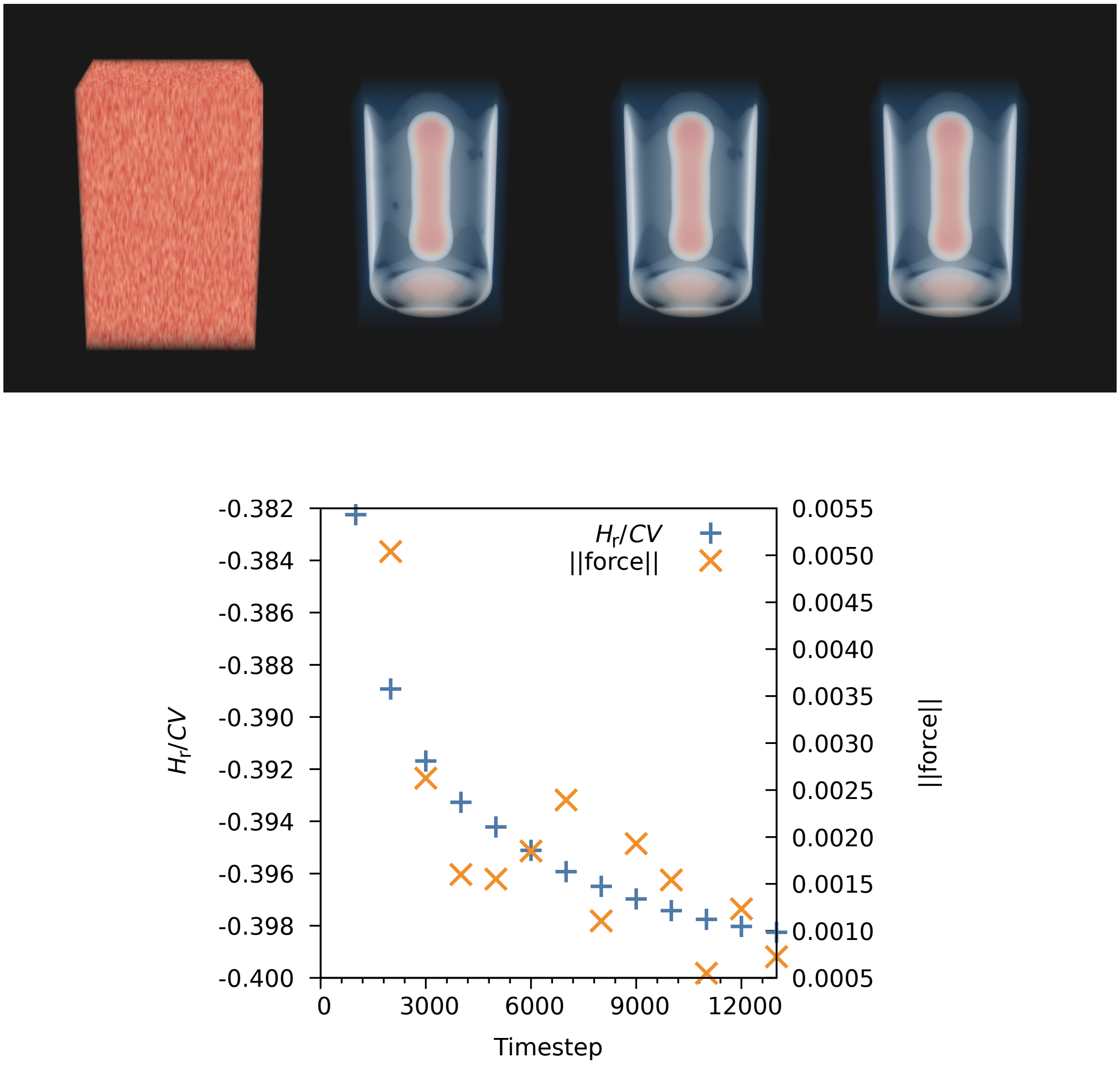

Figure 4.7: Progress of a diblock copolymer melt being relaxed using the OPF model in cylindrical confinement starting from random initial conditions. Top row, left to right: density snapshots from timestep 0, 1,000, 2,000 and 13,000 in the nonlinear conjugate gradient method. Bottom: evolution of the intensive energy H_r/CV and the L^2 norm of the relaxation force over time.

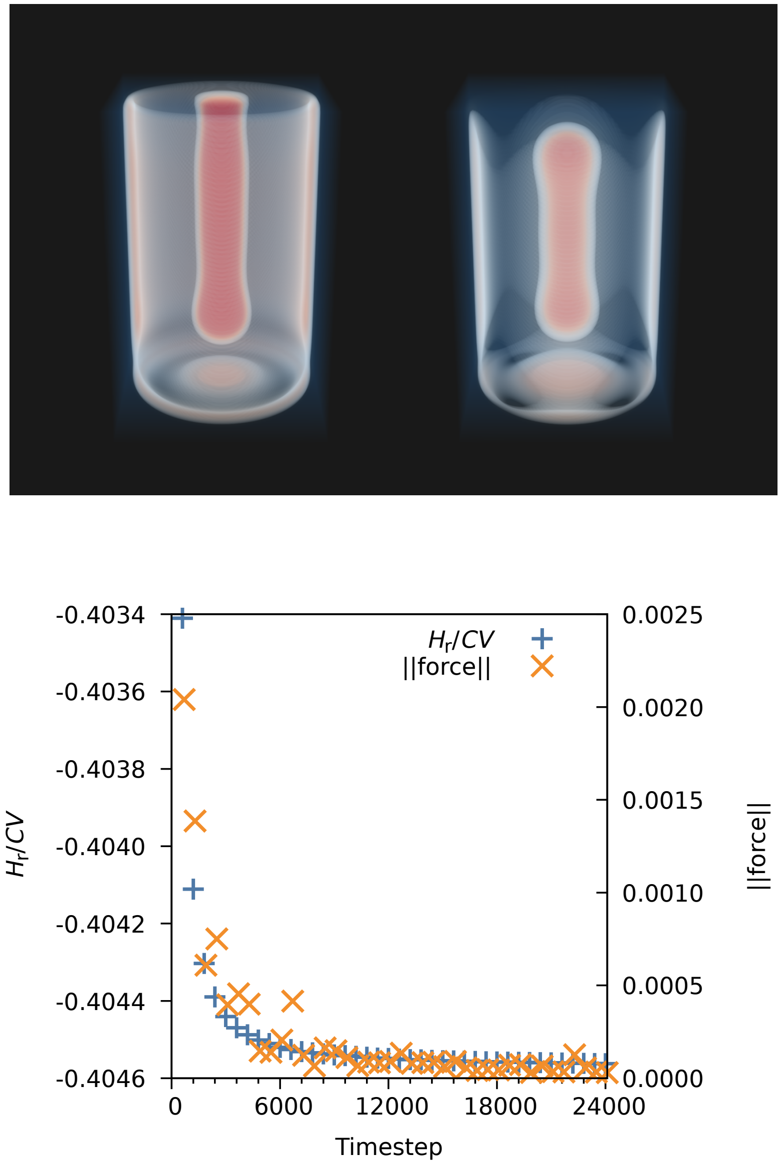

Figure 4.8: Progress of a diblock copolymer melt being relaxed using the OPF model in cylindrical confinement starting from converged SCFT density fields. Top left: equilibrium density for this system, as output by SCFT. Top right: converged density for the confined OPF model. Bottom: evolution of the intensive energy H_r/CV and the L^2 norm of the relaxation force over time.

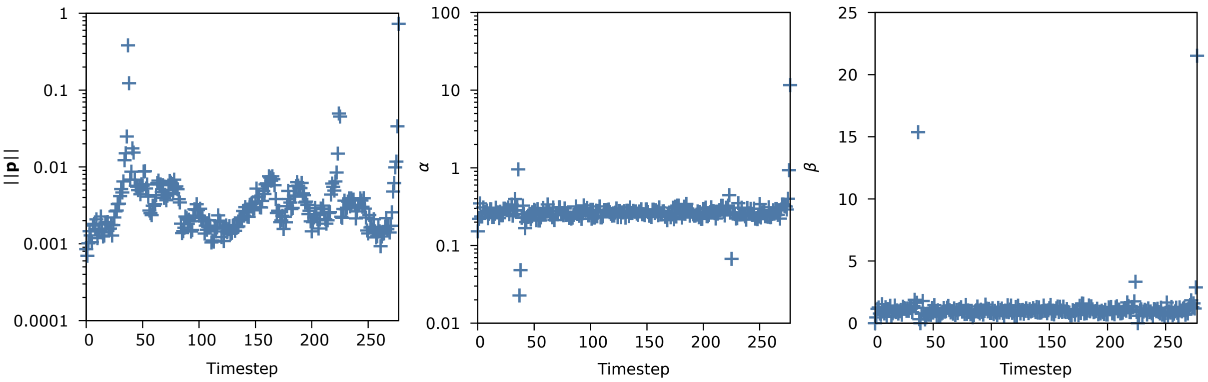

Figure 4.9: Progress of the conjugate gradient method for 278 timesteps (line searches) leading up to an observed numerical divergence. Plotted are the norm of the j-th conjugate direction, $||\mathbf{p}||$ (left), the minimizer of the j-th line search α (center), and the j-th conjugate gradient parameter β (right).

$\mathbf{p}$ are not normalized to one, so their magnitudes vary from step to step. This can be useful for diagnosing issues with the relaxation: if we notice that $||\mathbf{p}||$ does not change as j increases, the relaxation is likely to be "stuck" in one direction. This does not occur here. A possible separate issue, though, is that the final directions grow unusually large in magnitude. Similarly, the values of α (minimizers of each line search) are typically small, but occasionally, the method finds a minimum at an unusually large value of α, and the step before the calculation diverges is one of them. This may be part of the problem, because the first guess for the next value of α (the "blind step" in the next line search) is informed by the previous solution. However, we still encountered this type of issue, even with the blind step limited to a maximum value of 1. Finally, the value of β determines how much "better" the next conjugate direction will be relative to the steepest descent direction (the gradient in $\boldsymbol{\phi}$). We found that it dropped to zero twice during this segment of relaxation, both times in response to a line minimization that did not satisfy the Wolfe conditions after the maximum number of iterations (ten). In these cases, the algorithm then recovers by resetting the history of conjugate directions and starting again from the steepest descent direction. Like $\mathbf{p}$ and α, the final value of

β before divergence is also unusually large, which may give us some insight into how to improve the robustness of our algorithm.

4.2.3 Computational efficiency

The various modifications needed for a confined model—especially the tanh variable transformation—incur new computational costs, so we now revisit our previous analysis of computational efficiency. We compared the performance of the Euler predictor-corrector (EMPEC) method [54], our most efficient method for confined SCFT calculations, and the conjugate gradient solver for the confined OPF model. On the same hardware for both SCFT and the OPF model, we ran serial calculations ensuring that the cost of the simulation was dominated by fast Fourier transform operations [43]. We found that EMPEC field updates for SCFT took 0.40 s, while Polak-Ribière field updates for the confined OPF model took 0.055 s. In confinement, we thus estimate that a field update for the OPF model will complete 7 times faster than a field update for SCFT.

Let us also estimate the number of field updates required to attain convergence in both models. As we stated previously, we expect this number to be strongly dependent on the system and its initial conditions (however, it should not depend on the computer hardware used). To make a fair comparison between the two models, we should adjust our usual criterion for convergence, an arbitrarily small cutoff value for the L^2 norm of the relaxation force. In SCFT, this norm gives us an idea of the precision to which the w fields are known; in the OPF model, the norm of the force measures the precision for the transformed density ψ. A more direct way to compare the two models is to use a cutoff for the intensive energies H/CV and H_r/CV. For the one-dimensional confined channel above, seeded from a sinusoid, we found that SCFT with EMPEC needed 6000 timesteps to compute the energy to a tolerance of 10^{-6}, corresponding to a force norm of 2×10^{-5}, while confined OPF with Polak-Ribière needed only 2000 timesteps to reach the same precision—three times fewer—corresponding to a force norm of only 1×10^{-4}. Overall, then, a confined phase field calculation should complete about 20 times faster than SCFT.

Because we must now store two ψ fields and two ϕ fields, rather than just one field ϕ, as well as some number n_{walls} of ϕ_w fields, a confined OPF model calculation must allocate more memory than a bulk OPF calculation, about $20 + n_{\text{walls}}$. Of course, the corresponding SCFT calculation must also store n_{walls} additional wall fields. Overall, we find that the confined OPF model requires about five times less memory than SCFT, allowing us to access system sizes five times larger.

4.3 Conclusions

In this chapter, we outlined a number of modifications to the standard phase field model formulated in Section 2.1 to account for the physics of confinement (the presence of the wall density in the compressibility and enthalpic interactions with the wall), species conservation of mass, and the physical constraint $0 \leq \phi \leq 1$. Together, we showed that these extensions to the model bring real-valued field theories closer to the accuracy of SCFT and complex-valued field theories. We also demonstrated that, even with the confinement extensions, the OPF model is still significantly faster than SCFT.

Still, there is much left to understand about the confined model, especially in how to maximize its numerical performance at stronger segregation strengths. We speculate that numerical issues associated with floating-point arithmetic may be important [52]. Especially as we go to higher segregation strengths and the density fields approach zero and one, calculations involving ϕ, $\ln \phi$ and ψ increasingly rely on resolving small differences in numbers near zero and one. However, because types like the C++ `double` approximate real numbers using a floating-point representation, numbers close to zero can be represented much more precisely than numbers close to one.

An alternate variable transformation such as $\sqrt{\phi_i}$ as done by reference [33] might have better numerical performance. This transformation constrains $\phi \geq 0$ but not $\phi \leq 1$, which may be sufficient to reproduce the qualitative success of our confined work thus far.

Chapter 5

Conclusions and outlook

In this dissertation, we developed new methods for simulating real-valued polymer field theories with an emphasis on their connections to the more well-established complex field theories. In Chapter 2, we bridged the gap between SCFT and phase field models by introducing and refining phase field mapping, a new procedure inspired by force-matching that quickly and systematically parametrizes an optimized phase field model using output from inexpensive SCFT calculations. In Chapter 3, we studied the numerical properties of our best phase field model thus far, noting especially its impressive numerical efficiency and accurate predictions of length scales. We also identified areas for improvements, such as better performance at asymmetric block fractions and greater transferability across morphologies. Finally, in Chapter 4, we developed a sequence of modifications to the original incompressible model and produced a weakly compressible confined model compatible with the wall masking method that we can directly compare to SCFT in confined systems.

Chapters 2 and 3 teach us that identifying an appropriate set of basis functionals for H_r is crucial for a successful mapping. Without a strong basis set, there will always be inaccuracies in the equilibrium density fields that limit the quality of the mapping. There is room for improvement in our OPF model for the diblock melt, which could not reproduce SCFT density profiles for strongly asymmetric systems even with optimized coefficient values. We find it likely that adding new terms to H_{r} that capture these density profiles will lead to further improvements in other aspects of the model, such as the transferability of the mapping to gyroid, cylindrical and spherical morphologies and phase behavior. A possible lead is to introduce some semilocal or nonlocal character at cubic (and higher) order in ϕ, for example, the Lifshitz entropy, $\int d\mathbf{r}\, \frac{|\nabla\phi|^2}{\phi}$. The Lifshitz entropy might also be valuable for improving the model at strong segregation, since it appears in the ground state dominance approximation. We could also take a data-driven approach and use machine learning to find a functional form for $H_{\mathrm{r}}[\phi]$, as is being explored in electronic structure DFT [55, 56].

We also hope to develop optimized phase field models for other block copolymer architectures and blends. In this area, the generalized Ohta-Kawasaki model [33] (either its "weak segregation" form—effectively the RPA, or its "strong segregation" form) can serve as a starting point for the basis set. Some ideas for systems to study next are: blends of AB diblocks with A and B homopolymers, that could lead to interesting studies of polymer dynamics and reactive blending applications; ABC triblock copolymers, which have a rich phase behavior that reduces to the diblock copolymer in various limits; and bottlebrush copolymers, that might gain the most from a real-valued theory in terms of computational efficiency. As we increase the complexity of the system, the basis set will almost certainly increase in size; it will be interesting to see how the mapping procedure handles these larger basis sets. It may become important to characterize to what extent a mapped model was underfitted (fails to capture all of the relevant physics) or overfitted (loses transferability), perhaps by using the magnitude of Ψ at its minimum, scaled to some reference value. We should also be able to detect redundant basis functionals by looking at the condition number of the matrix used to solve for the coefficients. If the basis set is redundant, the matrix would become degenerate and the condition number would diverge.

Zooming out, a valuable direction for further study is to apply the mapping method in a more general context. Instead of using a single stationary point for the input ϕ^*, we can use multiple states and compute Ψ as a sum over states ϕ_j^*,

$$\begin{aligned}\Psi(\{c_i\}) = \sum_j^{\text{states}} \Bigg(\frac{1}{V} \int d\mathbf{r} \, \left[\left.\frac{\delta H_\mathrm{r}[\phi]}{\delta \phi(\mathbf{r})}\right|_{\phi=\phi_j^*} - \left\langle \frac{\delta H[w_A, w_B, \phi]}{\delta \phi(\mathbf{r})} \right\rangle_{\phi_j^*} \right]^2 \\ + \lambda \left[\left.\frac{\partial H_{\mathrm{r},V}[\phi]}{\partial \epsilon}\right|_{\phi=\phi_j^*} - \left\langle \frac{\partial H_V[w_A, w_B, \phi]}{\partial \epsilon} \right\rangle_{\phi_j^*} \right]^2 \Bigg).\end{aligned} \tag{5.1}$$

A useful set of input states might include different morphologies or defect states to improve transferability. If we choose at least one state with nonzero force or stress, the linear system to solve will no longer be homogeneous, so we can optimize every coefficient in the model simultaneously without resorting to a separate step like equation (2.19) (in place of the elastic modulus, we would hope that the input states provide the information necessary to correctly capture magnitudes for defect energies). We can also choose to relax the partial saddle approximation on H by sampling multiple configurations for w instead of approximating the average forces and stresses using only w^*. Finally, applying the mapping beyond the mean-field approximation would enable us to study an even broader range of phenomena dictated by fluctuation effects, such as phase separation in polyelectrolyte systems, or fluctuation-stabilized microphases like the bicontinuous microemulsion in diblock/homopolymer blends and the bricks-and-mortar phase in miktoarm/homopolymer blends.

Appendix A

Previous phase field models

A.1 Random phase approximation

Leibler's seminal paper [27] describes the random phase approximation for the diblock copolymer melt, a method to asymptotically evaluate the integrals in equation (2.1). Assuming that the potential fields $w_A(\mathbf{r})$ and $w_B(\mathbf{r})$ are close to the values they would take in the homogeneous (disordered) state, Leibler obtains the following expansion for H_{r} in powers of ϕ:

$$\begin{aligned} \frac{H_{\mathrm{r,RPA}}[\phi]}{C} &= H_0 + \sum_{n=2}^{\infty} \frac{1}{n!V^{n-1}} \int d\mathbf{r}_1 \ldots \int d\mathbf{r}_n \, N\Gamma_n(\mathbf{r}_1, \ldots, \mathbf{r}_n)\delta\phi(\mathbf{r}_1) \ldots \delta\phi(\mathbf{r}_n) && \text{(A.1)} \\ &= H_0 + \sum_{n=2}^{\infty} \frac{1}{n!V^{n}} \sum_{\mathbf{k}_1} \ldots \sum_{\mathbf{k}_n} N\hat{\Gamma}_n(\mathbf{k}_1, \ldots, \mathbf{k}_n)\widehat{\delta\phi}(\mathbf{k}_1) \ldots \widehat{\delta\phi}(\mathbf{k}_n), && \text{(A.2)} \end{aligned}$$

where the n-th order vertex function Γ_n is a function of n different positions $\mathbf{r}_1$ through $\mathbf{r}_n$ (or similar in Fourier space). The expression is typically truncated at fourth order, the lowest order sufficient to predict (micro)phase separation, and often a local approximation is applied to the third- and fourth-order vertex functions, producing

$$\begin{aligned}\frac{H_{\mathrm{r,RPA}}[\phi]}{C} &= \frac{1}{2!V}\int d\mathbf{r}\int d\mathbf{r}'\, N\Gamma_2(\mathbf{r}-\mathbf{r}')\delta\phi(\mathbf{r})\delta\phi(\mathbf{r}') \\ &\quad + \frac{1}{3!V^2}\int d\mathbf{r}\, N\Gamma_3\delta\phi(\mathbf{r})^3 + \frac{1}{4!V^3}\int d\mathbf{r}\, N\Gamma_4(0,0)\delta\phi(\mathbf{r})^4. \quad \text{(A.3)}\end{aligned}$$

The expression for Γ_2 can be related to the structure factor $\tilde{S}(\mathbf{k})$, which is the Fourier transform of the density correlation function $\langle\delta\phi(\mathbf{r})\delta\phi(\mathbf{r}')\rangle$:

$$N\hat{\Gamma}_2(\mathbf{k}) = N/\tilde{S}(\mathbf{k}) = \frac{g(1,x)}{g(f,x)g(1-f,x) - \frac{1}{4}[g(1,x)-g(f,x)-g(1-f,x)]^2} - 2\chi N, \tag{A.4}$$

where $x = k^2 = |\mathbf{k}|^2$ has units of R_{g}^{-2}, and the Debye function for the diblock copolymer melt is

$$g(f,x) = \frac{2(fx + e^{-fx} - 1)}{x^2}. \tag{A.5}$$

For the interested reader, derivations of the RPA can be found in the appendix of [27], and in [33, 41], and [57].

A.2 Ohta-Kawasaki model

In 1986, Ohta and Kawasaki simplified the random phase approximation to obtain a more tractable expression for analytical and numerical calculations. They noticed that the vertex function $\hat{\Gamma}_2(\mathbf{k})$ diverges as k goes to zero and infinity, and preserved the behavior of the function in those limits:

$$\lim_{k\to 0}\frac{N\hat{\Gamma}_2(\mathbf{k})}{k^{-2}} = \frac{3}{4f^2(1-f)^2} \tag{A.6}$$

$$\lim_{k\to\infty}\frac{N\hat{\Gamma}_2(\mathbf{k})}{k^2} = \frac{1}{4f(1-f)}. \tag{A.7}$$

Then, they added a constant in k to capture the χ-dependence and preserve the spinodal (the height of the minimum). This leads to the approximation

$$\frac{1}{2}N\hat{\Gamma}_2(\mathbf{k}) \approx -\chi N + \frac{s(f)}{4f^2(1-f)^2} + \frac{1}{4f(1-f)}k^2 + \frac{3}{4f^2(1-f)^2}k^{-2}. \tag{A.8}$$

where $s(f)$ is a fitting function that we will address later. This corresponds directly to the three quadratic terms in equation (2.9b):

$$\begin{aligned}\frac{1}{2!V}\int d\mathbf{r}\int d\mathbf{r}'\, N\Gamma_2(\mathbf{r}-\mathbf{r}')\delta\phi(\mathbf{r})\delta\phi(\mathbf{r}')& \\ \approx \int d\mathbf{r}\left\{c_2\delta\phi(\mathbf{r})^2 + c_5\left|\nabla\phi(\mathbf{r})\right|^2 + c_6\int d\mathbf{r}'\, G(\mathbf{r}-\mathbf{r}')\delta\phi(\mathbf{r})\delta\phi(\mathbf{r}')\right\}&, \end{aligned} \tag{A.9}$$

where

$$c_{2,\mathrm{OK}} = -\chi N + \frac{s(f)}{4f^2(1-f)^2} \tag{A.10}$$

$$c_{5,\mathrm{OK}} = \frac{1}{4f(1-f)} \tag{A.11}$$

$$c_{6,\mathrm{OK}} = \frac{3}{4f^2(1-f)^2}. \tag{A.12}$$

Note that in their original paper, Ohta and Kawasaki eventually divide their entire energy functional by $2c_{5,\mathrm{OK}}$ for convenience. We have been careful here to retain the original multiplicative factor on all of the terms (a straightforward way to do this is to ensure that c_2 contains the term $-\chi N$). Also note that c_2 has units of k_BT per chain, while c_5 has units of $k_BT \cdot R_\mathrm{g}^2$ per chain, and c_6 has units of $k_BT \cdot R_\mathrm{g}^{-2}$ per chain to compensate for factors of k^2 in equation (A.8) (or ∇^2 and $G(\mathbf{r}-\mathbf{r}')$ in equation (A.9)).

The fitting function $s(f)$ is defined to approximately preserve the spinodal χN_s, the value of χN at which our approximant for $\tilde{S}$ first diverges (and $\hat{\Gamma}_2$ first reaches zero). Since we can compute the RPA value of χN_s numerically, we will not bother with $s(f)$

and instead exactly preserve the spinodal using

$$\begin{aligned} c_{2,\mathrm{OK}} &= \frac{1}{2}N\hat{\Gamma}(k^*) - c_5 k^{*2} - c_6 k^{*-2} \\ &= -\chi N + \chi N_s - c_5 k^{*2} - c_6 k^{*-2}, \end{aligned} \tag{A.13}$$

where the critical wavevector k^* is the location of the minimum of $\hat{\Gamma}_2$, given in equation (2.12b).

To complete equation (2.9b), Ohta and Kawasaki make a local approximation for the third- and fourth-order vertex functions. The cubic and quartic polynomial coefficients c_3 and c_4 are not specified—the authors only note that in the strong segregation limit, the polynomial in $\delta\phi$ must have two degenerate minima corresponding to the densities in the A-rich and B-rich phases. Other authors have assumed phenomenological values that produce the desired minima for the double well in H_r, like in equation (2.10) and Figure 2.1 [53, 58], or values corresponding to $N\Gamma_3$ and $N\Gamma_4(0,0)$ from the previous section. To represent the OK model as fairly as possible in comparisons to our model, we parametrize c_3 and c_4 using phase field mapping, while retaining (A.13), (A.11) and (A.12) for the remaining quadratic coefficients.

A.3 Stress derivation

We perform an example derivation of the stress for the Ohta-Kawasaki form of H_r. For reference, the starting point is an intensive version of equation (2.9b),

$$\begin{aligned} \frac{H_{\mathrm{r},V}[\phi]}{C} = \frac{1}{V}\int d\mathbf{r}\,\Big\{ & c_2\delta\phi(\mathbf{r})^2 + c_3\delta\phi(\mathbf{r})^3 + c_4\delta\phi(\mathbf{r})^4 + c_5\left|\nabla\phi(\mathbf{r})\right|^2 \\ & + c_6\int d\mathbf{r}'\,G(\mathbf{r}-\mathbf{r}')\delta\phi(\mathbf{r})\delta\phi(\mathbf{r}')\Big\}, \end{aligned} \tag{A.14}$$

where the Green's function $G(\mathbf{r}-\mathbf{r}')$ solves Laplace's equation: $-\nabla^2 G(\mathbf{r}-\mathbf{r}') = \delta(\mathbf{r}-\mathbf{r}')$. In one dimension, we simplify to

$$\frac{H_{\mathrm{r},V}[\phi]}{C} = \frac{1}{L}\int_0^L dr \left\{ c_2\delta\phi(r)^2 + c_3\delta\phi(r)^3 + c_4\delta\phi(r)^4 + c_5\left|\frac{d\phi(r)}{dr}\right|^2 \right. \\ \left. + c_6\int_0^L dr'\, G(r-r')\delta\phi(r)\delta\phi(r') \right\}, \quad (A.15)$$

where, for periodic boundary conditions in one dimension, the Green's function G has dimensions of length and becomes $G(r-r') = -|r-r'|$.

To compute the stress, the derivative of $H_{\mathrm{r},V}$ with respect to the strain $\epsilon = \frac{L-L_0}{L_0}$, we first make explicit the dependence on L by moving it out of integration bounds, derivatives, and G. Defining a new spatial variable $x = r/L$ and new L-independent functions $\delta\varphi(x) = \delta\phi(r)$ and $G_x(x-x') = G(r-r')/L$, we write

$$\frac{H_{\mathrm{r},V}[\phi]}{C} = \frac{1}{L}\int_0^1 L\,dx \left\{ c_2\delta\varphi(x)^2 + c_3\delta\varphi(x)^3 + c_4\delta\varphi(x)^4 + \frac{c_5}{L^2}\left|\frac{d\varphi(x)}{dx}\right|^2 \right. \\ \left. + c_6\int_0^1 L\,dx'\, LG_x(x-x')\delta\varphi(x)\delta\varphi(x') \right\}. \quad (A.16)$$

We then take the derivative with respect to L and find that the Landau polynomial terms vanish:

$$\frac{1}{C}\frac{\partial H_{\mathrm{r},V}[\phi]}{\partial L} = \int_0^1 dx \left\{ \frac{-2c_5}{L^3}\left|\frac{d\varphi(x)}{dx}\right|^2 + 2c_6 L\int_0^1 dx'\, G_x(x-x')\delta\varphi(x)\delta\varphi(x') \right\}. \quad (A.17)$$

Restoring the original variable r, the stress is then

$$\begin{aligned}\frac{1}{C}\frac{\partial H_{\mathrm{r},V}[\phi]}{\partial \epsilon} &= \frac{1}{C}\frac{\partial H_{\mathrm{r},V}[\phi]}{\partial L}\frac{dL}{d\epsilon} \\ &= \frac{1}{C}\frac{\partial H_{\mathrm{r},V}[\phi]}{\partial L}L_0 \\ &= \frac{L_0}{L^2}\int_0^L dr\left\{-2c_5\left|\frac{d\phi(r)}{dr}\right|^2 + 2c_6\int_0^L dr'\, G(r-r')\delta\phi(r)\delta\phi(r')\right\}. \qquad (A.18)\end{aligned}$$

In d dimensions, the procedure is similar, but we can choose to define stress and strain tensors to describe changes for every element of the cell shape tensor. The expression for the Green's function and the dimensions of the Green's function will also change, but we can still define a system size-independent version, and the extra factors of length from integration over $d\mathbf{r}'$ will always cancel out the changes to the dimensions of G. If the strain is isotropic, we can again use a scalar ϵ. Repeating the derivation, we find a generalization of (A.18),

$$\frac{1}{C}\frac{\partial H_{\mathrm{r},V}[\phi]}{\partial \epsilon} = \frac{1}{(\epsilon+1)V}\int d\mathbf{r}\left\{-2c_5\left|\nabla\phi(\mathbf{r})\right|^2 + 2c_6\int d\mathbf{r}'\, G(\mathbf{r}-\mathbf{r}')\delta\phi(\mathbf{r})\delta\phi(\mathbf{r}')\right\}. \qquad (A.19)$$

Bibliography

[1] M. W. Matsen and M. Schick, "Stable and unstable phases of a diblock copolymer melt," *Physical Review Letters*, vol. 72, no. 16, pp. 2660–2663, 1994. 1

[2] C. A. Tyler and D. C. Morse, "Orthorhombic Fddd network in triblock and diblock copolymer melts," *Physical Review Letters*, 2005. 1

[3] G. H. Fredrickson, *The Equilibrium Theory of Inhomogeneous Polymers.* Oxford University Press, 2006. 1, 1.1, 2.5, 4

[4] M. W. Matsen, "Effect of architecture on the phase behavior of AB-type block copolymer melts," *Macromolecules*, 2012. 1

[5] Z. Mester, N. A. Lynd, K. T. Delaney, and G. H. Fredrickson, "Phase coexistence calculations of reversibly bonded block copolymers: A unit cell Gibbs ensemble approach," *Macromolecules*, vol. 47, no. 5, pp. 1865–1874, 2014. 1

[6] W. Li, K. T. Delaney, and G. H. Fredrickson, "Fddd network phase in ABA triblock copolymer melts," *Journal of Polymer Science, Part B: Polymer Physics*, 2016. 1

[7] C. L. Tsai, K. T. Delaney, and G. H. Fredrickson, "Genetic Algorithm for Discovery of Globally Stable Phases in Block Copolymers," *Macromolecules*, 2016. 1

[8] S. P. Paradiso, K. T. Delaney, and G. H. Fredrickson, "Swarm Intelligence Platform for Multiblock Polymer Inverse Formulation Design," *ACS Macro Letters*, 2016. 1

[9] M. Khadilkar, S. Paradiso, K. Delaney, and G. Fredrickson, "Inverse Design of Bulk Morphologies in Multiblock Polymers Using Particle Swarm Optimization," *Macromolecules*, 2017. 1

[10] J. M. Martin, W. Li, K. T. Delaney, and G. H. Fredrickson, "SCFT Study of Diblock Copolymer Melts in Electric Fields: Selective Stabilization of Orthorhombic Fddd Network Phase," *Macromolecules*, 2018. 1

[11] A. W. Bosse, C. J. García-Cervera, and G. H. Fredrickson, "Microdomain ordering in laterally confined block copolymer thin films," *Macromolecules*, vol. 40, pp. 9570–9581, dec 2007. 1, 4, 4.1.2

[12] C. Tang, E. M. Lennon, G. H. Fredrickson, E. J. Kramer, and C. J. Hawker, "Evolution of block copolymer lithography to highly ordered square arrays," *Science*, 2008. 1, 4

[13] S. M. Hur, C. J. García-Cervera, E. J. Kramer, and G. H. Fredrickson, "SCFT simulations of thin film blends of block copolymer and homopolymer laterally confined in a square well," *Macromolecules*, vol. 42, no. 15, pp. 5861–5872, 2009. 1, 4

[14] H. Takahashi, N. Laachi, K. T. Delaney, S. M. Hur, C. J. Weinheimer, D. Shykind, and G. H. Fredrickson, "Defectivity in laterally confined lamella-forming diblock copolymers: Thermodynamic and kinetic aspects," *Macromolecules*, vol. 45, no. 15, pp. 6253–6265, 2012. 1, 3.2.6, 3.2.6, 4

[15] B. Kim, N. Laachi, K. T. Delaney, M. Carilli, E. J. Kramer, and G. H. Fredrickson, "Thermodynamic and kinetic aspects of defectivity in directed self-assembly of cylinder-forming diblock copolymers in laterally confining thin channels," *Journal of Applied Polymer Science*, 2014. 1, 3.2.6, 4

[16] N. Laachi, T. Iwama, K. T. Delaney, D. Shykind, C. J. Weinheimer, and G. H. Fredrickson, "Directed self-assembly of linear arrays of block copolymer cylinders," *Journal of Polymer Science, Part B: Polymer Physics*, vol. 53, no. 5, pp. 317–326, 2015. 1, 3.2.6, 4

[17] G. Ouaknin, N. Laachi, D. Bochkov, K. Delaney, G. H. Fredrickson, and F. Gibou, "Functional level-set derivative for a polymer self consistent field theory Hamiltonian," *Journal of Computational Physics*, 2017. 1, 4

[18] C. L. Carpenter, S. Nicaise, P. L. Theofanis, D. Shykind, K. K. Berggren, K. T. Delaney, and G. H. Fredrickson, "Orientational Preference in Multilayer Block Copolymer Nanomeshes with Respect to Layer-to-Layer Commensurability," *Macromolecules*, 2017. 1, 4

[19] F. Drolet and G. H. Fredrickson, "Optimizing chain bridging in complex block copolymers," *Macromolecules*, 2001. 1

[20] N. A. Lynd, F. T. Oyerokun, D. L. O'Donoghue, D. L. Handlin, and G. H. Fredrickson, "Design of soft and strong thermoplastic elastomers based on nonlinear block copolymer architectures using self-consistent-field theory," *Macromolecules*, 2010. 1

[21] J. G. E. M. Fraaije, "Dynamic density functional theory for microphase separation kinetics of block copolymer melts," *The Journal of Chemical Physics*, vol. 99, no. 11, p. 9202, 1993. 1

[22] S. P. Paradiso, K. T. Delaney, C. J. García-Cervera, H. D. Ceniceros, and G. H. Fredrickson, "Block copolymer self assembly during rapid solvent evaporation: Insights into cylinder growth and stability," *ACS Macro Letters*, vol. 3, no. 1, pp. 16–20, 2014. 1

[23] G. H. Fredrickson, V. Ganesan, and F. Drolet, "Field-theoretic computer simulation methods for polymers and complex fluids," *Macromolecules*, vol. 35, no. 1, pp. 16–39, 2002. 1

[24] J. Liu, K. T. Delaney, and G. H. Fredrickson, "Optimized phase field models in confinement: fast and accurate simulations of directed self-assembly," *Proceedings of the SPIE - Advances in Patterning materials and Processes XXXIV*, vol. 10146, p. 101460Z, 2017. 1, 3.2.6

[25] G. H. Fredrickson and E. Helfand, "Fluctuation effects in the theory of microphase separation in block copolymers," *The Journal of Chemical Physics*, vol. 87, no. 1, p. 697, 1987. 1, 2.2

[26] T. Ohta and K. Kawasaki, "Equilibrium morphology of block copolymer melts," *Macromolecules*, vol. 19, no. 10, pp. 2621–2632, 1986. 1, 2.2

[27] L. Leibler, "Theory of microphase separation in block copolymers," *Macromolecules*, vol. 13, no. 6, pp. 1602–1617, 1980. 1, 2.2, 2.5, A.1, A.1

[28] S. Izvekov and G. A. Voth, "A multiscale coarse-graining method for biomolecular systems," *Journal of Physical Chemistry B*, vol. 109, no. 7, pp. 2469–2473, 2005. 1

[29] M. C. Villet and G. H. Fredrickson, "Numerical coarse-graining of fluid field theories," *Journal of Chemical Physics*, vol. 132, no. 3, 2010. 1

[30] H. D. Ceniceros and G. H. Fredrickson, "Numerical Solution of Polymer Self-Consistent Field Theory," *Multiscale Modeling & Simulation*, vol. 2, pp. 452–474, jan 2004. 1.1.2, 1.2

[31] N. Schuch and F. Verstraete, "Computational complexity of interacting electrons and fundamental limitations of density functionaltheory," *Nature Physics*, 2009. 2.1

[32] M. Kac, "On the partition function of a one-dimensional gas," *Physics of Fluids*, 1959. 2.1

[33] T. Uneyama and M. Doi, "Density functional theory for block copolymer melts and blends," *Macromolecules*, vol. 38, pp. 196–205, jan 2005. 2.2, 2.3.2, 2.5, 4.1.1, 4.3, 5, A.1

[34] P. C. Hohenberg and A. P. Krekhov, "An introduction to the Ginzburg-Landau theory of phase transitions and nonequilibrium patterns," *Physics Reports*, vol. 572, pp. 1–42, 2015. 2.2

[35] J. Liu, N. Laachi, K. T. Delaney, and G. H. Fredrickson, "Advantages and limitations of density functional theory in block copolymer directed self-assembly," *Proceedings of the SPIE - Alternative Lithographic Technologies VII*, vol. 9423, p. 94231I, mar 2015. 2.3.1

[36] Y. Bohbot-Raviv and Z. G. Wang, "Discovering new ordered phases of block copolymers," *Physical review letters*, vol. 85, no. 16, pp. 3428–31, 2000. 2.3.2, 2.5

[37] M. W. Matsen and F. S. Bates, "Unifying weak- and strong-segregation block copolymer theories," *Macromolecules*, vol. 29, no. 4, pp. 1091–1098, 1996. 2.3.2, 3.2.4

[38] J. Liu, K. T. Delaney, and G. H. Fredrickson, "Phase field mapping for accurate, ultrafast simulations of directed self-assembly," *Proceedings of the SPIE - Alternative Lithographic Technologies VIII*, vol. 9779, p. 977920, 2016. 2.4.1, 3.2.6

[39] H. Tang and K. F. Freed, "Free energy functional expansion for inhomogeneous polymer blends," *The Journal of Chemical Physics*, vol. 94, no. 2, pp. 1572–1583, 1991. 2.5

[40] T. Ohta and K. Kawasaki, "Comment on the free energy functional of block copolymer melts in the strong segregation limit," *Macromolecules*, vol. 23, pp. 2413–2414, apr 1990. 2.5

[41] W. E. McMullen, "A fourth-order, density-functional, random-phase approximation study of monomer segregation in phase-separated, lamellar, diblock-copolymer melts," *Macromolecules*, vol. 26, no. 5, pp. 1027–1036, 1993. 2.5, A.1

[42] J. Nocedal and S. J. Wright, *Numerical Optimization*. Springer, 2006. 3.1.1, 3.1.1

[43] K. T. Delaney and G. H. Fredrickson, "Polymer field-theory simulations on graphics processing units," *Computer Physics Communications*, vol. 184, no. 9, pp. 2102–2110, 2013. 3.1.1, 3.2.1, 4.2.3

[44] T. P. T. Russell, R. P. Hjelm, P. A. P. Seeger, R. H. Jr, and P. A. P. Seeger, "Temperature dependence of the interaction parameter of polystyrene and poly (methyl methacrylate)," *Macromolecules*, vol. 23, pp. 890–893, 1990. 3.2.5, 3.2.5

[45] X. Cheng, L. Lin, W. E, P. Zhang, and A.-C. Shi, "Nucleation of ordered phases in block copolymers," *Physical Review Letters*, vol. 104, no. 14, pp. 1–4, 2010. 3.2.6

[46] T. Iwama, N. Laachi, B. Kim, M. Carilli, K. T. Delaney, and G. H. Fredrickson, "Computational study of directed self-assembly in neutral prepatterns for a graphoepitaxial pitch-multiplication application," *Macromolecules*, vol. 48, no. 4, pp. 1256–1261, 2015. 3.2.6, 4

[47] W. E, W. Ren, and E. Vanden-Eijnden, "String method for the study of rare events," *Physical Review B*, pp. 5–8, 2002. 3.2.6

[48] T. L. Chantawansri, S.-M. Hur, C. J. García-Cervera, H. D. Ceniceros, and G. H. Fredrickson, "Spectral collocation methods for polymer brushes.," *The Journal of chemical physics*, vol. 134, no. 24, p. 244905, 2011. 4, 4.1.1

[49] F. S. Bates, M. A. Hillmyer, T. P. Lodge, C. M. Bates, K. T. Delaney, and G. H. Fredrickson, "Multiblock polymers: Panacea or Pandora's box?," *Science*, vol. 336, no. 6080, pp. 434–440, 2012. 4

[50] M. W. Matsen, "The standard Gaussian model for block copolymer melts," *Journal of Physics: Condensed Matter*, vol. 14, no. 2, pp. R21–R47, 2002. 4

[51] M. W. Matsen, "Thin films of block copolymer," *Journal of Chemical Physics*, vol. 106, no. 18, pp. 7781–7791, 1997. 4

[52] D. Goldberg, "What every computer scientist should know about floating-point arithmetic," *ACM Computing Surveys*, vol. 23, no. 1, pp. 5–48, 1991. 4.1.4, 4.3

[53] K. Yoshimoto and T. Taniguchi, "Large-Scale Simulations of Directed Self-Assembly with Simplified Model," *Journal of Photopolymer Science and Technology*, vol. 26, no. 6, pp. 809–816, 2013. 4.2.2, A.2

[54] D. Düchs, K. T. Delaney, and G. H. Fredrickson, "A multi-species exchange model for fully fluctuating polymer field theory simulations," *Journal of Chemical Physics*, vol. 141, no. 17, 2014. 4.2.3

[55] J. C. Snyder, M. Rupp, K. Hansen, K. R. Müller, and K. Burke, "Finding density functionals with machine learning," *Physical Review Letters*, 2012. 5

[56] F. Brockherde, L. Vogt, L. Li, M. E. Tuckerman, K. Burke, and K. R. Müller, "Bypassing the Kohn-Sham equations with machine learning," *Nature Communications*, 2017. 5

[57] W. E. McMullen and K. F. Freed, "A density functional theory of polymer phase transitions and interfaces," *The Journal of Chemical Physics*, vol. 92, no. 1990, p. 1413, 1990. A.1

[58] M. Muramatsu, T. Nakano, T. Tomita, K. Yamamoto, K. Matsuzaki, and T. Kitano, "Simulation analysis of directed self-assembly for hole multiplication in guide pattern," *Proceedings of the SPIE - Alternative Lithographic Technologies VI*, vol. 9049, p. 904921, 2014. A.2